# THE SOURCE OF SOLAR OSCILLATIONS

A DISSERTATION
SUBMITTED TO THE DEPARTMENT OF APPLIED PHYSICS
AND THE COMMITTEE ON GRADUATE STUDIES
OF STANFORD UNIVERSITY
IN PARTIAL FULFILLMENT OF THE REQUIREMENTS
FOR THE DEGREE OF
DOCTOR OF PHILOSOPHY

Rakesh Nigam
May 2000

I certify that I have read this dissertation and that in my opinion it is fully adequate, in scope and quality, as a dissertation for the degree of Doctor of Philosophy.

Philip H. Scherrer
(Principal Adviser)

I certify that I have read this dissertation and that in my opinion it is fully adequate, in scope and quality, as a dissertation for the degree of Doctor of Philosophy.

Arthur B. C. Walker II

I certify that I have read this dissertation and that in my opinion it is fully adequate, in scope and quality, as a dissertation for the degree of Doctor of Philosophy.

Ronald N. Bracewell

Approved for the University Committee on Graduate Studies:

# Abstract

The Sun is permeated by acoustic oscillations. The findings in this dissertation address the characteristics of the source exciting these waves and is consistent with the following proposed excitation mechanism: blobs of hot gas continually rise in the outer layer of the convection zone where they are cooled and collapse. This volume change results in monopolar emission of sound. Cool, dense parcels of gas then accelerate downward into the intergranular lanes and lead to dipolar acoustic emission due to the monopole source. Finally, the void left behind by the downflow is filled by horizontal flow resulting in Reynolds stresses which produce quadrupolar emission. During this process of acoustic excitation by turbulent convection there is photospheric darkening seen in the intensity observations.

Power spectra of these oscillations obtained with the Michelson Doppler Imager instrument on-board the Solar and Heliospheric Observatory are asymmetric about their central peaks. At frequencies above the acoustic cutoff frequency, the asymmetry is reduced. Surprisingly, a reversal in asymmetry is seen, along with a high frequency shift between velocity and intensity; where the velocity power drops off rapidly compared to the intensity power. The observed phase difference between velocity and intensity jumps in the vicinity of an eigenfrequency and is not 90 degrees as predicted by adiabatic theory of oscillations below the acoustic cutoff frequency.

The granulation signal is partially correlated with the oscillations, observed as photospheric darkening, and is related to the strength of the acoustic source. A model to explain the observed power spectra and the phase difference shows that the correlated signal is higher in intensity than in velocity. A novel asymmetric formula is derived and used to fit the power spectra, thus allowing accurate determination of the eigenfrequencies, resulting in more precise information about the solar interior and rotation. Finally, different types of excitation sources at various depths are studied, and a best match with observations occur when monopole and quadrupole acoustic sources are placed in the superadiabatic layer at a depth of 75 km below the photosphere where the turbulence is most intense and consistent with the proposed excitation mechanism.

# Acknowledgements

My doctoral studies at Stanford have been a unique educational experience, which resulted in the interaction with many people. First and foremost I would like to thank my advisor, Phil Scherrer for providing the guidance in this thesis. He was always available for discussions and gave constructive suggestions and ideas. I am grateful to him for allowing me to participate in various conferences and giving me freedom during the course of this research. My other committee members, Ron Bracewell, Doug Osheroff, Art Walker and Antony Fraser-Smith played the role of informal advisors giving me time and assistance. I would also like to thank Sasha Kosovichev for being helpful in this research. He took personal interest and spent a lot of his time on this project, especially the countless discussions I had with him. He gave me lot of insight when I was stuck at times.

I must also thank the other members of the helioseismology group, Tom Duvall, Todd Hoeksema, Rick Bogart, Rock Bush, Taeil Bai, Xuepu Zhao, John Beck, Jesper Schou, Rasmus Larsen, Peter Giles, Laurent Gizon, Aimee Norton and Aaron Birch for providing a stimulating environment. Todd trained me to be an observer at the Wilcox Solar Observatory. Others in the community gave helpful advice on the problems tackled in the thesis. Thanks go to Bob Stein, Dali Georgobiani and Dennis Martinez. Brian Roberts was helpful with the computer problems I had. I am thankful to Sam Karlin for offering me a postdoc position in his group in a new field. Margie Stehle, Reneé Rittler and Paula Perron have been very helpful and took care of the administrative issues very efficiently.

Most of all, I must thank my family. My parents, for cultivating interest in reading and learning and my wife who is always there for me.

This research was supported by SOI-MDI NASA contract NAG5-3077 at Stanford University.

# Contents

# List of Figures

# Chapter 1

# Introduction

Solar oscillations have been used to study the structure and rotation of the Sun. They were first observed by Leighton (1960) to have a period of about five minutes. A theoretical explanation of their existence was given ten years later by Ulrich (1970) and, Leibacher and Stein (1971). They described them as standing waves trapped inside the Sun. About five years later Deubner (1975) observed that the power in these oscillations as a function of frequency and horizontal wavenumber lies along ridges. With the discovery of these oscillations the field of helioseismology was born and since then has blossomed into an exciting new field of astrophysics.

The 1995 launch of the Solar and Heliospheric Observatory (SOHO space mission) provided near continuous observations free from atmospheric turbulence that made possible the results in this thesis. With the advent of better data that was not available in the past, several exciting techniques emerged and the Sun is beginning to share its secrets.

Oscillations are trapped in the Sun. Studying them enables us to infer the structure and properties of the Sun. Broadly speaking, solar oscillations consist of two kinds of waves. The acoustic or p modes are waves in which pressure is the restoring force. The other kind are internal gravity waves, the g modes, in which gravity is the restoring force. The g modes have not been unambiguously detected so far. A special case that deserves mention is the fundamental mode, the f mode, which is a surface gravity wave having no radial nodes.

In this thesis, we study the observed properties of the oscillation spectra of p modes. These oscillations are observed as fluctuations in intensity and line-of-sight velocity. They produce motion of gas particles and cause Doppler shifts of absorption lines. The pressure fluctuations of these modes are related to the intensity fluctuations. Various parts of the absorption line are formed in different layers of the atmosphere. Hence, the height of the observations depends on the position in the absorption line at which measurements are made. In the Michelson Doppler Imager (MDI) instrument on board the Solar and Heliospheric Observatory (SOHO) the observations are made 300 km above the photosphere, in the Nickel I 6768 Å absorption line (Scherrer et al., 1995).

In the next chapter an explanation of the line asymmetry puzzle which was first observed by Duvall et al. (1993) is given. The power spectra of the oscillations is not symmetrical, but exhibits varying degrees of asymmetry. Numerous people have studied this phenomenon (Gabriel, 1992, 1993, 1995), (Abrams and Kumar, 1996), (Roxburgh and Vorontsov, 1995), (Rast and Bogdan, 1998), without finding a solution to the puzzle. Recently Roxburgh and Vorontsov (1997) proposed a solution. They suggested that there is velocity overshoot of the granulation which reverses the asymmetry in the velocity power spectrum. However, observations tend to support the fact that the reversal of asymmetry occurs in intensity rather than the velocity power spectrum. This work proposes that the reversal is explained by the presence of correlated noise due to the granulation which happens to be large in the intensity fluctuations (Nigam et al., 1998). This conclusion is explained in chapter 2 of the thesis. At frequencies above the acoustic cutoff frequency, waves propagate and are no longer trapped in the cavity. Due to the presence of correlated noise, a high frequency shift between the velocity and intensity power spectrum is predicted by the model. This is supported by MDI observations.

In chapter 3 the phase difference between velocity and intensity helioseismic spectra is discussed. This was first observed by Deubner and Fleck (1989) from ground based measurements and later by Straus et al. (1998) from the SOHO instrument. No satisfactory explanation has been provided for the phase jumps in the vicinity of an eigenfrequency. According to theory the phase is constant and should not jump.

This unusual behavior of the phase is explained by the same model that explains the reversal of asymmetry. It is the interaction of the oscillations with the background that results in this peculiar phase difference (Nigam and Kosovichev, 1999a).

Chapter 4 deals with the derivation of an asymmetrical fitting formula using a simple potential well model (Nigam and Kosovichev, 1998). It takes into account the correlated noise that is responsible for the reversal in asymmetry. This formula is used to determine the eigenfrequencies of the p modes, which can then be used to study the solar structure and rotation. In the past, eigenfrequencies were generally determined by fitting a symmetrical Lorentzian profile to the asymmetric power spectra. Clearly, this resulted in errors, as is demonstrated in the chapter. The formula is tested on low degree p modes and is found to perform quite well (Toutain et al., 1998).

All this leads to the natural question as to how p modes are excited. This is dealt with in chapter 5. The results in chapters 2 and 3 combine in a self consistent manner to answer this question. We apply Lighthill's formulation (Lighthill, 1952), (Stein, 1967), (Goldreich and Kumar, 1988), (Kumar, 1994) and decompose the source into monopole, dipole and quadrupole types. A very simple model of turbulence is assumed with regards to the mathematical framework. We find that a model based on a simple representation of turbulent convection is consistent with the observations suggesting that the source of oscillations may be turbulent convection. The oscillations appear to be excited in the superadiabatic layer 75 km below the photosphere by a combination of monopole and quadrupole sources (Nigam and Kosovichev, 1999b). The monopole source results from the mass or entropy fluctuations while the quadrupole results from the Reynolds stresses. The monopole source is the dominant one. The dipole source as a result of the Reynolds stress forces is ruled out by the observations.

Finally, chapter 6 concludes the thesis pointing to future directions of research, which follow as extensions of the work presented here.

The thesis uses numerical models to represent the Sun. Studies are made by comparing the computations from these models with the observed quantities. By doing this a better insight into the physical processes that work in the Sun can be gained. I briefly explain below the main observational and theoretical techniques used in this thesis.

## 1.1 Observations

The observables derived by the MDI instrument that are used here are the Doppler velocity, line depth and the continuum intensity. It will be worth describing briefly how this is accomplished. MDI records filtergrams which are images of the solar photosphere in selectable, well-defined narrow wavelength bands. The observables are computed by the instrument since there is insufficient telemetry to transmit the number of filtergrams required to compute these observables at a given cadence and resolution. Due to this fact, the actual observables are derived quantities based on multiple sets of filtergrams at five fixed wavelengths separated by 75 mÅ, denoted by $F_0$ through $F_4$. $F_0$ being nearly continuum, $F_1$ and $F_4$ centered on the wings and $F_2$ and $F_3$ centered about the core of the center-of-disk Ni I 6768 Å line (Scherrer et al., 1995). The filtergrams are combined onboard by an image processor to produce the velocity, intensity and line depth measurements which are shown in Figure 1.1, and are discussed below.

A flexible observing parameter is the resolution. Some studies have been done with integrated light spectrum over the entire disk (low resolution), and some other cases have been more successfully done with an imaged (high resolution) map of the Sun. The issue of resolution depends on the practical objective for a given set of observations.

### 1.1.1 Doppler velocity

Velocity measurements usually consist of sampling the intensity of the desired spectral absorption line at a slightly redshifted and an equally blueshifted wavelength. These values may then be converted to Doppler wavelength shift using some measure of the difference between intensities. In other words, the Doppler measurement relates to a differential measurement in a Fraunhofer line. Since the solar spectrum lines are rather narrow, typically even a small redshift will give a large intensity difference. This causes the Doppler measurements to be extremely sensitive. Doppler measurements are fairly stable, but the effects of solar rotation are significant and care must be taken to extract them. The velocity imposed by solar rotation is on the order of 2

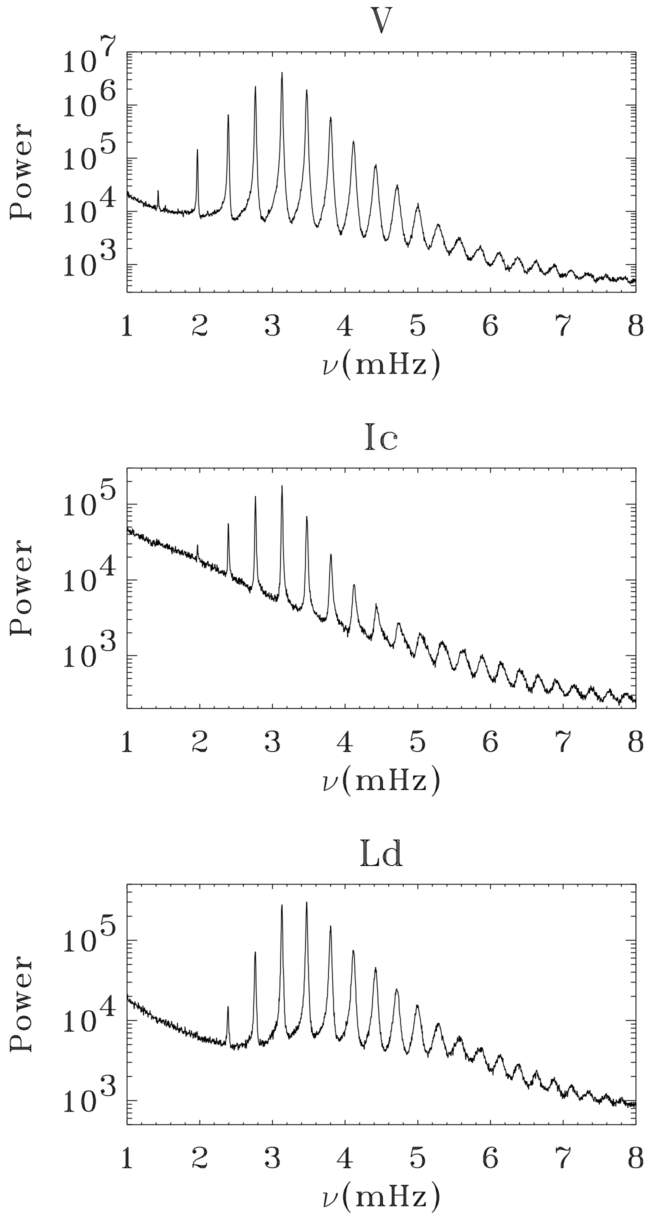

Figure 1.1: Typical power spectra for solar oscillations of angular degree $l = 200$ in Doppler velocity, in $(\mathrm{cm/sec})^2$ (top), continuum intensity, in $(\text{CCD counts per sec})^2$ (middle) for the same 3-day period of 21-23 July 1996 and line depth (bottom) for a 3-day duration of 17-19 July 1996 from the MDI full disk data. The leftmost peak of the velocity spectrum corresponds to the f mode. The other peaks in the spectra correspond to acoustic (p) modes.

km/sec, while the p mode oscillations have a typical velocity of about 50 cm/sec per mode.

MDI derives an estimate of the Doppler velocity from a ratio of differences of filtergrams $F_1$ through $F_4$:

$$\alpha_> = [(F_1 + F_2) - (F_3 + F_4)]/(F_1 - F_3) \tag{1.1}$$

$$\alpha_< = [(F_1 + F_2) - (F_3 + F_4)]/(F_4 - F_2) \tag{1.2}$$

where the first ratio, equation (1.1), is used with a positive numerator while the latter equation (1.2) is used to calculate the Doppler velocity when the numerator is less than or equal to zero. The Doppler shift is calculated from a tabulated nearly linear function of the filtergram difference ratios. This measurement has several noteworthy properties:

1) It is essentially blue wing minus red wing intensity divided by continuum minus line center intensity so it is quite insensitive to variations in the slopes of the wing intensities. The purpose of this measurement is to get a proxy measure that is nearly linear over a large dynamic range. The line core actually crosses $F_2/F_3$ near the limbs (Scherrer et al., 1995).

2) It is independent of linear gain and offset variations in the intensity measurements.

### 1.1.2 Line depth

The line depth proxy is the continuum minus line center intensity. It is estimated from the four filtergrams by:

$$I_{\text{depth}} = \left[2[(F_1 - F_3)^2 + (F_2 - F_4)^2]\right]^{1/2} \tag{1.3}$$

The formula has similarities to the Doppler calculation since it involves subtracting filtergrams. Any brightness offsets in the filtergrams due to granulation tend to cancel in the line depth and Doppler measurements. Therefore there are similarities between velocity and line depth power spectra (see Figure 1.1).

### 1.1.3 Continuum intensity

Intensity measurements have the advantage of being perhaps one of the easiest measurements to take. No fancy calibrations are required. Intensity measurements are also less likely to need correction for rotation of the Earth/Sun. However, the fluctuation in intensity due to small oscillations is only on the order of 1 ppm (part-per-million), so the measurement is very sensitive to any kind of signal degradation. That is why these measurements are so sensitive to granulation, atmospheric turbulence and cloud interference from the Earth's surface. Many of these problems are alleviated with spaceborne observations.

The MDI proxy for the continuum intensity near the Ni-I absorption line of the measurements is computed with all five filtergrams according to the equation:

$$I_{\mathrm{cont}} = 2F_0 + I_{\mathrm{ave}} + I_{\mathrm{depth}}/2 \tag{1.4}$$

where $I_{\mathrm{ave}}$ is the average of the four filtergrams, $F_1$ through $F_4$. This formula is different from the previous two measurements in that there is the $(2F_0 + I_{\mathrm{ave}})$ term which contains the sum of the filtergrams. Any brightness offset due to granulation in the filtergrams doesn't cancel in the intensity measurement.

### 1.1.4 Integrated light techniques

Integrated light techniques used by MDI, which sums CCD pixels have been deployed previously by the IRIS (International Research on the Interior of the Sun, administered by the Université de Nice, France) instrument (Fossat, 1991). Instruments in this category use integrated sunlight and so they measure the average surface velocity over the solar disk. They view the Sun as a star and study p modes of very low degree ($l$ = 0,1,2). These techniques are unable to study higher degree modes because higher $l$ modes have nearly equal areas of the disk which are receding and approaching effectively canceling out any velocity signal when averaged over the entire disk. Since there is no spatial resolution with this technique, there is no way of isolating out which mode is being measured.

### 1.1.5 Imaging techniques

The imaging techniques take advantage of modern CCD detectors to record velocity (or intensity) measurements on a discrete grid over the visible disk. These techniques have been used by the MDI instrument (Scherrer et al., 1995), where the CCD is a $1024^2$ grid. This method returns a slew more data and allows resolution of individual modes and analysis of their surface patterns. Usually for imaged methods, a Doppler measurement is used for its superior signal/noise ratio.

## 1.2 Data processing

The various steps involved are recording the oscillation (using either intensity or Doppler velocity measurements), calibrating and correcting the data, splitting the recorded oscillations into their component spherical harmonics and then analyzing the resonant frequencies of each individual harmonic.

Step 1: Record the data using either velocity or intensity, which are computed from the filtergrams.

Step 2: Calibrate all the data. Correct the data for known effects like instrument drifting, solar rotation, etc. Remove from the velocity a model of the spacecraft motion and solar rotation.

Step 3: Isolate the contribution from each spherical harmonic. This involves multiplying the data set at a particular time by one of the spherical harmonics functions ($Y_l^m$, where $l$ is the angular degree and $m$ is the azimuthal order) and integrating over the disk (Christensen-Dalsgaard, 1994). The resultant is the contribution from that spherical harmonic degree to the velocity/intensity distribution over the disk. Since one observes less than half of the Sun, the spherical harmonic functions are no longer orthogonal, and the modes we isolate are not exactly what we intend to, but a slight mixture of neighboring modes as well. As a result of this, leakage has to be taken into account. The result from this step is a series of coefficients: one for each harmonic considered at each time step. The time series are then detrended and gap filled.

Step 4: Convert the time series to frequency (power) spectrum. This is a Fourier transform (Bracewell, 1986) of each mode in time. The result is a spectrum showing the frequency content of each mode.

In general, a power spectrum is plotted only for each degree, $l$. This is because the modes with different $m$ but same $l$ are almost identical. The $m$ modes cause small peak splittings, which is used in the analysis of internal rotation rates. There is also a radial order, $n$, which we have not taken into account yet, since it is not visible from the surface. Each peak in the power spectrum corresponds to a different radial order $n$ for the same degree, $l$.

The best possible frequency resolution is inversely proportional to observing time and lifetime, therefore observations should be made for as long as time permits. This is important for two reasons: firstly, since g modes have long periods and low amplitudes, and in order to get a strong spectrum, long observation times are required. A second reason is that Fourier analysis assumes an infinite time series, and discrete ends to that produce undesirable effects. Data must be recorded often in order to get a good sampling of the oscillations. This reduces aliasing problems. From the above discussion it is clear that observations must be recorded for as long and continuous a period as is possible. Several strategies have been used to achieve the above task. Observations from the South pole have been carried out in the past, where the Sun is visible for longer periods of time. Another solution is a network of observing sites around the globe spaced so that their observing times overlap each other to produce one continuous data set. A third method that is being tried is to observe from space, unobstructed by atmospheric effects.

## 1.3 Mode physics

The Sun's surface is found to be in a state of continuous motion when measured by the different instruments. There are flares and other bizarre phenomena happening on the surface. However, measurements of either the velocity or intensity across the solar disk shows that it is oscillating in a periodic way.

These oscillations, although very complex, are actually combinations of millions of resonant modes of vibration. Each mode is vibrating at a specific frequency caused by waves of that frequency resonating in different cavities in the Sun. These cavities are not gaps and walls in the Sun, like those found in buildings. But rather they are defined by a combination of both the solar interior properties and the wave frequency. Only inside a particular cavity are the conditions right for a certain wave to propagate stably; outside the boundaries, it either is reflected back or decays exponentially.

Solar p modes are sound waves trapped in the cavity. As sound waves propagate into the Sun their sound speed increases due to an increase of temperature. This causes them to refract continually until they are reflected back to the surface of the Sun (Christensen-Dalsgaard, 1994). At the surface the solar properties change abruptly, and waves whose wavelength is smaller than the density scale height propagate, while others get reflected and are trapped in the cavity.

Because the amplitude of the oscillations observed are small compared to their wavelength, their properties can be studied by means of a linear theory. Therefore, the oscillations can be decomposed into a linear combination of many resonant modes. The frequencies of these modes are in turn related to the structure of the interior of the Sun, and may be calculated using physics of stellar interiors (Christensen-Dalsgaard, 1994).

The mathematical framework used to study these oscillations are the usual equations of hydrodynamics. Even though we know that this is not true, to simplify matters we assume a non-rotating, non-magnetic and spherically symmetric Sun.

The equation of continuity which expresses the conservation of mass becomes

$$\frac{\partial \rho}{\partial t} + \nabla \cdot (\rho \boldsymbol{v}) = 0 \tag{1.5}$$

where $\rho$ is the density, $t$ the time and $\boldsymbol{v}$ the velocity.

The equation of motion (Newton's second law) is

$$\rho\left(\frac{\partial \boldsymbol{v}}{\partial t}+\boldsymbol{v}\cdot\nabla\boldsymbol{v}\right)=-\nabla p+\rho\boldsymbol{f_b} \tag{1.6}$$

where $p$ is the pressure, $\boldsymbol{f_b}$ the body forces. Among the possible body forces we consider only gravity $\boldsymbol{g}$.

If the motion occurs adiabatically then $p$ and $\rho$ are related by

$$\frac{Dp}{Dt}=c^2\left(\frac{D\rho}{Dt}\right) \tag{1.7}$$

where $c^2=\gamma_1 p/\rho$ is the sound speed, $\gamma_1$ is the adiabatic exponent and $D/Dt$ is the material derivative, following the motion of the fluid element; given by

$$\frac{D}{Dt}=\frac{\partial}{\partial t}+\boldsymbol{v}\cdot\nabla \tag{1.8}$$

This is contrasted with the local derivative $\partial/\partial t$ at a fixed point. The first three equations (1.5)-(1.7) form the complete set of equations for adiabatic motion.

The observed solar oscillations have very small amplitudes (maximum velocity of a superposition of millions of p modes at the surface is about 500 m/sec) compared with the characteristic scales of the Sun, therefore they can be treated as small perturbations around an equilibrium state. We also assume that the equilibrium structure is static compared to the oscillation time scale (p modes have a period of about 5 minutes) and that there are no velocities.

Thus by representing each field variable $f(\boldsymbol{r},t)=f_0(\boldsymbol{r})+f'(\boldsymbol{r},t)$, where $f_0(\boldsymbol{r})$ is the equilibrium state and $f'(\boldsymbol{r},t)$ is a small Eulerian perturbation, that is the perturbation at a given point $\boldsymbol{r}$, we linearize the above equations about the equilibrium state by expanding them in the perturbations and retaining only terms that do not contain products of the perturbations.

The equations (1.5)-(1.6) of continuity and motion become

$$\frac{\partial \rho'}{\partial t}+\nabla\cdot(\rho_0\boldsymbol{v}')=M(\boldsymbol{r},t) \tag{1.9}$$

$$\rho_0 \frac{\partial \boldsymbol{v}'}{\partial t} + \nabla p' + \rho' \boldsymbol{g}_0 = \boldsymbol{F}(\boldsymbol{r}, t) \tag{1.10}$$

The right hand sides of the equations are the source terms which drive the oscillations. In deriving the above equations the Cowling approximation was applied, with the neglect in the perturbation of the acceleration due to gravity (Christensen-Dalsgaard, 1994). Here $M$ and $\boldsymbol{F}$ are the mass and force sources and are given by:

$$M = -\nabla \cdot (\rho' \boldsymbol{v}') \tag{1.11}$$

$$\boldsymbol{F} = -\rho' \frac{\partial \boldsymbol{v}'}{\partial t} - \nabla \cdot (\rho_0 \boldsymbol{v}' \boldsymbol{v}') \tag{1.12}$$

It is convenient to transform the above equations expressing the Eulerian perturbations in terms of the Lagrangian perturbations, which are perturbations following the motion of the fluid. They are related as

$$\delta f(\boldsymbol{r}) = f'(\boldsymbol{r}_0) + \delta \boldsymbol{r} \cdot \nabla p_0 \tag{1.13}$$

where $\delta f$ is the Lagrangian perturbation of the field variable $f$ and $\delta \boldsymbol{r}$ is the fluid displacement. The velocity $\boldsymbol{v}$ is given by the time derivative of the displacement $\delta \boldsymbol{r}$

The equation for adiabatic motion becomes

$$\delta p = c_0^2 \delta \rho \tag{1.14}$$

where $c_0$ is the equilibrium sound speed, which is computed from a solar model.

The fluid displacement can be written in terms of the spherical harmonics $Y_l^m(\theta, \phi)$

$$\delta \boldsymbol{r} = 2\sqrt{\pi} Re \left[ \left( \psi_r(r), \psi_h(r) \frac{\partial}{\partial \theta}, \frac{\psi_h(r)}{\sin\theta} \frac{\partial}{\partial \phi} \right) Y_l^m(\theta, \phi) \exp(i\omega_{nl} t) \right] \tag{1.15}$$

where $r$ is the distance from the center, $\theta$ is the colatitude (angle from the polar axis), $\phi$ is the longitude and $\psi_r$ and $\psi_h$ are the radial and horizontal components of the displacement. The angular frequency $\omega_{nl}$ is complex and contains the effect of the damping. In this thesis viscous damping is considered.

Carrying out the spherical harmonic decomposition of the equations of mass and momentum leads to the following ordinary differential equations, with the subscripts $nl$ dropped in the angular frequency $\omega$ and the subscript 0 dropped from the equilibrium variables:

$$\frac{d\psi_r}{dr} + \psi_r\left(\frac{2}{r} + \frac{d\ln\rho}{dr}\right) + \frac{\rho'}{\rho} - \frac{l(l+1)}{\rho r^2\omega^2}p' = S_1 \tag{1.16}$$

$$\frac{dp'}{dr} + g\rho' - \omega^2\rho\psi_r = S_2 \tag{1.17}$$

The sources $S_1$ and $S_2$ are

$$S_1 = \frac{1}{\rho\omega^2}\int dt\ \exp(-i\omega t)\int\frac{d\Omega}{\rho}F_{\mathrm{h}} \tag{1.18}$$

$$S_2 = -\int dt\ \exp(-i\omega t)\int d\Omega\, F_{\mathrm{v}} \tag{1.19}$$

where $\Omega$ is the solid angle, $F_{\mathrm{h}}$ and $F_{\mathrm{v}}$ contain the horizontal and radial component of the forces and are given by:

$$F_{\mathrm{h}} = \left[\frac{1}{r}\frac{\partial Y_l^{m^*}}{\partial\theta}F_\theta + \frac{1}{r\sin\theta}\left(\frac{\partial Y_l^{m^*}}{\partial\phi}\right)F_\phi - \frac{\partial^2 M}{\partial t^2}\right] \tag{1.20}$$

$$F_{\mathrm{v}} = Y_l^{m^*}F_r \tag{1.21}$$

where $\boldsymbol{F} = (F_r, F_\theta, F_\phi)$ and $^*$ is the complex conjugate.

The above equations (1.16) and (1.17) can be rewritten involving Lagrangian perturbations (Gough, 1993) and become:

$$\frac{d\xi}{dr} + \left(\frac{2}{r} - \frac{L^2 g}{\omega^2 r^2}\right)\xi + \left(1 - \frac{L^2c^2}{\omega^2r^2}\right)\frac{\delta p}{\rho c^2} = S_1 \tag{1.22}$$

$$\frac{d\delta p}{dr} + \frac{L^2 g}{\omega^2 r^2}\delta p - \frac{g\rho f}{r}\xi = S_2 \tag{1.23}$$

where $L^2 = l(l+1)$, $\xi = \psi_r$ and the discriminant $f$ is

$$f = 2 + \frac{\omega^2 r}{g} + \frac{r}{H_g} - \frac{L^2 g}{\omega^2 r} \tag{1.24}$$

where $H_g^{-1}$ is the scale height of the gravitational acceleration and is

$$H_g^{-1} = -\frac{d \ln g}{dr} \tag{1.25}$$

By differentiating equation (1.23) with respect to $r$ and using equation (1.22) to eliminate $\frac{d\xi}{dr}$ and then using equation (1.23) to eliminate $\xi$, an equation for $\delta p$ is obtained:

$$\frac{d^2 \delta p}{dr^2} + H_u^{-1} \frac{d\delta p}{dr} + \left[ \frac{1}{c^2} \left( \omega^2 + \frac{g}{h} \right) - \frac{L^2}{r^2} \left( 1 - \frac{N_{\mathrm{s}}^2}{\omega^2} \right) \right] \delta p = S_{12} \tag{1.26}$$

where $H_u^{-1}$ and $N_{\mathrm{s}}$ are

$$H_u^{-1} = H^{-1} + H_f^{-1} + H_g^{-1} + 3r^{-1} \tag{1.27}$$

$$N_{\mathrm{s}}^2 = g \left( H_u^{-1} - \frac{g}{c^2} - 2h^{-1} \right) \tag{1.28}$$

and $h^{-1} = H_g^{-1} + 2r^{-1}$ is the scale height of $\frac{g}{r^2}$ and $H_f^{-1}$ is the scale height of $f$.

It is convenient to reduce equation (1.26) into more compact form by means of the transformation (Gough, 1993)

$$\delta p = \left( \frac{g \rho f}{r^3} \right)^{1/2} \Psi := u \Psi \tag{1.29}$$

$$\frac{d^2 \Psi}{dr^2} + K^2 \Psi = S \tag{1.30}$$

where $S = S_{12}/u$, is given by

$$S(r, \omega) = \left[ c_1 \frac{dS_2}{dr} + c_2 S_2 \right] + \left[ c_3 \frac{dS_1}{dr} + c_4 S_1 \right], \tag{1.31}$$

where $c_1, c_2, c_3$ and $c_4$ depend on the solar model and are given in Appendix A.1 and $K$ is

$$K^2 = \frac{\omega^2 - \omega_{\rm cs}^2}{c^2} + \frac{l(l+1)}{r^2}\left(\frac{N_{\rm s}^2}{\omega^2} - 1\right) \tag{1.32}$$

where $\omega_{\rm cs}$ is

$$\omega_{\rm cs}^2 = \frac{c^2}{4H_u^2}\left(1 - 2\frac{dH_u}{dr}\right) - \frac{g}{h} \tag{1.33}$$

Here $H_u^{-1}$ is the scale height of the factor $u$ defined in equation (1.29). Medium $l$ oscillations are confined to the outer convective layers of the Sun, hence the effect of spherical geometry can be neglected. In the plane-parallel approximation $\omega_{\rm cs}$ reduces to $\omega_{\rm c}$ the acoustic cutoff frequency and $N_{\rm s}$ reduces to $N$ the buoyancy frequency, which are given below:

$$\omega_c^2 = \frac{c^2}{4H^2}\left(1 - 2\frac{dH}{dr}\right) \tag{1.34}$$

$$N^2 = g\left(\frac{1}{H} - \frac{g}{c^2}\right) \tag{1.35}$$

where $H^{-1}$ is the density scale height:

$$H^{-1} = -\frac{d\ln\rho}{dr} \tag{1.36}$$

The solutions to this reduced wave equation (1.30) are evanescent if $K^2 < 0$, and waves propagate when $K^2 > 0$. The two frequencies define the cavities in the Sun. It follows from the constraint $K^2 > 0$ that there are two different types of cavities, where the p and g modes propagate. This can be easily seen if we rewrite $K$ as:

$$K^2 = \frac{\omega^2}{c^2}\left(1 - \frac{\omega_+^2}{\omega^2}\right)\left(1 - \frac{\omega_-^2}{\omega^2}\right) \tag{1.37}$$

This makes it clear that there are two separate propagation zones: where the wave frequency $\omega > \omega_+$, and where $\omega < \omega_-$. These boundary frequencies $\omega_+$ and $\omega_-$ are given by

$$\omega_+^2 = \frac{1}{2}(S_l^2 + \omega_{\rm cs}^2) + \left[\frac{1}{4}(S_l^2 + \omega_{\rm cs}^2)^2 - N_{\rm s}^2 S_l^2\right]^{1/2} \tag{1.38}$$

$$\omega_-^2 = \frac{1}{2}(S_l^2 + \omega_{\mathrm{cs}}^2) - \left[\frac{1}{4}(S_l^2 + \omega_{\mathrm{cs}}^2)^2 - N_{\mathrm{s}}^2 S_l^2\right]^{1/2} \tag{1.39}$$

where $S_l$ is the Lamb frequency and is

$$S_l^2 = \frac{c^2 L^2}{r^2} \tag{1.40}$$

In the interior of the Sun, the equations (1.38) and (1.39) can be approximated by:

$$\omega_+^2 \approx \frac{c^2 l(l+1)}{r^2} \tag{1.41}$$

$$\omega_-^2 \approx N^2 \tag{1.42}$$

Waves that propagate in the region defined by $\omega > \omega_+$ are called p modes, and those that resonate in the $\omega < \omega_-$ region are called g modes. Waves with frequency in the range $\omega_- < \omega < \omega_+$ are evanescent. A plot of the solar potential $\nu_+$ and $\nu_-$ is shown in Figure 1.2

### 1.3.1 P modes

P modes are standing pressure waves trapped in the Sun. They propagate stably in the region of the Sun defined by $\omega > \omega_+$.

For p modes,

$$K^2 \approx \frac{\omega^2 - \omega_+^2}{c^2} \tag{1.43}$$

The upper limit of this region is essentially when the wave frequency equals the acoustic cutoff frequency, and depends only on the speed of sound $c$ and the density scale height $H$. For p modes the discriminant $f > 0$ in equation (1.24) (Gough, 1993).

Once a wave reaches the point where its frequency equals this cutoff frequency, it is sharply reflected back inward. This cutoff point is fairly constant, between about 0.98 and 0.99 solar radii. However, it does have a finite upper limit in the outer layers

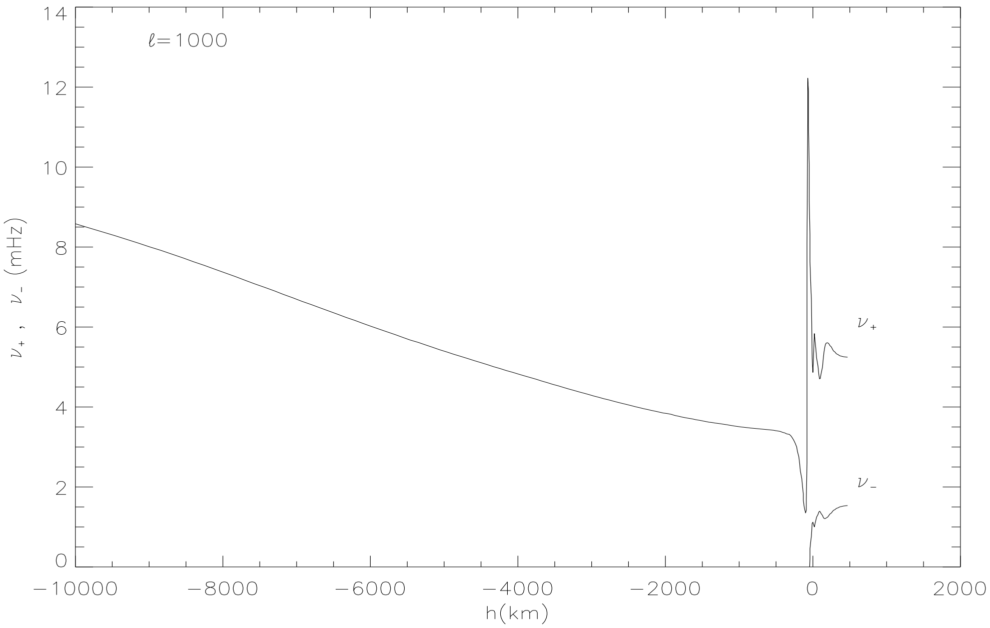

Figure 1.2: Solar potentials $\nu_+ = \omega_+/2\pi$ and $\nu_- = \omega_-/2\pi$ as a function of depth $h$ for for angular degree $l = 1000$. Depth 0 indicates the photosphere and negative depths are below the photosphere.

of the Sun. If a wave has a frequency greater than $\omega_\mathrm{c}$ then it will not be reflected back into the Sun. This constrains the p modes to have resonant frequencies lower than a specific value, set by the stellar structure.

The inner boundary of the p mode propagation cavity is caused by an increase in sound speed, $c$, towards the center of the Sun due to increase in temperature. As $c$ increases, the inner edge of the wave (closer to the core of the Sun) moves faster than the outer edge, causing the wave to gradually refract towards the surface. As the wave propagates deeper into the Sun, the wave is continually refracted until it is completely reflected. This inner turning point is described by the Lamb frequency $S_l$.

High frequency p modes include waves with $\omega > \omega_\mathrm{c}$, $\nu_\mathrm{c} = \omega_\mathrm{c}/2\pi = 5.2$ mHz. These waves propagate and are not trapped by the photosphere. It was therefore a surprise to find p mode ridges continue above the acoustic cutoff. The explanation by Kumar and Lu (1991) states that waves are emitted isotropically from a source near the top of the convection zone. Waves that propagate directly from the source interfere with the waves that are reflected from below due to the continual increase in sound speed. This interference is responsible for the observed high frequency ridges and this is true for the ridges above $l = 200$ as well. These high frequency waves suffer some amount of reflection in the solar atmosphere.

Note that this inner turning point does depend on the mode degree. For higher degree modes, the turning point will be nearer to the surface than for low degree modes. This is important, because it tells us how far a mode of particular degree penetrates into the interior of the Sun. Low order, low degree waves penetrate the deepest of all the modes. High degree ($l > 60$) don't penetrate any deeper than the convective layer, whereas low degree modes travel deeper down up to about 0.05 solar radii. Radial modes ($l = 0$) propagate right through the core (Christensen-Dalsgaard, 1994). The lower and upper turning points are shown in the plot of the solar acoustic potential $\nu_+ = \omega_+/2\pi$ in Figure 1.2.

### 1.3.2 G modes

G modes are rather mysterious. They hide deep within the solar interior and have not yet been observed. The main restoring force for these modes is buoyancy. The waves are essentially oscillations of packets of gas moving around their hydrostatic equilibrium position. If some initial disturbance perturbs the gas from equilibrium, it may rise above the equilibrium position only to find that its density is then greater than the new surroundings. The gas then sinks back down, but overshoots the equilibrium position, until it is in a region where its density is less than the surrounding gas. The packet is then forced up, and so on... The frequency of these waves is the buoyancy frequency.

G modes, like the p modes, are trapped within a cavity in the solar interior. These waves oscillate in a region defined by $\omega < \omega_-$. The upper limit of this region is the bottom of the convective layer, since in the convection zone the gravity waves are no longer stable.

The inner limit of the g mode cavity is defined by the buoyancy frequency $N$. The lower turning point occurs when $\omega = \omega_-$, or in other words when the wave frequency equals the buoyancy frequency. In the stable g mode region, $\omega_-$ is less than $N$. But as the wave travels towards the center, the gravitational acceleration reduces to the point till $N = \omega_-$. This is the turning point. Therefore g modes are nothing but standing internal gravity waves. For g modes $f < 0$ (Gough, 1993).

Gravity modes can be trapped either beneath the convection zone or in the atmosphere (Christensen-Dalsgaard, 1994). A single mode can exist in both regions; however, the evanescent decay is so great through the turbulent convection that extremely weak coupling between the atmosphere and the interior is likely to be destroyed by turbulence. Thus for practical purposes the interior modes and the atmospheric modes can be regarded as distinct.

G modes have much longer periods than the p modes (Christensen-Dalsgaard, 1994). Typical g mode periods are of the order of 165 minutes. Many observations have been done to detect these modes, but because of their very long periods and low amplitudes (as they are localized around the core of the Sun), the data and interpretations are full of ambiguities.

### 1.3.3 F mode

The p and g modes are separated by a mode with no radial node, whose frequency lies between those of the p and g modes. This mode can exist only when $l \neq 0$. Cowling called it the f mode, for fundamental gravity mode (Christensen-Dalsgaard, 1994).

The f mode is a special type of the g mode. It is the surface gravity wave that exists at the interface of fluids of differing density. The f mode propagates without compression, so it produces no pressure fluctuations. It has been observed in both the velocity and intensity observations, but not in line depth. The reason why it is present in intensity is not well understood. Since the f mode is a surface gravity wave, it has proved useful to study the surface magnetic fields, the constraining of the solar radius and other interesting surface effects. Moreover the frequencies of the f mode depend only on their wavelength and on gravity, but not on the internal structure of the layer, in particular the density. Its dispersion relation is given by $\omega^2 = gk$, where

$g$ is the acceleration due to gravity computed from the solar model and $k = L/R_{\mathrm{Sun}}$ is the wave number and $R_{\mathrm{Sun}}$ is the solar radius. The f mode satisfies the discriminant $f = 0$ (Gough, 1993). The displacement eigenfunction decays exponentially with depth from the solar surface, which is an indication that the mode is concentrated in the uppermost layers of the Sun, particularly when $k$ is large. Since the f mode propagates horizontally, it can be used to study supergranules and horizontal flow fields.

So, the Sun is observed to resonate at certain harmonic frequencies. Which frequencies are resonant is a combination of the frequency of the wave and the size of the cavity it is trapped in. Waves of millions of frequencies are excited in the interior of the Sun, but the specific structure of the Sun selects which exact frequencies are resonant. These frequencies are a measure of the interior structure of the Sun. Studying the p, g and f modes together would be useful in solving the mysteries of the Sun.

Before proceeding to discuss the excitation and damping of p modes, it will be worthwhile to review Lighthill's theory of sound generation.

## 1.4 Lighthill's theory

Sir James Lighthill in 1952 propounded his theory of sound generation due to fluid flow, with rigid boundaries. According to his theory sound is generated by a conversion of kinetic enery into acoustic, as a result of fluctuations in the flow of momentum across fixed surfaces.

The propagation of sound in a uniform medium, without sources of matter or external forces is governed by the equation of continuity and linearized equation of momentum

$$\frac{\partial \rho}{\partial t} + \frac{\partial}{\partial x_i}(\rho v_i) = 0, \tag{1.44}$$

$$\frac{\partial}{\partial t}(\rho v_i) + c_0^2 \frac{\partial \rho}{\partial x_i} = 0 \tag{1.45}$$

Eliminating the momentum density $\rho v_i$ from equations (1.44) and (1.45) leads to

$$\frac{\partial^2 \rho}{\partial t^2} - c_0^2 \nabla^2 \rho = 0 \tag{1.46}$$

Here $\rho$ is the density, $v_i$ is the velocity in the $x_i$ direction and $c_0$ is the sound speed in the uniform medium.

On the other hand, the original equation of momentum in an arbitrary continuous medium under no external forces in Reynolds's form is

$$\frac{\partial}{\partial t}(\rho v_i) + \frac{\partial}{\partial x_j}(\rho v_i v_j + p_{ij}) = 0 \tag{1.47}$$

Here $p_{ij}$ is the compressive stress tensor, representing the force in the $x_i$ direction acting on a portion of fluid, per unit surface area with inward normal in the $x_j$ direction. The other term $\rho v_i v_j$ is the momentum flux tensor, that is the rate at which momentum in the $x_i$ direction crosses unit surface area in the $x_j$ direction. This equation can be obtained from the momentum equation in the familiar Eulerian form by adding a multiple of the equation of continuity, equation (1.44). Physically, this equation represents the fact that the momentum contained within a fixed region of space as changing at a rate equal to the combined effect of (i) the stresses acting at the boundary $p_{ij}$ and (ii) the flow across the boundary of momentum-bearing fluid due to $\rho v_i v_j$.

Hence the equations of an arbitrary fluid motion can be rewritten as the equations of propagation of sound in a uniform medium at rest due to externally applied fluctuating stresses, namely, as

$$\frac{\partial}{\partial t}(\rho v_i) + c_0^2 \frac{\partial \rho}{\partial x_i} = -\frac{\partial T_{ij}}{\partial x_j} \tag{1.48}$$

$$\frac{\partial^2 \rho}{\partial t^2} - c_0^2 \nabla^2 \rho = \frac{\partial^2 T_{ij}}{\partial x_i \partial x_j} \tag{1.49}$$

where the instantaneous applied stress at any point is

$$T_{ij} = \rho v_i v_j + p_{ij} - c_0^2 \rho \delta_{ij} \tag{1.50}$$

Equations (1.48) and (1.49) are the basic equations of the theory of aerodynamic sound generation (Lighthill, 1952).

It has been pointed out in Lighthill's paper that all effects such as the convection of sound by the turbulent flow, or the variations in the sound speed within it, are taken into account, by incorporation as equivalent applied stresses, in equations (1.48) and (1.49). Thus outside the airflow the density satisfies the ordinary equations of sound, with out the stress $T_{ij}$ in equations (1.45) and (1.46), and the fluctuations in density, caused by the effective applied stresses within the airflow, are propagated acoustically. These stresses are responsible for the quadrupolar emission of sound.

The theory of sound generated aerodynamically was extended by Lighthill (1953), to take into account the statistical properties of turbulent airflows, from which the sound radiated (without the help of solid boundaries) is called aerodynamic noise. The quadrupole distribution is shown to behave as if it were concentrated into independent quadrupoles, one in each average eddy volume.

## 1.5 Excitation and damping of p modes

P modes have a period of about 5 minutes and are believed to be excited as a result of granulation in the outer turbulent convective zone (Goldreich and Keeley, 1977). The granulation turnover time is roughly 5 minutes, which suggests that p modes are excited as a result of granulation. The maximum amplitude of a superposition of velocity oscillations is small compared to the other characteristic scales of the Sun, and is about 500 m/sec. The convective currents randomly excite different frequencies within the Sun. Any given resonant oscillation gets damped and dies out after a lifetime of anywhere from hours to years, then is reexcited at some later time by the same random motion of the convective currents.

The linearized hydrodynamic equations derived in the previous sections adequately describe the excitation of p modes. The right hand side of the continuity equation (1.9) contains the mass term (monopole source), the momentum equation (1.10) has a force term (dipole source) on the right hand side. The force term contains the turbulent Reynolds stress, which is responsible for the quadrupole source. These sources could be produced by fluctuations in entropy. The physical significance of each of these sources along with their role in p mode excitation is discussed in the following subsections.

### 1.5.1 Monopole source

The monopole source results by forcing the mass in a fixed region of space to fluctuate (Crighton, 1975). By this kinetic energy is coverted into acoustic energy. A way of achieving this in linear acoustics is to suppose that sources of mass are distributed throughout the fluid, injecting fluid mass at a given rate. The right hand side of the linearized continuity equation describes the mass source. A time dependent mass flux, e.g., popping a balloon, cracking a finger, radially pulsating sphere etc. results in a monopole source. Entropy fluctuations due to radiative cooling at the solar surface are responsible for the monopole source in the Sun.

### 1.5.2 Dipole source

The dipole source results by forcing the momentum in a fixed region of space to fluctuate. This type of source is exactly equivalent to an external force distribution acting on the fluid (Crighton, 1975). The right hand side of the linearized momentum equation contains the force, which acts as the dipole source. The monopole and dipole terms are related in the Sun, since an increase in entropy will cause both an increase in the volume of the gas (the monopole part) and, because of the gravitational field, a change in the momentum of the gas (the dipole part). A time-varying force (momentum flux) is responsible for dipole emission such as sound from a musical string or a tuning fork or the force due the Reynolds stresses in the Sun.

### 1.5.3 Quadrupole source

The quadrupole source results by forcing the rates of momentum flux across fixed surfaces to vary, as when sound is generated aerodynamically with no motion of solid boundaries. In a theoretical treatment, the real fluid, in which highly-nonlinear motions may occur, is replaced by a fictitious acoustic medium, in which only small amplitude linear motions occur. If this medium is acted upon by an external stress system, then exactly the same density fluctuations will be produced. This is the basis of Lighthill's theory. The quadrupole stress distribution is derived from dipoles in exactly the same way as the dipole from a monopole by a limiting process. A quadrupole is formed by taking the limit of two adjacent equal and opposite dipoles. Thus, there are two characteristic directions associated with a quadrupole: one the direction of the individual dipoles, the other the direction in which the dipoles are separated. Since there are three components of each direction, there are nine possible independent orientations of the quadrupole axes. These divide into a group of three longitudinal quadrupoles in which the dipoles or monopoles are arranged in a line and in which both characteristic directions coincide, and a group of six lateral quadrupoles with mutually perpendicular characteristic directions (Crighton, 1975). Now, two equal and opposite adjacent forces constitute a stress; a pressure type stress in the longitudinal case, a shear stress in the lateral case. Internal stresses with no associated mass or momentum flux as in the case of free turbulence is responsible for quadrupolar emission of acoustic waves. In the Sun Reynolds stresses act as quadrupole sources.

For Lighthill's theory to be valid, the physical conditions should be such that wave motions, satisfying the homogeneous wave equation, do emerge at sufficiently great distances from the unsteady flow. Therefore, Lighthill's theory reduces to the ordinary acoustic theory at all points outside the region of unsteady flow.

## 1.6 Why is this problem important?

By studying the excitation of p modes one learns the underlying physics of excitation and about the source of these modes. This is then useful in deriving a fitting formula to accurately determine the p mode eigenfrequencies by fitting the observed velocity and intensity power spectra. An accurate determination of the frequencies will in turn have an effect on the inversions to determine the solar structure and rotation rate.

# Chapter 2

# The Line Asymmetry Puzzle

`(Part of this chapter is published in ApJ 1998, 495, L115)`

Line asymmetry is closely linked to the excitation of p modes. Observations of Duvall et al. (1993) have indicated that the power spectrum of solar acoustic (p) modes show varying amounts of asymmetry. In particular, the velocity and intensity power spectra revealed an opposite sense of asymmetry. There was scepticism about the result (Abrams and Kumar, 1996), and it was even believed to be an error in the experiment. However, the new MDI data presented here confirm the result and, in addition, allow us to study the variations of asymmetry among modes of various angular degrees and frequencies.

The variations in the asymmetry have important implications in helioseismology where the eigenfrequencies are generally determined by assuming that the line profile is symmetric and can be fitted by a Lorentzian. This leads to systematic errors in the determination of frequencies and, thus, affects the results of inversions.

Several authors have studied this problem theoretically and have found that there is an inherent asymmetry when the solar oscillations are excited by a localized source (Gabriel, 1992); (Duvall et al., 1993); (Roxburgh and Vorontsov, 1995); (Abrams and Kumar, 1996); (Nigam et al., 1997). Physically, the asymmetry is an effect of interference between an outward direct wave from the source and a corresponding inward wave that passes through the region of wave propagation (Duvall et al., 1993).

However, the precise cause for the asymmetry and its relation to the Sun's acoustic source have not been pinned down in the past. We briefly describe the observations, formulate a theoretical model and from it suggest an explanation for the difference in asymmetries between velocity and intensity and finally estimate the depth and type of the sources that are responsible for exciting the solar p modes.

## 2.1 Observations

To compare the asymmetry in velocity and intensity spectra we computed spherical harmonic transforms (SHTs) of full disk velocity and intensity images from the MDI instrument (Scherrer et al., 1995). These SHT's were gap filled, Fourier transformed to make power spectra, shifted in frequency according to a solar rotation law, and averaged over the angular order $m$. To simplify the comparison we chose the days July 21 to July 23, 1996 for which simultaneous velocity and intensity images were available. The results for oscillations of angular degree $l = 200$ are shown in Figure 2.1.

From these two power spectra that have been normalized with respect to the maximum power we see that the p mode peaks of the velocity spectrum have negative asymmetry (more power on the low frequency end of the peak) while the peaks of the intensity spectrum have positive asymmetry (more power on the high frequency end of the peak). In the velocity spectrum (Figure 2.1a), the asymmetry is strongest for low frequency (low radial order) modes and becomes negligible around and above the acoustic cutoff frequency ($\approx 5.2$ mHz). However, the asymmetry in the intensity oscillations (Figure 2.1b) increases with frequency for modes below the acoustic cutoff frequency, and then gradually decreases at higher frequencies. The intensity spectrum shows a higher noise level compared to the velocity spectrum.

Also in Figure 2.2 with the model of the additive background subtracted a notable shift in the peaks at the high frequency part of the intensity spectrum is seen in relation to the same part of the velocity spectrum. This frequency shift is particularly strong at and above the acoustic cutoff frequency. This is due to the fact that around the acoustic cutoff frequency, a transition from the dominance of well resonance to source resonance takes place (see section 2.2.3).

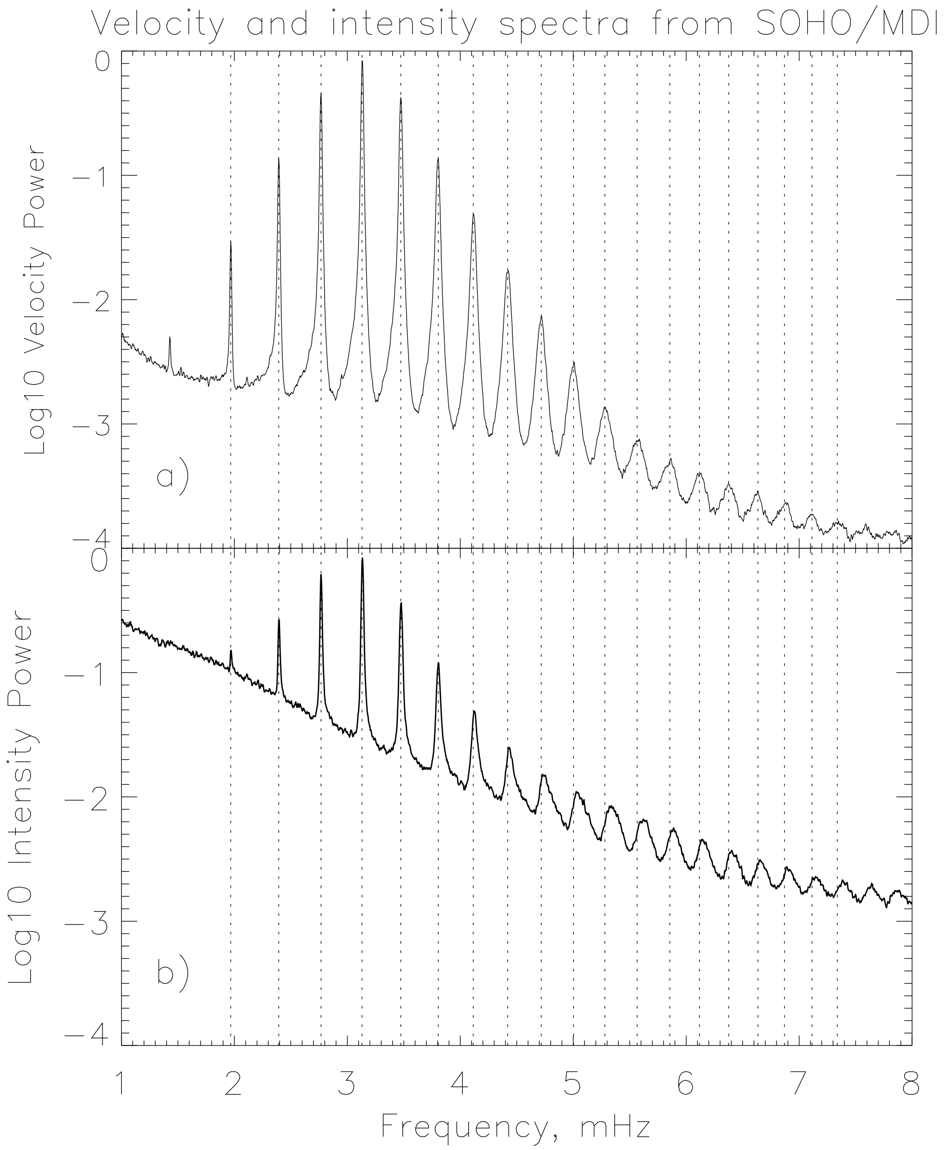

Figure 2.1: Normalized power spectra for solar oscillations of angular degree $l = 200$: a) Doppler velocity and b) continuum intensity for the same 3-day period of 21-23 July 1996. The leftmost peak of the velocity spectrum corresponds to the f mode. The other peaks of both spectra correspond to acoustic (p) modes of radial order from 1 to 21 (from the left to the right). The vertical dotted lines in both panels indicate the locations of the p mode maxima in the velocity power spectrum to show that a relative shift in frequency occurred at and above the acoustic cutoff frequency ($\approx$ 5.2 mHz).

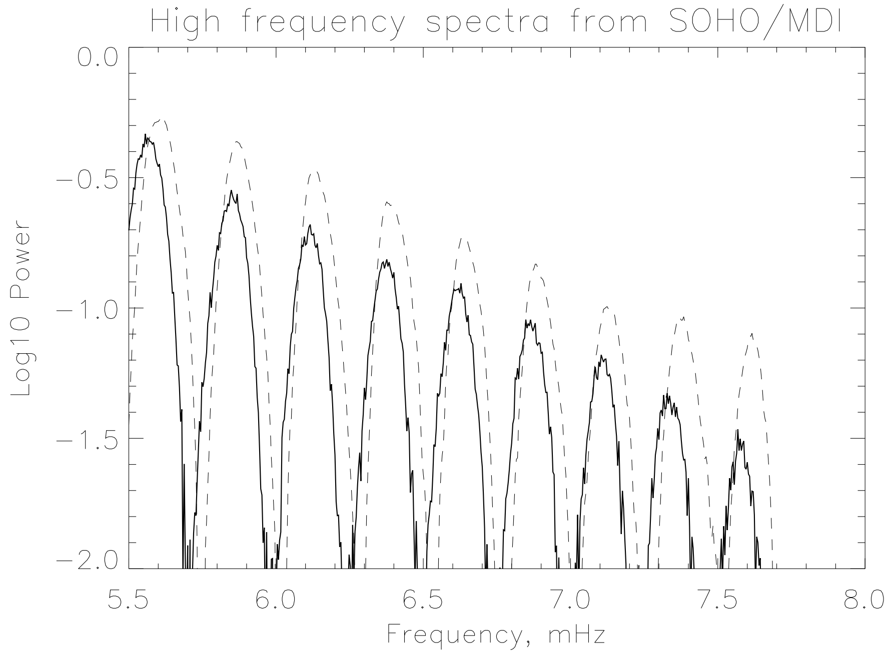

Figure 2.2: Normalized high frequency velocity (solid curve) and intensity power spectra (dashes) of Figure 1 with the model of the background subtracted. The relative shift in frequency is apparent.

The other modes in the medium-$l$ range (50-300) and in the high-$l$ range (300-1000) show similar properties of the line asymmetry. While the degree of the asymmetry varies across the spectrum, we have not yet detected a change in the sense of asymmetry with $l$. For $l = 200$ and higher there is reversal of asymmetry for the f mode in the velocity and intensity spectra just as in the case of p modes.

## 2.2 Why is the asymmetry reversed?

### 2.2.1 Numerical model of mode excitation

We assume that solar acoustic waves are generated by turbulence in the convection zone, and apply Lighthill's (1952) method described in chapter 1, in which the acoustic sources of various multipole orders are transferred to the right hand side of the wave equation (Moore and Spiegel, 1964), to calculate the velocity and pressure perturbations. We also assume that the observed intensity variations recorded by the MDI instrument correspond to Lagrangian pressure (or temperature) perturbations (Duvall et al., 1993); (Abrams and Kumar, 1996).

The background state is assumed to be spherically symmetrical, and all the perturbations are time harmonic. Dissipation is modeled by viscous damping. Then, using a standard decomposition onto spherical harmonics (Gough, 1993); (Gabriel, 1993) we transform Lighthill's equations of motion, continuity and energy (the full non-adiabatic problem is at least of the fourth order) into a simplified single second-order wave equation (see equation (1.30) in chapter 1)

$$\frac{d^2\Psi}{dr^2} + \left[\frac{\omega^2 - \omega_c^2}{c^2} - \frac{l(l+1)}{r^2}\left(1 - \frac{N^2}{\omega^2}\right)\right]\Psi = S[\boldsymbol{f}, q], \tag{2.1}$$

where $\Psi$ is proportional to the Lagrangian pressure perturbation $\delta p$ (Gough, 1993), $r$ is the radius, $\omega$ is the frequency, $\omega_c$ is the acoustic cutoff frequency, $c$ is the equilibrium sound speed, $N$ is the equilibrium buoyancy frequency, $S$ is a combination of source terms that include the fluctuating Reynolds stress force, $\boldsymbol{f}$ and the mass source, $q$. In this research, we consider a source given in equation (2.2) that is a combination of monopole (mass source) and dipole (Unno, 1964). The dipole part results when a monopole source is in a stratified medium and also from the radial and horizontal components of the Reynolds stress force. The radial component of the force is more dominant than its horizontal counterpart for data of medium angular degree $l$. The expression for $S$ is proportional to the sum of $q$, $\boldsymbol{f}$ and their respective derivatives with respect to $r$. This type of composite source gives a good match with the MDI intensity and velocity data, and is given by (see chapter 1 equation (1.31) and Appendix A.1, equation (A.9))

$$S(r, \omega) = \left[c_1\frac{dS_2}{dr} + c_2 S_2\right] + \left[c_3\frac{dS_1}{dr} + c_4 S_1\right], \tag{2.2}$$

where $c_1, c_2, c_3$ and $c_4$ depend on the solar model. $S_1$ is a source that contains the mass term and the horizontal component of the Reynolds stress force. $S_2$ contains the radial component of the Reynolds stress force. $S_1$ scales as $\omega^{-2}$ while $S_2$ does not contain $\omega$ explicitly as discussed in Kumar (1994).

The Green's function $G_\Psi(r, r_\mathrm{s})$ of equation (2.1) for a delta-function source at $r = r_\mathrm{s}$ using a standard solar model (Christensen-Dalsgaard et al., 1996), is found numerically using finite differences. The Sommerfeld radiation condition is applied above the upper turning point to ensure outgoing waves and $G_\Psi(r, r_\mathrm{s}) = 0$ at $r = 0$ as the perturbations are negligible much below the lower turning point. Damping is added by making the frequency complex, the imaginary part having the damping coefficient. Since the source is close to the surface, where dissipative effects vary with position, the damping coefficient is a function of position. Two kinds of damping, spatial, similar to Abrams and Kumar (1996), and temporal damping, were investigated. It is found that they have very little effect on line asymmetry. Damping basically effects the line width. The resulting system is a complex tridiagonal matrix equation which is solved by a standard routine (see Appendix A.2 for the numerical solution). To compare with the observations we multiplied the Green's function with a suitable source function and then added noise that was correlated with this source in a frequency dependent manner.

### 2.2.2 Effect of correlated noise

For the solar potential of the simplified model, the real part of the Green's function for the pressure perturbation is calculated from equation (2.1) and shown in Figure 2.3. It has been normalized with respect to its maximum value. The corresponding imaginary part is plotted in Figure 2.4. The intersection of the dashes with the Green's function (solid line) in Figure 2.3 correspond to points of zero amplitude, which result when there is no driving by the source.

The Lagrangian perturbations are then calculated from the Green's function for a single source location and source type by multiplying by a suitable source function and adding solar noise. The noise is assumed to consist of a part $c_\mathrm{p}(\nu)$ that is correlated with the source function $s(\nu)$, while $n_\mathrm{p}(\nu)$ forms the uncorrelated additive background. One then obtains for the pressure perturbation

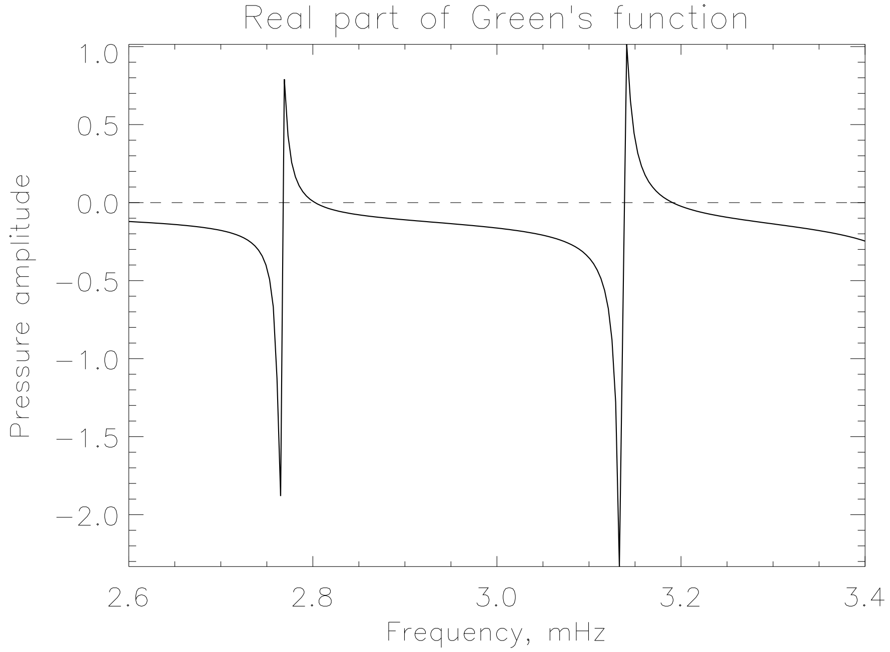

Figure 2.3: Real part of the normalized Green's function for solar p modes of angular degree $l = 200$ produced by a composite source located at a depth, $d = 75$ km beneath the photospheric level and an observing location $r_{\mathrm{obs}} = 300$ km above the photosphere, where the observed spectral line is formed, for pressure perturbation. Intersection of the dashes with the Green's function (solid line) correspond to the zero points. The correlated noise shifts these zero points and causes a reversal of asymmetry

$$p(\nu) = s(\nu)[c_{\mathrm{p}}(\nu) + G_{\mathrm{p}}(\nu)] + n_{\mathrm{p}}(\nu) \tag{2.3}$$

and the velocity perturbation is found in a similar manner. Equation (2.3) is a simple model of the observed solar signal, that includes the correlated noise. Here $G_{\mathrm{p}}$ is proportional to $G_{\Psi}$.

The asymmetry in velocity and intensity power spectra is of opposite sense because a component of the solar noise that is correlated with the source is present. The correlated component of the noise must remain below a certain threshold to preserve the asymmetry obtained by the above model in the velocity power spectrum yet be large enough to reverse the asymmetry in the intensity spectrum (Nigam et al.,

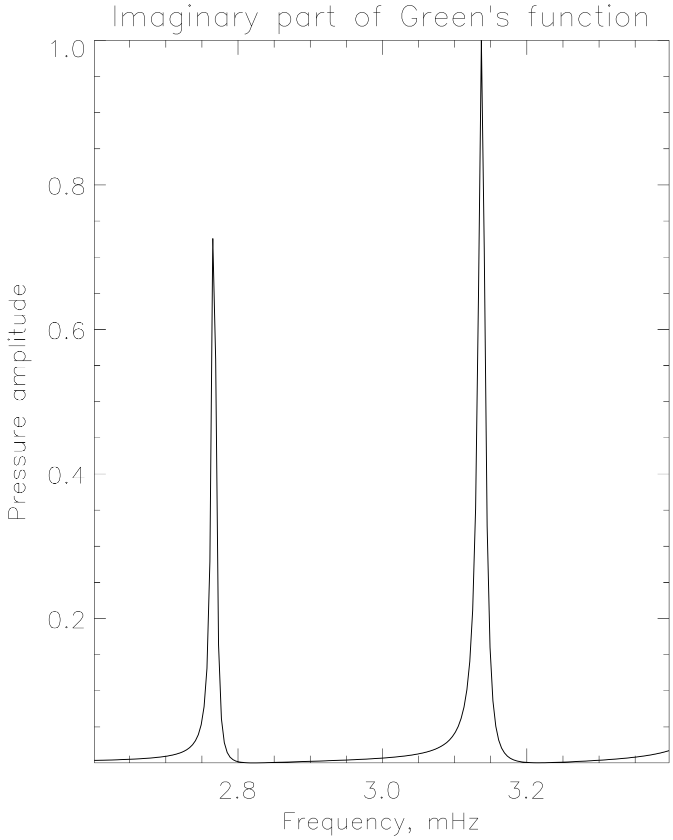

Figure 2.4: Imaginary part of the normalized Green's function for solar p modes of angular degree $l = 200$ produced by a composite source located at a depth, $d = 75$ km beneath the photospheric level and an observing location $r_{\rm obs} = 300$ km above the photosphere, where the observed spectral line is formed, for pressure perturbation.

1998). The source position $r_{\rm s}$ from the origin is kept fixed and the power spectrum is computed from equation (2.3) for the pressure perturbation. It is found that the correlation $c_{\rm p}(\nu)$ reverses the asymmetry found in $G_{\rm p}(\nu)$ when computing the power spectrum as seen from Figure 2.4b. This is due to the fact that $c_{\rm p}$ shifts the zero points in $G_{\rm p}(\nu)$. The uncorrelated noise plays no role in the reversal of asymmetry.

The intensity and velocity fluctuations are computed from the absorption line that is formed at a particular height in the solar atmosphere. The spectral line is effected by the p mode oscillations and the solar granulation, which modulate and shift the

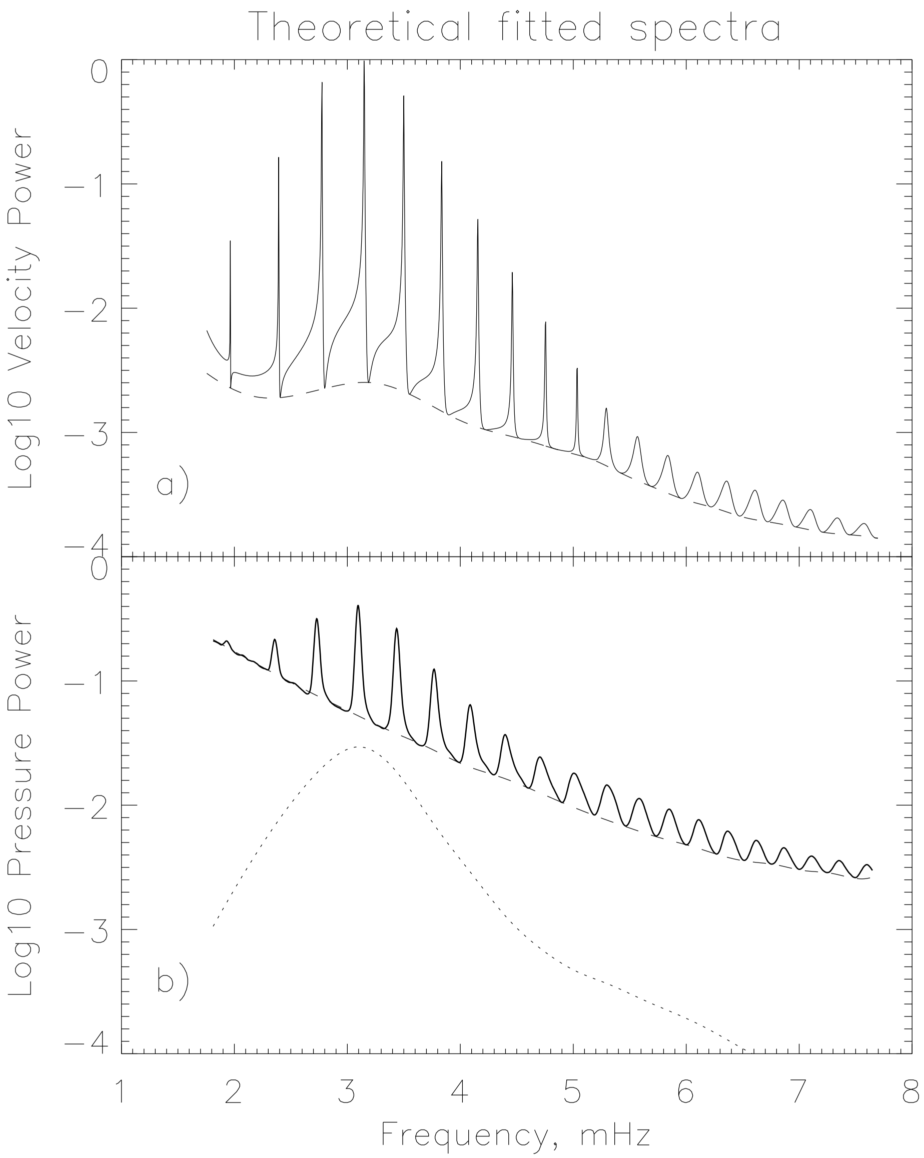

Figure 2.5: Normalized theoretical power spectra for solar p modes of angular degree $l = 200$ produced by a composite source: a) velocity spectrum (solid line) with additive uncorrelated noise (dashed line) and b) pressure spectrum (solid line) with additive correlated (dotted line) and uncorrelated noise (dashed line). The normalized correlated noise is multiplied by a factor of 5.

line. It is thus the granulation overshoot that forms the correlated component of the noise as it transports the effect of the source directly onto the line in the atmosphere. It also excites the solar oscillations in the intergranular lanes (Rimmele et al., 1995).

Without adding correlated noise no reversal in asymmetry can be brought about between intensity and velocity in this simplified second order problem. The full problem incorporating non-adiabatic effects and radiative transfer in an inhomogeneous turbulent medium is at least of the fourth order (Gabriel, 1998) and was discussed in Kumar (1994). However, the full problem remains unsolved and is a subject of future investigation. The effect of correlated noise may be built into the framework of the general problem, but is not present in the simplified second order equation. Therefore, we add noise to determine our solution.

For the theoretical velocity power spectrum (Figure 2.5a) corresponding to a delta-function source, the bound states (modes below the acoustic cutoff frequency $\approx 5.2$ mHz) show marked asymmetry that decreases with increasing frequency, while for the pressure power spectrum (Figure 2.5b), their asymmetry increases with frequency. The peaks of the bound states are close to the eigenfrequencies if damping is small as is the case for p modes. The leaky states (modes above the acoustic cutoff frequency) have less asymmetry and their peaks are mainly determined by the source position. They convey little information about the solar cavity as compared to the bound states. In Figure 2.6 we capture the high frequency shift that is present in the observations. Comparing the theoretical profiles with those in the observations, we find from Figures 2.1 and 2.5 that the profiles differ from the observations close to 3 mHz. Also, from Figures 2.2 and 2.6 we find that the power contrast (ratio of the maximum to minimum power) for the velocity spectrum is well reproduced but that for the pressure it is smaller than in the observations. This is due to the fact that we have used a simplified model of mode excitation and correlation. The correlation coefficient $c_{\mathrm{p}}$ for simplicity has been assumed to be a constant. Pressure and velocity perturbations for sources extended over a range of depths can then be calculated from the respective Green's function by linear superposition.

It is important to note that the narrow range of the acoustic source depth ($75 \pm 50$ km) found by comparing the theoretical and observed spectra coincides with the

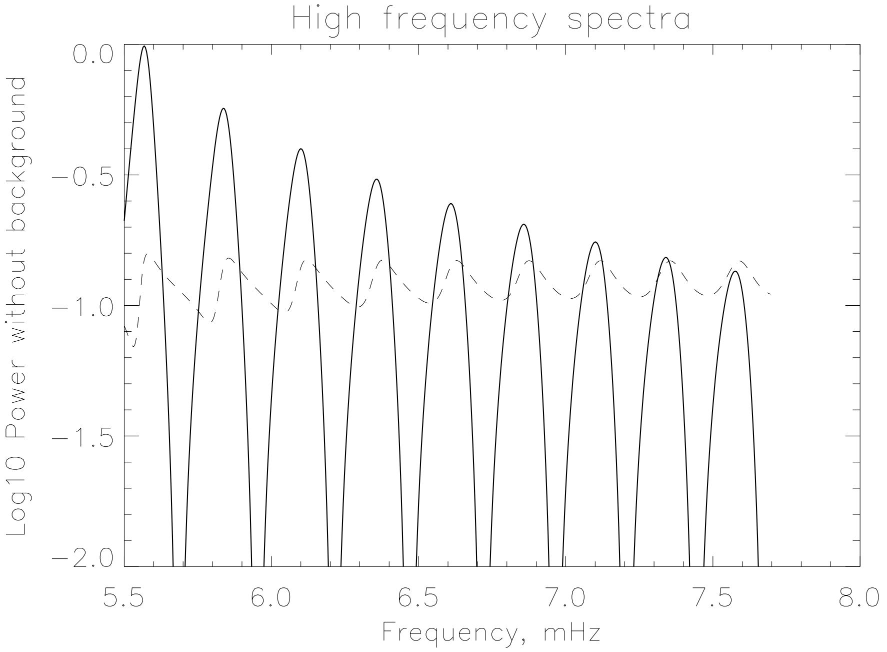

Figure 2.6: Normalized theoretical high frequency velocity (solid curve) and pressure power spectra (dashes) of Figure 2.4 with no additive uncorrelated noise. Correlated noise with coefficient $c_{\rm p}$ greater than a threshold value of 0.04 is responsible for the relative frequency shift that is present in the observations.

region of superadiabatic convection in the solar model (see Chapter 5). This region represents the highly unstable upper boundary layer of the convection zone where the convective motions are most violent. The extent of the source was determined by comparing the high frequency peaks of the theoretical spectra with those of the observations (Kumar and Lu, 1991), for a range of source depths.

### 2.2.3 Simple model of asymmetry

Solar p modes are formed by resonances of the acoustic cavity beneath the Sun's surface. The shape and size of the cavity depends on the stratification. However, some basic features of line asymmetry can be explained by approximating the cavity as a rectangular potential well $V(r)$ of width $a$ with an infinite potential at the lower turning point $r = 0$, and a finite height at the upper turning point $r = a$ (Stein, 1966);

(Nigam and Kosovichev, 1996); (Abrams and Kumar, 1996). This height corresponds to the square of the acoustic cutoff frequency $\nu_{\mathrm{c}}^2$ ($\nu_{\mathrm{c}} \equiv \omega_{\mathrm{c}}/2\pi$) while the width $a$ relates to the angular degree $l$ of the mode. For simplicity the effects of stratification have been neglected. The sound speed, $c$, is assumed to be constant in this problem. The effect of damping is included in the complex frequency $\omega_1^2 = (\omega^2 + i\omega\Gamma)$, the factor $\Gamma$ representing the damping coefficient and $\omega$ is the frequency. A delta-function source is placed at $r = r_{\mathrm{s}}$ inside the cavity. So, we write the reduced wave equation for the pressure perturbation:

$$\frac{d^2\Psi}{dr^2} + \frac{\omega_1^2 - V(r)}{c^2}\Psi = \delta(r - r_{\mathrm{s}}) \tag{2.4}$$

where $\Psi$ is proportional to the pressure perturbation.

Equation (2.4) is solved analytically (see Appendix A.3), using the boundary condition that $\Psi = 0$ at $r = 0$ and applying the Sommerfeld radiation condition far away from the upper turning point $r = a$. This gives the Green's function $G_\Psi$ for $\Psi$ (which is proportional to the pressure perturbation) at a particular observing point $r = r_{\mathrm{obs}}$; this can be taken to be at the upper turning point $r = a$ without loss of generality. If we define $\omega_2^2 = (\omega_c^2 - \omega_1^2)$, the Green's function can be written as (see Appendix A.3, equation (A.62))

$$G_\Psi(\omega_1) = \frac{-c\ \sin(\omega_1 r_{\mathrm{s}}/c)}{\omega_1 \cos(\omega_1 a/c) + \omega_2 \sin(\omega_1 a/c)} e^{-\omega_2 (r-a)/c} \tag{2.5}$$

In equation (2.5) the exponential term drops out when the observing point is at $r = a$.

Equation (2.5) can be written as

$$G_\Psi(\omega_1) = \frac{N_{\mathrm{s}}}{D_{\mathrm{w}}} \tag{2.6}$$

where $N_{\mathrm{s}}$ is the numerator of the Green's function which contains the effect of the source and $D_{\mathrm{w}}$ is the denominator of the Green's function which contains the effect of the cavity.

The power spectrum can be calculated from the above equation, by taking the absolute square of the numerator and denominator. In the numerator the maximum power occurs at the source resonance frequencies $\omega_{\mathrm{s}}$, as in Figure 2.7, while in the denominator the minimum power occurs at the well resonance frequency $\omega_{\mathrm{w}}$, which is the eigenfrequency (see Appendix A.4). The two separate resonances are due to interference, which in the simple problem are separable. At the frequency $\omega_{\mathrm{w}}$ the denominator is proportional to the damping coefficient, and this results in the peaks seen in the power spectra. It is the mismatch between these two power spectra from the numerator (solid curve in Figure 2.7) and the denominator (dotted curve in Figure 2.7) that makes the overall power spectra asymmetric (solid curve in Figure 2.8). Examination of the two effects separately shows that there is no asymmetry in either of them. A combination of the two effects leads to asymmetry. The maximum value of the power from the Green's function is close to the eigenfrequency. In the neighborhood of an eigenfrequency there are three cases that can arise: (i) Source resonance frequency $\omega_{\mathrm{s}} < \omega_{\mathrm{w}}$, this leads to negative asymmetry (ii) $\omega_{\mathrm{s}} = \omega_{\mathrm{w}}$, this leads to zero asymmetry (symmetry) and (iii) $\omega_{\mathrm{s}} > \omega_{\mathrm{w}}$, his leads to positive asymmetry. A physical measure of asymmetry is naturally the difference $\omega_{\mathrm{s}} - \omega_{\mathrm{w}}$. The eigenfrequency is a characteristic of the cavity and doesn't depend on the source position and nor on the particular representation of the acoustic disturbance.

One can also think of the source resonance in terms of zero points, which are the frequencies $\omega_{\mathrm{z}}$ for which the numerator power is zero. If we look at the Green's function, it is at these frequencies the function is zero (see Figures 2.7 and 2.8). At these frequencies $\omega_{\mathrm{z}}$, the overall power is zero. By adding correlated noise $N_{\mathrm{cor}}$ in equation (2.6), we get

$$G_{\Psi} + N_{\mathrm{cor}} = \frac{N_{\mathrm{s}} + N_{\mathrm{cor}} D_{\mathrm{w}}}{D_{\mathrm{w}}} \tag{2.7}$$

In equation (2.7) the numerator changes with respect to equation (2.6) , while the denominator remains the same. Due to this the zero points get shifted and hence reverse the asymmetry in the power spectrum of $|G_{\Psi} + N_{\mathrm{cor}}|^2$

Reversal of asymmetry can also be brought about by changing the source location $r_{\mathrm{s}}$ or changing the source type. The asymmetry reverses whenever the source crosses a node of the eigenfunction. Moving the source deeper and keeping everything else fixed

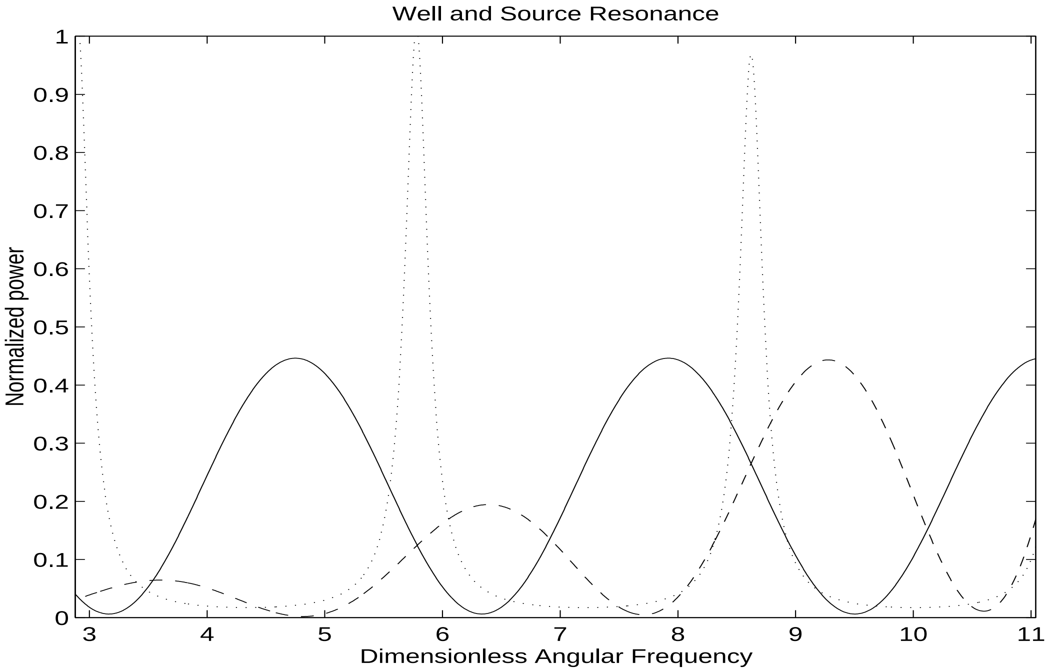

Figure 2.7: Normalized power (solid curve) from the numerator of the Green's function containing the effect of the source and no correlated noise. The dashes represent the effect of the correlated noise on the numerator, while the dotted curve is due to the well resonance, the reciprocal of the denominator of the Green's function are plotted as a function of the dimensionless angular frequency, $\omega a/c$. The peak is close to the eigenfrequency. The normalization is done with respect to the maximum value of the dotted curve.

reverses the asymmetry. Likewise, changing the source type (eg. monopole to dipole) also reverses the asymmetry. However, without adding correlated noise, these effects reverse the asymmetry in both the velocity and the pressure spectra simultaneously. This does not explain the puzzle.

## 2.3 Summary

In this chapter, we have given a possible explanation for the puzzle about the opposite sense of asymmetries between intensity and velocity power spectra. This will have an implication on the fitting and determination of eigenfrequencies from the observed

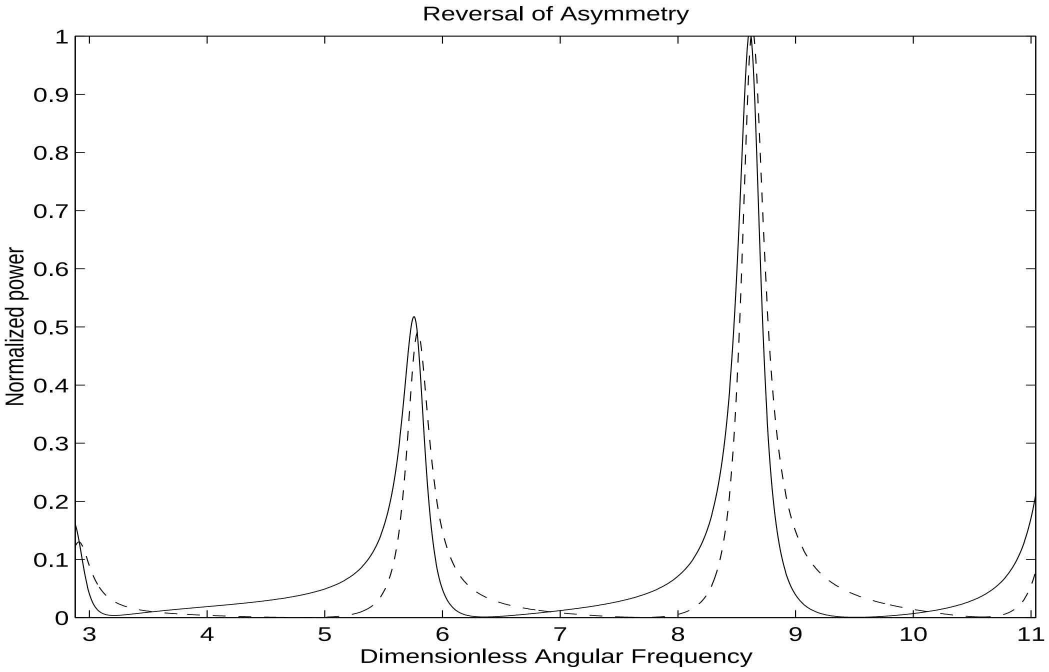

Figure 2.8: Normalized power with respect to the maximum (solid curve) without correlated noise of the Green's function, as a function of the dimensionless angular frequency, $\omega a/c$. Adding correlated noise shifts the zero points (the frequencies where the power is zero) in the power spectra and reverses the asymmetry (dashed curve).

spectra, which will in turn effect the inversions.

From our model we see that the intensity and velocity power spectra have opposite sense of asymmetry, because the solar noise is partly correlated with the source that is responsible for exciting the solar oscillations. The solar noise is made up of two parts: one which is correlated to the source and the other is the additive uncorrelated background. This also explains the appreciable frequency shift at and above the acoustic cutoff frequency, for the high frequency pseudo-modes, which are in fact responsible for the asymmetry of the bound states.

For a composite source the source depth is found to be in a thin layer $75 \pm 50$ km below the photosphere. It is remarkable that the theoretical spectra matches the observations when the source is placed within the superadiabatic layer, thus pinning down the location, extent and the nature of the source.

# Chapter 3

# Phase and Amplitude Differences

`(Part of this chapter is published in ApJ 1999, 510, L149)`

The phase difference between velocity and intensity is also linked to the excitation of p modes. Ground-based observations and analysis carried out by Deubner and Fleck (1989), Deubner et al. (1992) and space-based observations from MDI that were analyzed by Straus et al. (1998) revealed a velocity intensity a phase difference that is below 90 degrees along modal lines of the solar p mode spectra. Above the acoustic cutoff a non-zero phase difference is observed. But a simple adiabatic theory of solar oscillations predicts a phase difference of 90 degrees for modes below the acoustic cutoff frequency (bound states) and zero for modes above the acoustic cutoff frequency (scattered states). To explain this disagreement between theory and observations they suggested that continuous partial reflection of the waves in the solar atmosphere was responsible for the observed phase difference. A number of authors have studied this problem theoretically (Marmolino and Severino, 1991); (Wang et al., 1995). However, their models could not explain the unusual phase difference between velocity and intensity along modal lines. More recently, it was seen in the MDI data that at low frequencies the velocity has a higher power contrast than intensity, relative to the uncorrelated background. While at high frequencies above the acoustic cutoff, the continuum intensity shows higher power contrast relative to the uncorrelated background compared to the Doppler velocity, see Fig. 2.1 and Fig. 1 of Nigam et al. (1998). In addition, a puzzling shift between the maxima in the velocity and intensity high-frequency power spectra is observed in Fig. 2.6 (Nigam et al., 1998).

The phase difference between the intensity maximum and the radius minimum was discovered in Cepheid pulsation many decades ago. Subsequently, this difference (called the phase lag) has been determined for a large number of pulsating stars of different types. In these cases the phase lag is interpreted in terms of nonadiabatic effects and it is closely linked to the driving mechanism. Recently, Houdek et al. (1995) presented an attempt to explain the phase lag in the solar oscillations as a result of the nonadiabatic effects. In the solar case, this theory is far less reliable than in the case of Cepheids.

We propose that the phase difference and variation of power in the velocity and intensity spectra can be explained in the adiabatic approximation by the interaction of the p modes and part of the background noise that is correlated to the source responsible for exciting the waves. The correlated noise is also responsible for the reversal of asymmetry between velocity and intensity (Nigam et al., 1998). This result has been recently confirmed by Rast (1999) and Kumar and Basu (1999). The solar intensity and velocity oscillations are usually observed from variations in an absorption line. The intensity variations consist of two parts: solar oscillation modes and granulation noise. Since the oscillation modes are excited by granulation, the granulation signal (noise) is partially correlated with the oscillations. Thus, the observed intensity and to some extent, velocity variations, have a noise component which is caused directly by granulation and correlated to the oscillations.

## 3.1 Theoretical model

The Green's function for the potential well model described in section (2.2.3) given by equation (2.5) is (see Appendix A.3 for derivation)

$$G_{\Psi}(\omega_1) = \frac{-c\,\sin(\omega_1 r_{\rm s}/c)}{\omega_1 \cos(\omega_1 a/c) + \omega_2 \sin(\omega_1 a/c)} e^{-\omega_2 (r-a)/c} \tag{3.1}$$

For modes below the acoustic cutoff frequency the above equation can be simplified; and, taking into account the time dependence $e^{i\omega t}$, the pressure perturbation $\delta p$, that is taken as a proxy for the intensity fluctuations in the observations which are caused by the oscillations, is

$$\delta p \propto -\frac{\alpha c}{\omega_{\mathrm{c}}} e^{i\omega t} e^{-\omega_{\mathrm{c}}(r-a)/c} \tag{3.2}$$

where $\alpha$ is a complex analytical function of $\omega$, $a$, $r_{\mathrm{s}}$, $c$ and the damping. Using the equation of continuity, the velocity perturbation is

$$\delta v = \frac{\delta p\, \omega}{c\rho\omega_{\mathrm{c}}} e^{i\pi/2} \tag{3.3}$$

where $\rho$ is the density which has been assumed to be constant in this simple model (see Appendix B for details). Without loss of generality both the pressure and velocity perturbations are evaluated at the upper turning point $r = a$.

The cross spectrum (see Appendix B, equation (B.13) for its definition) between the velocity and pressure perturbations is calculated after adding correlated noise, and is,

$$S_{\mathrm{vp}} = (\delta v + N_{\mathrm{v,cor}})(\delta p + N_{\mathrm{p,cor}})^{*} + N_{\mathrm{v,uncor}} N^{*}_{\mathrm{p,uncor}} \tag{3.4}$$

where * refers to the complex conjugate. $N_{\mathrm{p,cor}}$ and $N_{\mathrm{v,cor}}$ are the complex correlated noise that are added to the pressure and velocity perturbations in equations (3.2) and (3.3) respectively, and $N_{\mathrm{p,uncor}}$ and $N_{\mathrm{v,uncor}}$ are the complex uncorrelated noise.

The phase of the cross spectra $S_{\mathrm{vp}}$ gives the phase difference between velocity and pressure, and is given by

$$\theta_{\mathrm{v-p}} = \arctan \frac{N_{\mathrm{i}} + \frac{\omega|\delta p|^2}{c\rho\omega_{\mathrm{c}}}}{N_{\mathrm{r}}} \tag{3.5}$$

where $N_{\mathrm{r}}$ and $N_{\mathrm{i}}$ are the real and imaginary parts of the terms in the cross spectra in equation (3.4) that contain the correlated noise, $(N^{*}_{\mathrm{p,cor}}\delta v + N_{\mathrm{v,cor}}\delta p^{*} + N_{\mathrm{v,cor}}N^{*}_{\mathrm{p,cor}} + N_{\mathrm{v,uncor}}N^{*}_{\mathrm{p,uncor}})$. They have dimensions of velocity times pressure.

From equation (3.5) it is evident that the phase difference $\theta_{\mathrm{v-p}}$ is related to the power $|\delta p|^2$. Since tan is a monotonic function in ($-\pi/2$, $\pi/2$), the phase difference rises and falls whenever the power jumps and falls, which happens whenever a mode is present in the vicinity of an eigenfrequency. Thus, the interaction of the correlated noise with the mode explains the unusual phase difference along modal lines. In between the modes the phase difference is due to the presence of both correlated and uncorrelated noise. In the absence of noise the phase difference $\theta_{\mathrm{v-p}}$ is 90 degrees everywhere, both along and in between modal lines, which follows from equation (3.5).

For modes above the acoustic cutoff frequency, equation (3.1) is simplified for the pressure perturbation,

$$\delta p \propto -\frac{c}{\omega}\sin(\omega r_{\mathrm{s}}/c)e^{i\omega t}e^{-i\omega r/c} \tag{3.6}$$

and the velocity perturbation is given by,

$$\delta v = \frac{\delta p}{c\rho} \tag{3.7}$$

The phase difference between velocity and intensity for the scattered states is given by,

$$\theta_{\mathrm{v-p}} = \arctan\frac{N_{\mathrm{i}}}{N_{\mathrm{r}} + \frac{|\delta p|^2}{c\rho}} \tag{3.8}$$

In the absence of noise in equation (3.8) the phase difference is zero. The bound states show a 90 degrees phase difference, which is the case for standing waves. On the other hand, scattered states show a 0 degree phase difference, which is true for propagating waves.

The power contrast of the power of quantity $\psi$ ($p$ or $v$), $P_\psi$, relative to the power of the uncorrelated background $P_{\psi,\mathrm{uncor}}$, is $C_\psi$ and is given by (see Appendix B)

$$C_\psi = |\delta\psi|^2/P_{\psi,\mathrm{uncor}} + \beta_\psi[1 + 2\mathrm{Re}(\delta\psi/N_{\psi,\mathrm{cor}})] \tag{3.9}$$

where $\psi$ can be $p$ or $v$, $\beta_\psi = |N_{\psi,\mathrm{cor}}|^2/P_{\psi,\mathrm{uncor}}$ is the ratio of the power of correlated, $|N_{\psi,\mathrm{cor}}|^2$, to uncorrelated noise, and $C_\psi = P_\psi/P_{\psi,\mathrm{uncor}}$.

In Figure 3.1 the power spectra for velocity and pressure is computed for the potential well model. By adding both correlated and uncorrelated noise to both velocity and pressure, we see that the power contrast in the velocity power spectrum is higher at low frequencies and falls off rapidly at higher frequencies in comparison to the pressure power spectrum. To see this we assume that the correlated noise in the velocity is negligible and set $\beta_v = 0$ in equation (3.9), therefore the power contrast for the velocity is proportional to $|\delta v|^2/P_{\mathrm{v,uncor}}$, which rapidly decreases at higher frequencies, as the waves are no longer trapped. In the case of the pressure perturbation from equation (3.9) the power contrast has additional terms involving $\beta_p$. Due to the presence of these additional terms the pressure power contrast does not fall off rapidly as compared to the velocity power contrast. It is also seen that the presence of correlated noise is responsible for the reversal of asymmetry and also the high frequency shift between velocity and pressure (Nigam et al., 1998).

## 3.2 Comparison of the Numerical Model and Observations

Velocity and pressure perturbations are generated numerically from the Green's function for the reduced wave equation as described in Chapter 2, (see also Appendix A.2) using a standard solar model (Christensen-Dalsgaard et al., 1996). In order to compare with the MDI observations, noise is added to the computed perturbations. We took an example of angular degree $l = 200$ and angular order $m = 81$. Other modes in the MDI data behave similarly. From this the cross spectrum between velocity and pressure for the bound states is computed. The amplitude (absolute value) and phase of the cross spectra are plotted in Figure 3.2. A similar plot is made for the cross spectrum after smoothing the MDI data in Figure 3.3. By adjusting the noise the observed phase jump in Figure 3.3b between velocity and intensity along modal lines is reproduced in the theoretical plot in Figure 3.2b (black curve). The correlated noise is close to zero in the velocity perturbation. We find that the phase difference is below 90 degrees. While the unusual behavior of the phase along modal lines has been explained in the discussion of equation (3.5), from which we see that in the vicinity of an eigenfrequency the power rises and falls, and hence the phase rises and

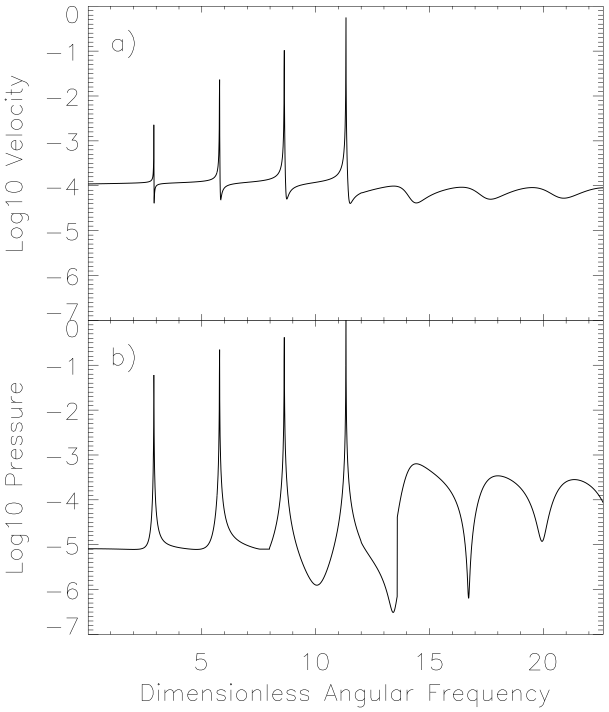

Figure 3.1: Normalized (with respect to its maximum) (a) velocity and (b) pressure power spectra computed for the potential well model as a function of the dimensionless angular frequency, $\omega a/c$.

falls. The scattered states show a non-zero phase difference. Without noise, no such jumps in the phase are seen, and the phase is constant at 90 degrees.

The effect of the correlated noise is modeled by adding a complex function whose real and imaginary parts depend on the characteristics of granulation, convection and time delay between exciting the waves and observing the disturbance caused by the oscillations on the surface (Rast, 1999). Complex uncorrelated noise is also added. From Figure 3.2a we find that increasing the absolute level of the correlated noise, the modulus of the cross spectrum increases. Where as from Figure 3.2b we observe that the phase difference is sensitive to the imaginary part of the correlated noise. If

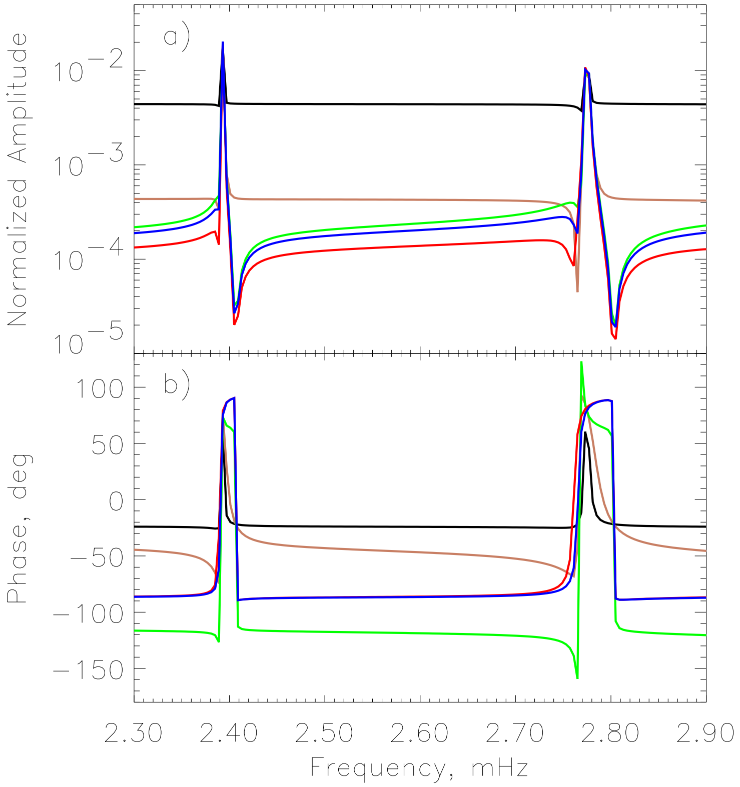

Figure 3.2: (a) Normalized (with respect to its maximum) absolute value and (b) phase of the theoretical cross spectrum between velocity and pressure for the bound states computed for a standard solar model for $l = 200$, showing two modal lines $n = 2$ and 3 (corresponding eigenfrequencies $\approx 2.392$ and 2.766 mHz respectively). The black curve, which matches the data best corresponds to $N_{\rm p,cor} = -0.3 - i\,0.2$, $N_{\rm p,uncor} = 0.3 + i\,0.7$, $N_{\rm v,uncor} = 0.016 + i\,0.016$; the brown curve is for $N_{\rm p,uncor} = 0.03 + i\,0.07$, the uncorrelated noise for the velocity and correlated noise for pressure are the same as the black curve. The green curve is for $N_{\rm p,cor} = -0.4 - i\,0.2$ and no uncorrelated noise; red and blue curves correspond to purely real values of correlated noise -0.3 and -0.4 respectively for pressure and no uncorrelated noise. The level of correlated noise is negligible in velocity in the above curves. All the values have been normalized with respect to the maximum value of the real part of the respective perturbations in this frequency range.

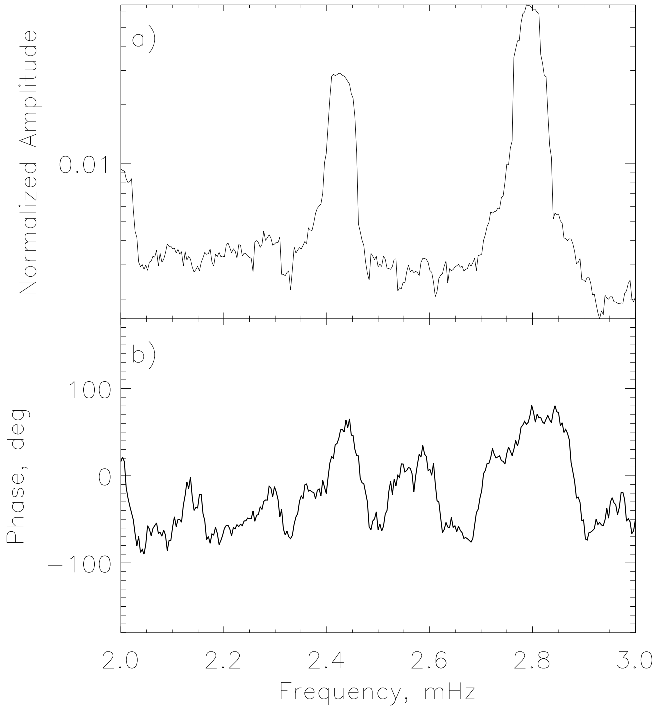

Figure 3.3: (a) Normalized (with respect to its maximum) absolute value and (b) phase of the cross spectrum between velocity and intensity for the smoothed SOI/MDI data for $l = 200$, $m = 81$ showing two modal lines $n = 2$ and 3 as in Fig. 3.2. The phase difference is below 90 degrees.

the imaginary part is set equal to zero, the phase difference is not sensitive to changes in the real part, as seen by the blue and red curves, which coincide.

## 3.3 Summary

We have explained the unusual phase difference that is below 90 degrees between velocity and intensity spectra. By adding correlated and uncorrelated noise we are able to reproduce the phase jump along modal lines. The deviation of the phase difference from 90 degrees, that is predicted by simple adiabatic solar oscillation theory was puzzling for many years. The phase difference depends on the power spectrum, which jumps whenever an eigenfrequency is approached. The high frequency modes show a non-zero phase difference which is different from the zero phase difference predicted theoretically. Taking into account the correlated noise whose level happens to be higher in the pressure spectrum compared to the velocity, we are able to explain the high power contrast in the velocity power spectrum at low frequencies and its rapid drop off at frequencies above the cutoff frequency, in comparison to the intensity. Studying the asymmetry, the high-frequency shift, the amplitude and the phase difference between velocity and intensity is a useful diagnostic to measure the level and phase of the correlated noise in the data, and also understand the mechanism of mode excitation of solar oscillations.

# Chapter 4

# Asymmetric Fitting Formula

`(Part of this chapter is published in ApJ 1998, 505, L51 and ApJ 1998, 506, L147)`

An asymmetric fitting formula is derived to measure the eigenfrequencies. The principal goal of helioseismology is to infer the internal structure and rotation of the Sun from the observed eigenfrequencies of the normal modes of oscillation. Solar eigenfrequencies are generally determined by assuming that the power spectrum is symmetric and can be fitted by a Lorentzian. This is clearly not the case. Recent studies (Duvall et al., 1993); (Gabriel, 1993); (Abrams and Kumar, 1996); (Roxburgh and Vorontsov, 1997); (Nigam et al., 1998); (Rosenthal, 1998) have shown that the peaks in the power spectra are asymmetric. The asymmetry may be caused by interference between an outward-directed wave from the source and a corresponding inward-directed wave that passes through the region of wave propagation. Also important is the interaction between the wave and part of the background noise that is correlated to the source responsible for exciting the waves. The solar intensity and velocity oscillations are usually observed from variations in an absorption line. These variations consist of two parts: solar oscillation modes and granulation noise. Because the oscillation modes are excited by granulation, the granulation signal (noise) is partially correlated with the oscillations. According to Goode et al. (1998) the solar oscillations are excited in the intergranular dark lanes. Thus, the observed intensity and velocity variations have a noise component which is caused directly by the dark lanes and correlated to the amplitude of the oscillations. The absorption line is affected by the p mode oscillations and the solar granulation, (due to intensity fluctuations and overshoot) which modulate and shift the line. More specifically, the intensity fluctuations form the correlated component of the noise that is responsible for the reversal of asymmetry in the intensity power spectrum.

Line asymmetry in the solar power spectra alters the frequencies which are obtained under the assumption that the lines are symmetric. It has been observed (Rhodes et al., 1997) that when asymmetric line profiles of the velocity data are fitted with a symmetric formula, the resulting frequency is shifted by a significant amount. The affect of asymmetry was first observed by Toutain (1993) and later he observed frequency differences of the order of 0.1 $\mu$Hz (Toutain et al., 1997) between intensity and velocity, for modes of low angular degree when Lorentzian fits are performed. This suggests that an asymmetric fitting formula should be used to measure solar eigenfrequencies instead of the usual Lorentzian fits.

In §4.2 we describe an asymmetric fitting formula that was derived from a physical understanding of asymmetry. The derivation takes into account the reversal of asymmetry between velocity and intensity when correlated noise is present in the data (Nigam and Kosovichev, 1998). The correlated noise is above a certain threshold to reverse the asymmetry in the intensity power spectrum but is small in the velocity spectrum so as to preserve its asymmetry. We use a simple model to derive an analytical fitting formula, as the full solar model is complicated and has to be dealt with numerically. In §4.3 we use our formula to fit both the theoretical velocity and pressure (intensity) spectra. This is compared with a symmetric Lorentzian fit, and deviations from the computed theoretical eigenfrequencies are discussed. In §4.4 we repeat the fits for the medium $l$ MDI data and in §4.5 they are applied to the low $l$ data from MDI and VIRGO instruments.

## 4.1 Derivation of the Formula

The Green's function for the potential well model from equation (2.5) in chapter 2 is

$$G_\Psi(\omega_1) = \frac{-c\,\sin(\omega_1 r_\mathrm{s}/c)}{\omega_1\cos(\omega_1 a/c) + \omega_2\sin(\omega_1 a/c)} e^{-\omega_2(r-a)/c} \tag{4.1}$$

A new formula to fit the bound states (modes with frequencies less than the acoustic cutoff frequency) is derived from equation (4.1). In the derivation it is assumed that the damping is much smaller than the frequency, which is true of the solar p modes. We next substitute the expressions for $\omega_1$ and $\omega_2$ into equation (4.1), and expand for small $\Gamma$. Making use of the eigenvalue condition at $\omega = \omega_0$: $\omega\cos(\omega a/c) + w\sin(\omega a/c) = 0$, (where $w^2 = \omega_\mathrm{c}^2 - \omega^2$) (see Appendix A.4) we get the complex amplitude of the pressure perturbation $A_\Psi$ (see Appendix C.1, equation (C.25))

$$A_\Psi(X) = -A_\mathrm{w}\frac{\sin(\beta X - p_\mathrm{w}) + \frac{i}{2}\beta\cos(\beta X - p_\mathrm{w})}{\sin(\beta X) + \frac{i}{2}\beta\cos(\beta X)} \tag{4.2}$$

Here $X = (\omega - \omega_0)/\Gamma$, $\beta = a\Gamma/c$, $A_\mathrm{w} = A_0 c/\omega_\mathrm{c}$, $A_0$ is the mode amplitude that has been multiplied by the Green's function, $p_\mathrm{w} = p_0 + \phi_\mathrm{c}$, $p_0 = \omega_0 d_\mathrm{s}/c$, $\sin\phi_\mathrm{c} \approx \omega/\omega_\mathrm{c}$ and $d_\mathrm{s} = a - r_\mathrm{s}$ is the depth of the source below the upper turning point. To explain the reversal of asymmetry between velocity and intensity (equivalent to the pressure perturbation), correlated noise $N_\mathrm{cor}$ which is due to the granulation is added to the amplitude signal $A_\Psi$ (Nigam and Kosovichev, 1998). The power is then given by $P = |N_\mathrm{cor} + A_\Psi|^2$. This gives a trigonometric expression for the power, that can be used to fit the peaks and troughs (minimum points in the power spectra) in the power spectra (see Appendix C.1, equation (C.28)) and is

$$P(x) \approx A\frac{[U\cos(Ux) + B\sin(Ux)]^2 + B^2U^2\cos^2(Ux)}{U^2\cos^2(Ux) + \sin^2(Ux)} \tag{4.3}$$

Where $x = 2(\nu - \nu_0)/\gamma$, cyclic frequency $\nu = \omega/2\pi$, $\gamma = \Gamma/2\pi$,$A = 4A_\mathrm{w}^2(1 - q_\mathrm{w}^2)\beta^{-2}$, $B = 0.5\beta(N_\mathrm{cor} - A_\mathrm{w}q_\mathrm{w})A_\mathrm{w}^{-1}(1 - q_\mathrm{w}^2)^{-1/2}$, $q_\mathrm{w} = \cos p_\mathrm{w}$ and $U = \beta/2$ is a dimensionless quantity. Here $\beta$ is the product of the damping $\Gamma$ (mode line width) and the travel time $a/c$ of the p modes between the upper and lower turning points. $U$ is generally small for the solar case. The trigonometric formula in equation (4.3) can be used to fit multiple peaks, in this case the travel time can be written in terms of the mode spacing $\Delta\nu$ between radial orders of constant angular degree $l$. The expression for $U$ is $\pi\gamma/2\Delta\nu$.

This expression for the power can be expanded for small $Ux$ to give a more practical polynomial formula,

$$P(x) \approx A\frac{(1+Bx)^2 + B^2}{1+x^2} + B_{\mathrm{l}} \tag{4.4}$$

Here $B_{\mathrm{l}}$ is the uncorrelated linear background and $N_{\mathrm{cor}}$ is the correlated noise. In using equation (4.4) as a fitting formula for the line profile the fit parameters are $A, B$, the damping $\gamma$ (which is related to the mode linewidth), and the eigenfrequency $\nu_0$. The parameter $B$ controls the asymmetry. It is positive for positive asymmetry (more power on the higher frequency end of the peak) and negative for negative asymmetry (more power on the lower frequency end of the peak). It contains the effects of correlated noise and the source, the two factors that are responsible for asymmetry. The sign of $B$ changes when $N_{\mathrm{cor}}$ changes sign. When $B = 0$ (absence of asymmetry) the first term in equation (4.4) reduces to the usual Lorentzian profile. Without correlated noise the frequencies of the troughs in the power spectra are determined by the source characteristics and the solar structure. Adding correlated noise shifts these frequencies.

Other workers have derived fitting formulae (Duvall et al., 1993); (Gabriel, 1995); (Appourchaux et al., 1995b); (Abrams and Kumar, 1996); (Rhodes et al., 1997); (Rosenthal, 1998), but their models do not explain the reversal of asymmetry between velocity and intensity. For instance, the polynomial line fitting formula derived by Rosenthal (1998), equation (45), is different from our formula in equation (4.4), as his formula does not contain correlated noise, which is responsible for the reversal of asymmetry between intensity and velocity. Other important features of our profile, equation (4.4) are that it is always positive and as shown below matches the theoretical power spectra from a standard solar model and the MDI observations quite well.

## 4.2 Fitting of Velocity and Pressure Theoretical Power Spectra

A simultaneous fit of the velocity and pressure spectra of angular degree $l = 200$ is performed using the above formula. The fitting is carried out using a standard nonlinear minimization algorithm. We minimize the chi-square error, defined as the square of the difference between the power estimated by the above formula and that from the theoretical power spectra, summed over a suitable frequency range so as to isolate the mode (see Appendix C.2). The theoretical power spectra are generated from the Green's function for the reduced wave equation as described in Nigam et al. (1998). For modes of medium angular degree $l$, the effects of spherical geometry can be neglected. In the plane parallel approximation, the reduced wave equation can be written using equations (1.30) and (1.43)

$$\frac{d^2\Psi}{dr^2} + \frac{\omega_1^2 - \omega_+^2}{c^2}\Psi = S[\boldsymbol{f}, q], \tag{4.5}$$

where $\Psi$ is proportional to the Lagrangian pressure perturbation $\delta p$, $r$ is the radius, $\omega$ is the frequency and $c$ is the equilibrium sound speed. In equation (4.5) $\omega_+^2$ plays the role of the acoustic potential (Gough, 1993) and is calculated from a solar model using equation (1.38). For the acoustic modes we neglect $\omega_-^2$ in equation (1.37), as it is very small compared to $\omega_+^2$. Both $\omega_+$ and $c$ are functions of radius. $S$ is a combination of source terms that include the fluctuating Reynolds stress force, $\boldsymbol{f}$, and the mass source, $q$. The Green's function $G_\Psi(r, r_\mathrm{s})$ of equation (4.5), for a delta-function source at $r = r_\mathrm{s}$ is found numerically using a standard solar model (Christensen-Dalsgaard et al., 1996). We use reflecting boundary conditions at the lower and upper turning points. To the Green's function we add the noise $N_\mathrm{cor}(\nu)$, which is correlated with the source function $s(\nu)$, and uncorrelated noise $B_\mathrm{l}(\nu)$. One then obtains for the pressure perturbation, which serves as a proxy for the intensity observations.

$$p(\nu) = s(\nu)[N_\mathrm{cor}(\nu) + G_\mathrm{p}(\nu)] + B_\mathrm{l}(\nu) \tag{4.6}$$

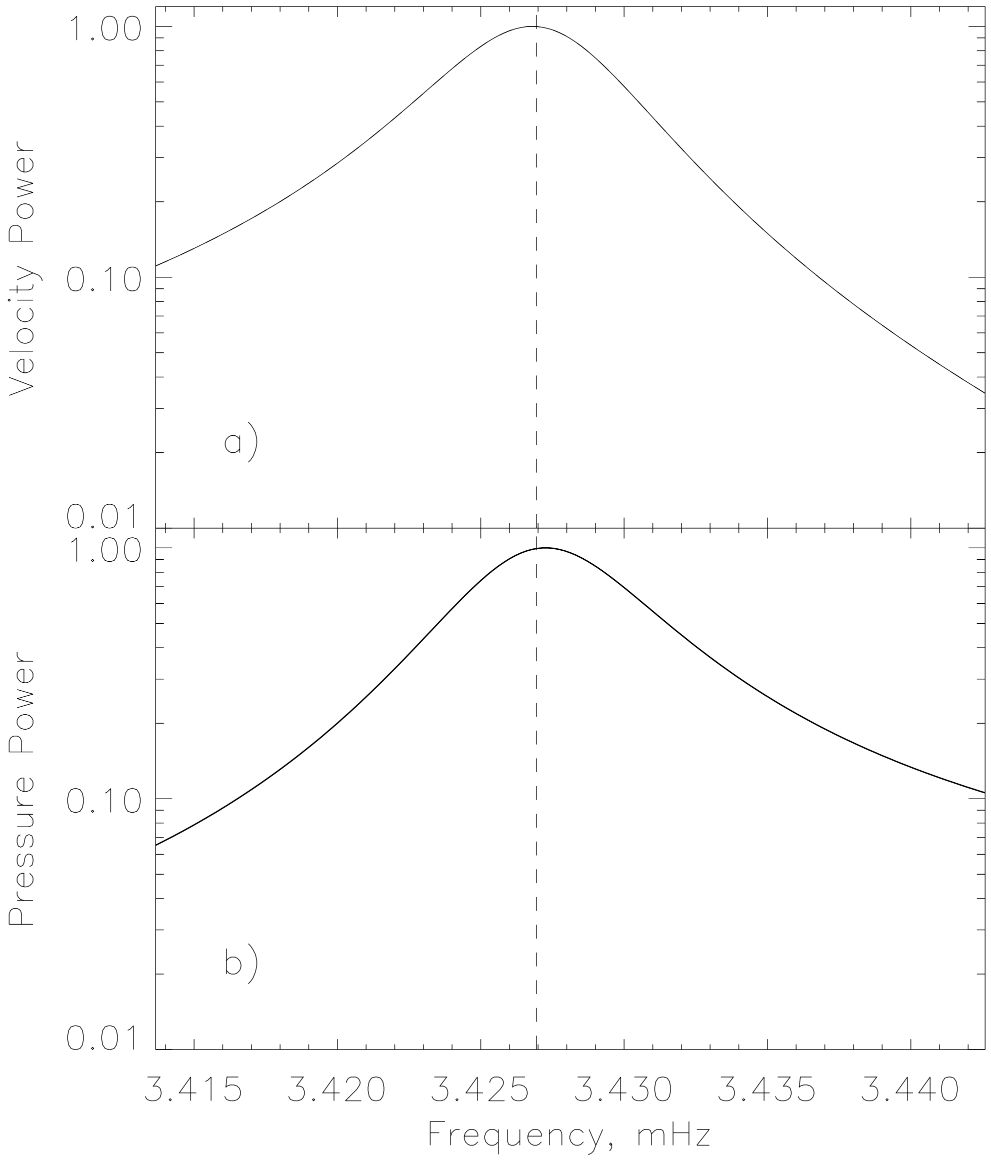

Figure 4.1: Asymmetrical fit for the $l = 200$, $n = 5$ theoretical power spectra (log scale) that has been normalized with respect to its maximum value: (a) Velocity spectrum and (b) Pressure spectrum. The dashed lines show the computed eigenfrequency. The fitted profile is indistinguishable from the theoretical profile, with a maximum deviation of 0.003%.

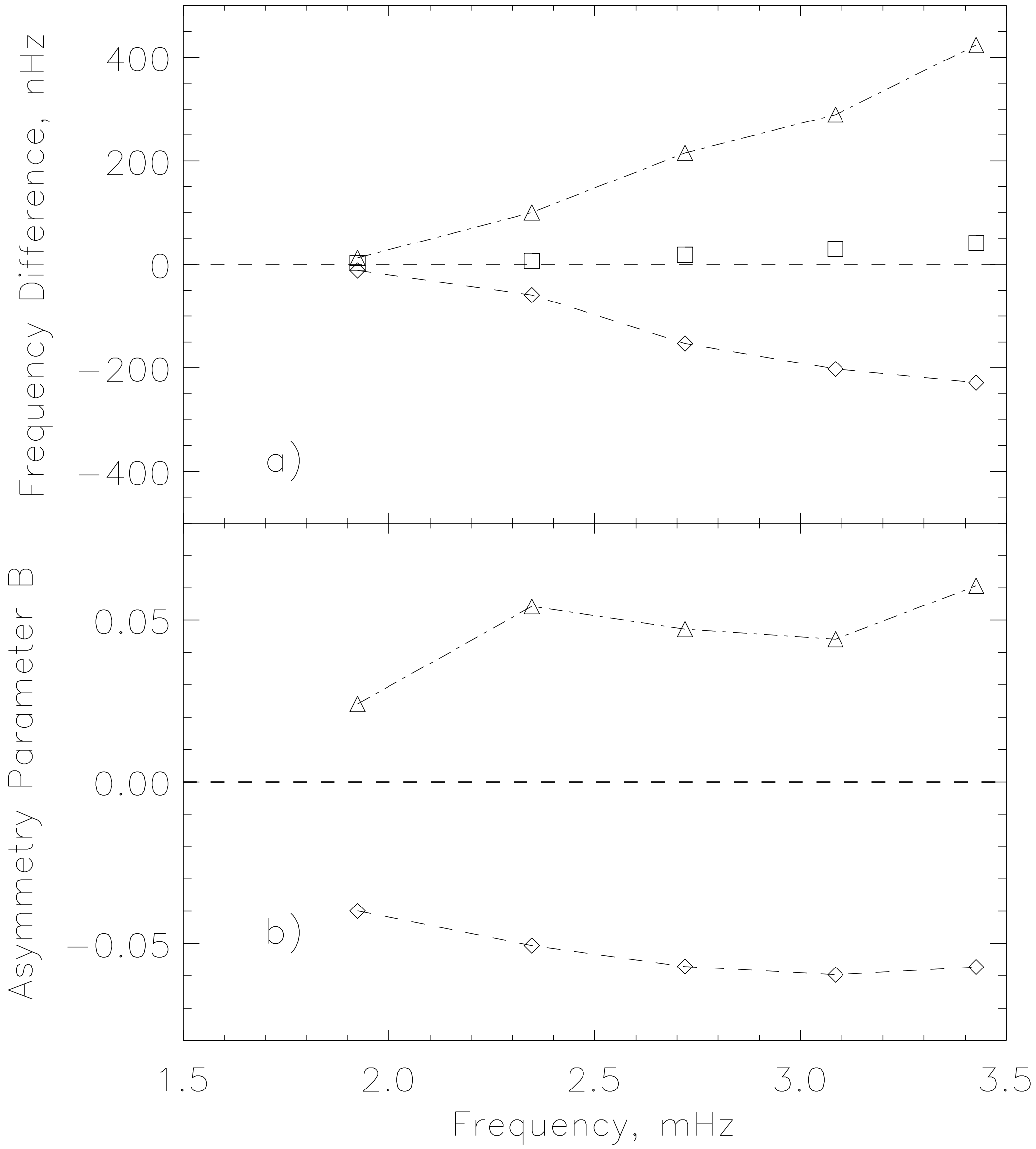

Figure 4.2: (a) Squares denote the deviation (in nHz) of the asymmetrical fitted frequencies from the computed eigenfrequencies, triangles are the deviation of the Lorentzian fitted frequencies of the theoretical pressure power spectrum for $l = 200$ and the diamonds are the deviation of the Lorentzian fitted frequencies of the velocity power spectrum from the computed eigenfrequencies. (b) Triangles represent the dimensionless asymmetry parameter B for the pressure power spectrum and the diamonds for the velocity power spectrum.

where $G_{\mathrm{p}}$ is proportional to $G_{\Psi}$. The power spectrum for the pressure perturbation is calculated from the function $p(\nu)$, see Fig. 2.5b. This equation is same as equation (2.3) in chapter 2 with $B_{\mathrm{l}}(\nu) = n_{\mathrm{p}}(\nu)$. The velocity power spectrum is found in a similar manner, from the complex velocity amplitude (Appendix D, equation (D.25)).

The eigenfrequencies $\omega_0$ of the solar model are determined numerically from equation (4.5) with no source term (see Appendix C.3).

The first five modes (bound states with frequencies less than the acoustic cutoff frequency) of the two spectra are fitted using both the asymmetrical formula and the Lorentzian profile. The fitting algorithm converges rapidly to the same fitted frequency for both the velocity and pressure power spectra when the asymmetric formula is used. This is not the case for the Lorentzian fits, where the convergence is slow. The asymmetrical fit for $n = 5$ is shown, along with the computed eigenfrequency, in Figure 4.1. The fits are indistinguishable from the theoretical spectra, with a maximum deviation of 0.003%. The resulting fitted frequencies are then compared with the computed eigenfrequencies in Figure 4.2a. We see the deviation from the true eigenfrequencies is more pronounced for the Lorentzian fit than for the asymmetrical formula, which yields values very close to the eigenfrequencies.

In Figure 4.2b we show the asymmetry parameter $B$ for the five modes. The asymmetry parameter is negative for the velocity and positive for the pressure power spectra. This difference in asymmetry is also observed in real solar power spectra.

The good agreement obtained using equation (4.4) as a fitting formula means that the formula although derived for a simple potential, is sufficiently accurate for a realistic solar model.

## 4.3 Fitting of Velocity and Intensity MDI Power Spectra

To carry out a simultaneous fit of the $m$-averaged velocity and intensity spectra we compute spherical harmonic transforms (SHTs) of full disk velocity and intensity images from the MDI instrument (Scherrer et al., 1995). After filling gaps in the

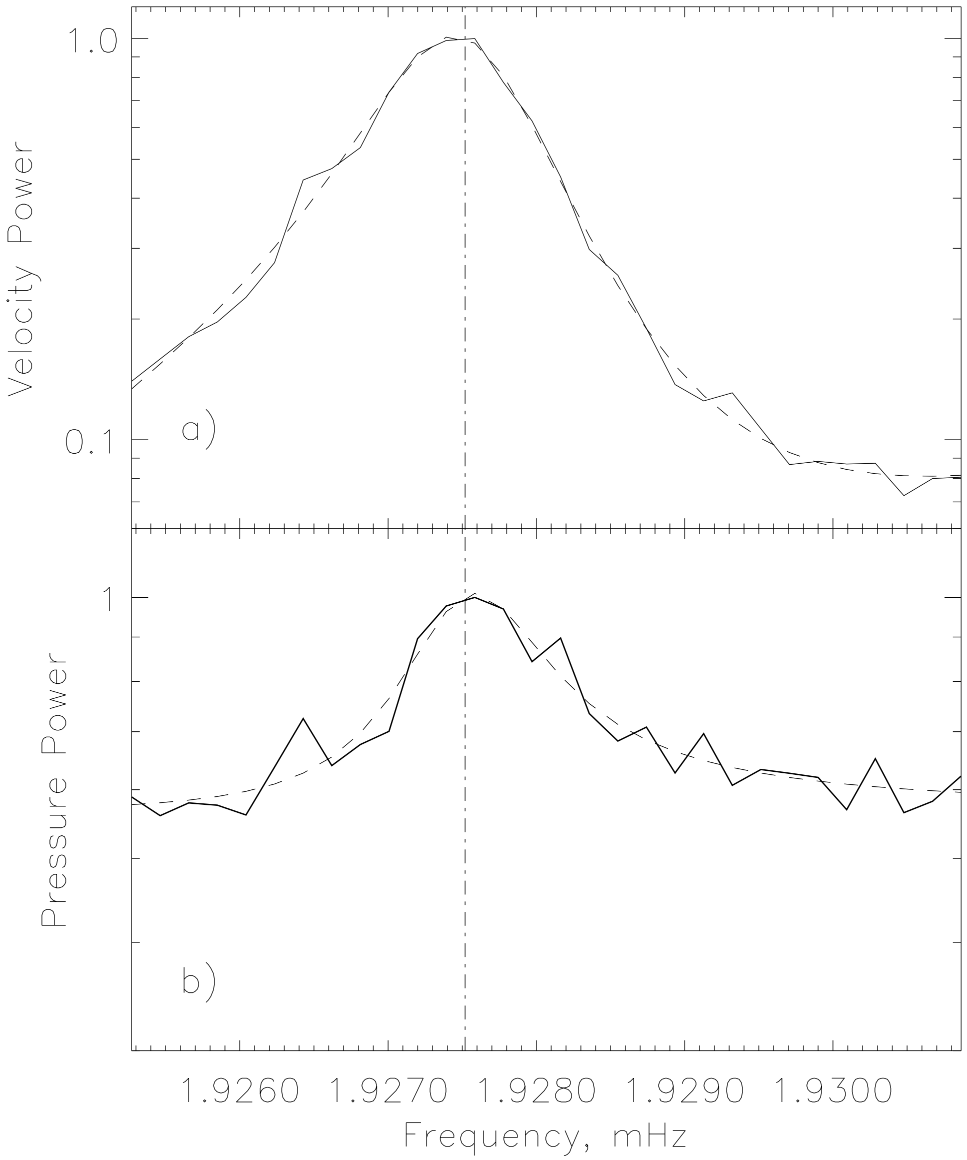

Figure 4.3: Asymmetrical fit for the $l = 75$, $n = 3$ MDI power spectra (log scale) that has been normalized with respect to its maximum value. Solid curve is the MDI spectra and the dashed one is the fit. (a) Doppler velocity and (b) Continuum intensity. The dotted lines show the fitted eigenfrequency, which is the average of the velocity and intensity fits. It can be seen that the fits are reasonably good, with a maximum deviation of 10%.

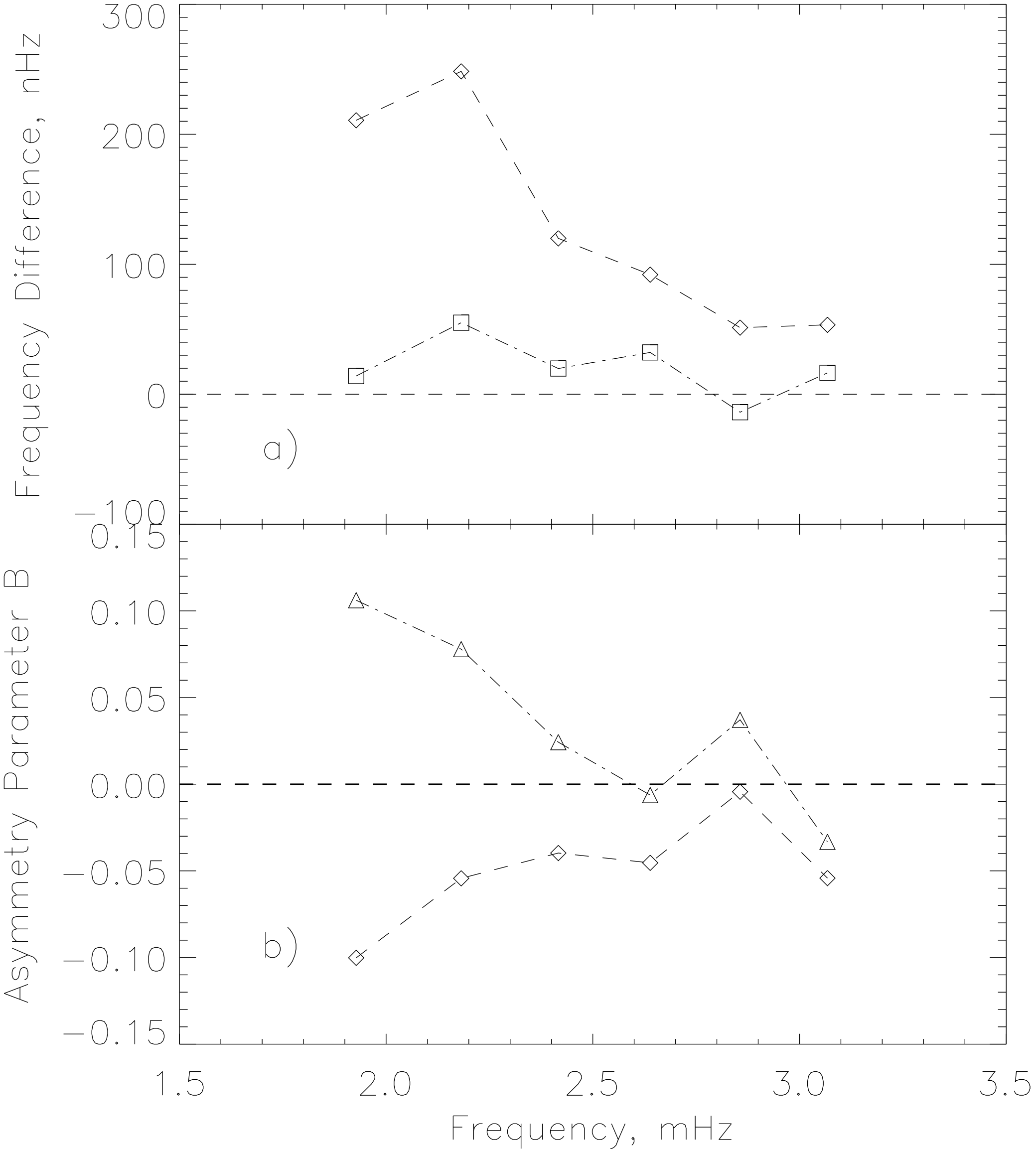

Figure 4.4: (a) Squares denote the difference (in nHz) between the asymmetrical fitted frequencies of intensity with velocity, while the diamonds are the deviation of the corresponding Lorentzian fitted frequencies of the MDI power spectra for $l = 75$. (b) Triangles represent the dimensionless asymmetry parameter B for the intensity power spectrum and the diamonds for the velocity power spectrum.

SHTs, they are Fourier transformed to make power spectra, shifted in frequency according to a solar rotation law, and averaged over the angular order $m$. To simplify the comparison we choose the 60 days from April 14 to June 12, 1997 for which simultaneous velocity and intensity images were available.

A fit of these power spectra for angular degree $l = 75$ and order $n$ from 3 to 8 is done using the asymmetrical formula. The technique is similar to that described in the previous section. Here we do not present the fits for $l = 200$ because the peaks are not properly resolved and the fits get corrupted by the $l$-leakage. In Figure 4.3 we see that the asymmetric formula fits the data reasonably well with a maximum deviation of 10%. From the fits we get a small difference in the frequency between velocity and intensity, which is much smaller than that obtained by fitting a Lorentzian as seen in Figure 4.4a. In Figure 4.4b the asymmetry parameter $B$ for both velocity and intensity is shown. This parameter, which controls the asymmetry, is found to decrease with frequency and reaches a minimum around 3 mHz. This is consistent with the low $l$ fits of Toutain et al. (1998) using the same asymmetrical formula.

## 4.4 Application of the formula to low degree modes

An accurate determination of frequencies of solar acoustic (p) modes of low angular degree $l$ is necessary to infer the structure and rotation of the solar core. Since the work of Duvall et al. (1993) based on oscillation spectra averaged over the azimuthal order, $m$, the line shape of medium-$l$ p modes have been considered to be possibly asymmetric. Moreover, this asymmetry showed up with opposite sign for modes observed in intensity and in velocity. In standard techniques of measuring solar frequencies (Anderson et al., 1990) the asymmetry is not taken into account, and the line shape is assumed to be a Lorentzian. This leads to systematic errors in frequency measurements, and thus to errors in helioseismic inferences of the structure of the Sun. Recently, Toutain et al. (1997) have observed frequency differences of the order of 0.1 $\mu$Hz between intensity and velocity low-degree p mode lines when a Lorentzian fit was done. In this chapter we show that these frequency differences can significantly be reduced using our model of an asymmetrical line profile.

The first successful attempt to detect the asymmetry of low-$l$ modes was made by Toutain (1993) using the intensity data from the IPHIR space experiment (Frohlich et al., 1990). However, the IPHIR data being the longest intensity time series available at that time, had a poor resolution and signal-to-noise ratio to make reliable conclusions about the asymmetry and corresponding frequency corrections.

The oscillations of the Sun have been observed continuously for about 2 years with three experiments on board SOHO. Two of these experiments are VIRGO (Frohlich et al., 1995) which is measuring oscillations of the solar irradiance with a triple Sun-photometer (SPM) and a 16-pixel imager LOI, (Appourchaux et al., 1995a) and the MDI which is measuring with a CCD detector velocity oscillations in the Ni 6768 line (Scherrer et al., 1995). We have used the longest available time series from both experiments consisting of 610 days of integrated velocity and spectral irradiance (at 400, 500 and 862 nm) to accurately measure the parameters of the p modes for degrees $l$=0,1 and 2 in a frequency domain ranging from 2000 to 4000 $\mu$Hz.

We discuss the fact that the shape of low-degree p mode lines significantly depart from a Lorentzian profile. We use a theoretical model by Nigam and Kosovichev (1998) to fit the asymmetrical shape found in the data. We fit both intensity and velocity lines to determine the frequency dependence of the asymmetry and present new estimates of eigenfrequencies of low-degree modes (Toutain et al., 1998) which are particularly important for determining the structure of the Sun's energy-generating core.

### 4.4.1 Integrated velocity and intensity power spectra

The power spectra of the 610-day time series are plotted in Figure 4.5 in a frequency range spanning from 1000 to 5000 $\mu$Hz. Below 2000 $\mu$Hz we hardly see p mode lines in the intensity data because of granulation noise which steeply increases, and above 4000 $\mu$Hz, mode linewidths are such that modes of degrees 0 and 2 overlap. We therefore restrict ourselves to work in this frequency range to compare the results from the velocity and intensity data. Because of the stochastic nature of solar oscillations, the power in each frequency bin of a line is distributed with a large variance around its

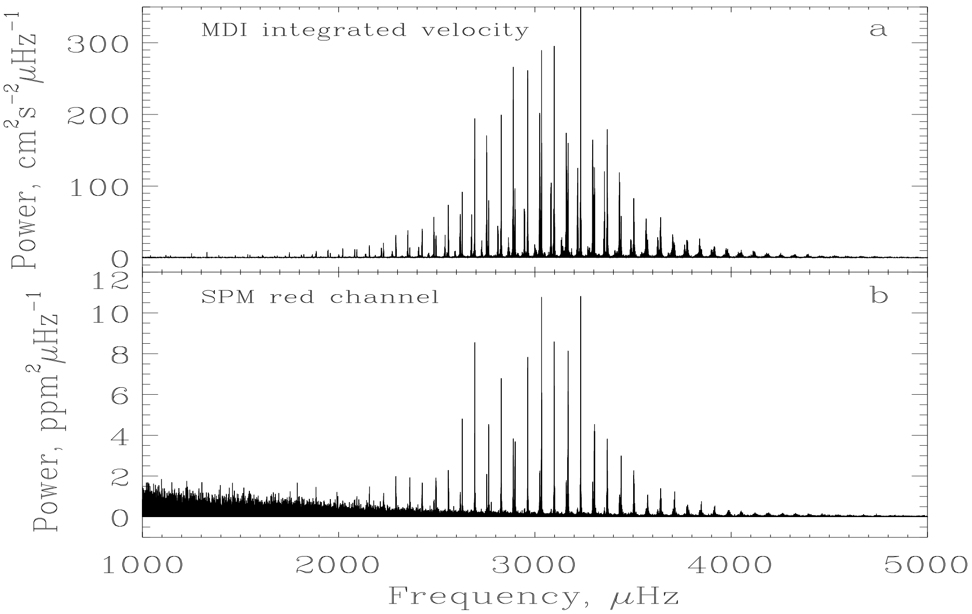

Figure 4.5: Oscillation power spectra of low angular degree solar p modes obtained from 610-day time series of a) MDI integrated velocity, and b) VIRGO/SPM intensity (red channel) measurements.

expectation value (Woodard, 1984). A smoothing of the line is therefore necessary to reveal its fine structure. Line asymmetry is mainly visible on the edges of the power spectra. As an example, we have plotted in Figure 4.6 the $l$=0, $n$=12 line both for MDI and SPM (red) spectra. The lines are smoothed with a 1 $\mu$Hz box-car average in order to enhance the asymmetry of the profiles. On top of the profiles are plotted results of fitting using a model of the asymmetrical line shape as described in the next section. The line asymmetry which is reversed between velocity and intensity power spectra is apparent.

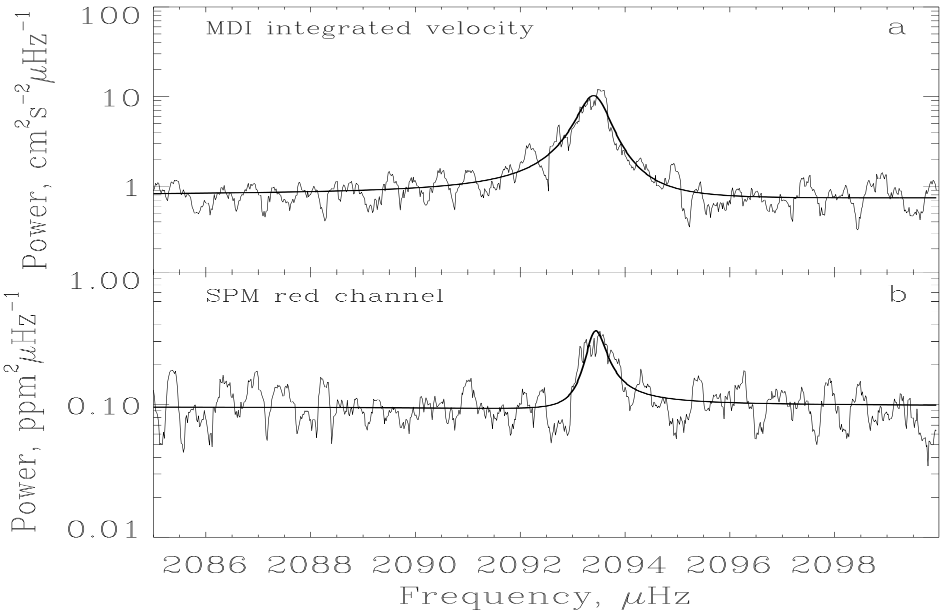

Figure 4.6: Smoothed $l$=0 $n$=12 line for MDI (a) and SPM (b) with a box-car average of 1 $\mu$Hz.

### 4.4.2 Physical model for p mode line asymmetry and fitting formula

Physically, asymmetry is a result of an interaction between an outward-directed wave from the source and a corresponding inward-directed wave that passes through the region of wave propagation (Duvall et al., 1993). As illustrated in Figure 4.6, the velocity power spectrum exhibits negative asymmetry (more power on the lower frequency end of the peak) whereas the intensity power spectrum shows positive asymmetry (more power on the higher frequency end of the peak). This reversal of asymmetry can be explained if correlated noise is added to the amplitude spectra (Nigam et al., 1998).

The asymmetry in velocity and intensity power spectra is of opposite sense because a component of the solar noise that is correlated with the source is present in the observed signal. The correlated component of the noise is below a certain threshold to preserve the asymmetry obtained by the model (Nigam et al., 1998) in the velocity power spectrum but that it is large enough (the correlated component is above a certain threshold) to reverse the asymmetry in the intensity spectrum. This is due to the fact that the correlated noise shifts the zero points in the amplitude spectra of the pressure perturbation. The uncorrelated noise plays no role in the reversal of asymmetry because it adds to the power not to the amplitude spectrum.

The solar intensity and velocity oscillations are observed from variations in an absorption (Fraunhofer) line or, as in the case of the SPM, from intensity variations in relatively broad bands of the solar spectrum. These variations consist of two parts: solar oscillation modes and granulation noise. Because the oscillation modes are excited by granulation the granulation signal (noise) is partially correlated with the oscillations. According to Goode et al. (1998) the solar oscillations are excited in the intergranular dark lanes. Thus, the observed intensity variations have a noise component which is caused directly by the dark lanes and correlated to the amplitude of the oscillations. It has been suggested by Roxburgh and Vorontsov (1997) that the granulation overshoot forms the correlated component of the noise to the velocity signal. However, the observations show higher level of noise in the intensity data, and support the idea by Nigam et al. (1998) that the line asymmetry in the intensity power spectra is reversed due to the correlated noise in the intensity observations.

To measure the properties of solar oscillations we employed an asymmetric fitting formula of Nigam and Kosovichev (1998) for the power, $P$ from equation (4.4):

### 4.4.3 Line asymmetry

According to the line shape model described in the previous section we have fitted $l$=0-2 doublets and the $l$=1 lines between 2000 and 4000 $\mu$Hz. The technique of fitting is a standard maximum likelihood technique. Usually for a disk-averaged spectrum we fit simultaneously the line for $l$=0 and 2 because they overlap. We therefore give a mean asymmetry for these degrees. The modes of $l$=1 are fitted assuming 2-component rotationally split multiplets of $m$=1 and -1, both components having the same asymmetry coefficient. The asymmetry coefficient is plotted in Figure 4.7

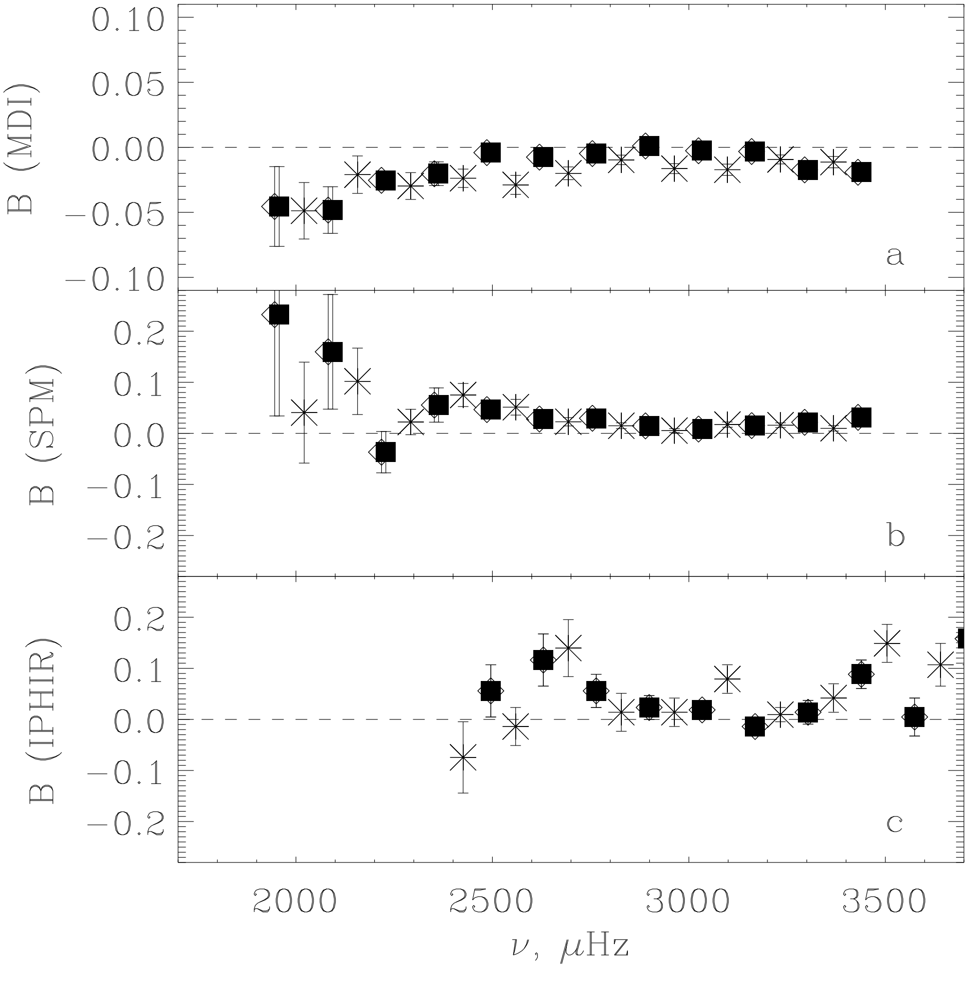

Figure 4.7: Asymmetry coefficient $B$ for $l = 0$ (squares), $l = 1$ (crosses) and $l = 2$ (diamonds) modes as a function of mode frequency for a) MDI, b) SPM data, and c) IPHIR data.

as a function of frequency for the MDI (a) and SPM (b) data. It is clear from these results that, according to the definition of asymmetry we have, velocity lines exhibit negative asymmetry whereas intensity lines exhibit positive asymmetry. Moreover the frequency dependence of the asymmetry is similar in both cases. Asymmetry seems to have a minimum around 3000 $\mu$Hz and appears to be smaller for the velocity than for the intensity at least for low and high frequencies. Both effects can easily be explained if correlation with noise along with the source exciting the modes is the factor of asymmetry (Nigam et al., 1998). In this case for a given correlation the asymmetry is a function of the square root of the inverse of the signal-to-noise ratio, which is largest around 3000 $\mu$Hz and is bigger in general for the velocity spectra compared to the intensity spectra, we expect the above behavior of the asymmetry with frequency and data type. These arguments also explain why lines in the red spectrum have slightly larger asymmetries compared to those from the SPM green channel spectrum. This is because the signal-to-noise ratio in the red is about 10% lower than in the green. On the other hand, blue and green signals are very well correlated and have the same signal-to-noise ratios leading to the same asymmetry.

It is interesting to compare these asymmetries with those obtained with IPHIR (Frohlich et al., 1990), which is an instrument similar to the SPM/VIRGO instrument. IPHIR lines were fitted with an empirical line shape formula (Toutain, 1993) which has the property to describe well the asymmetrical profile shown by Duvall et al. (1993). Compared to SPM, IPHIR data have a signal-to-noise ratio in power which is 3 times smaller. If the noise were to be solar noise and according to our model of noise-source correlation we would expect the asymmetries with IPHIR to be 2 times larger than with SPM, and that is what they are. It is interesting to note that an increase in solar noise for a fixed line amplitude should mask the line asymmetry, but it turns out to be opposite with IPHIR. The asymmetries from the IPHIR data are generally larger than the SPM asymmetries. It is therefore consistent to think that IPHIR noise in the 5-minute range is solar noise and that the p mode amplitudes are correlated with the noise.

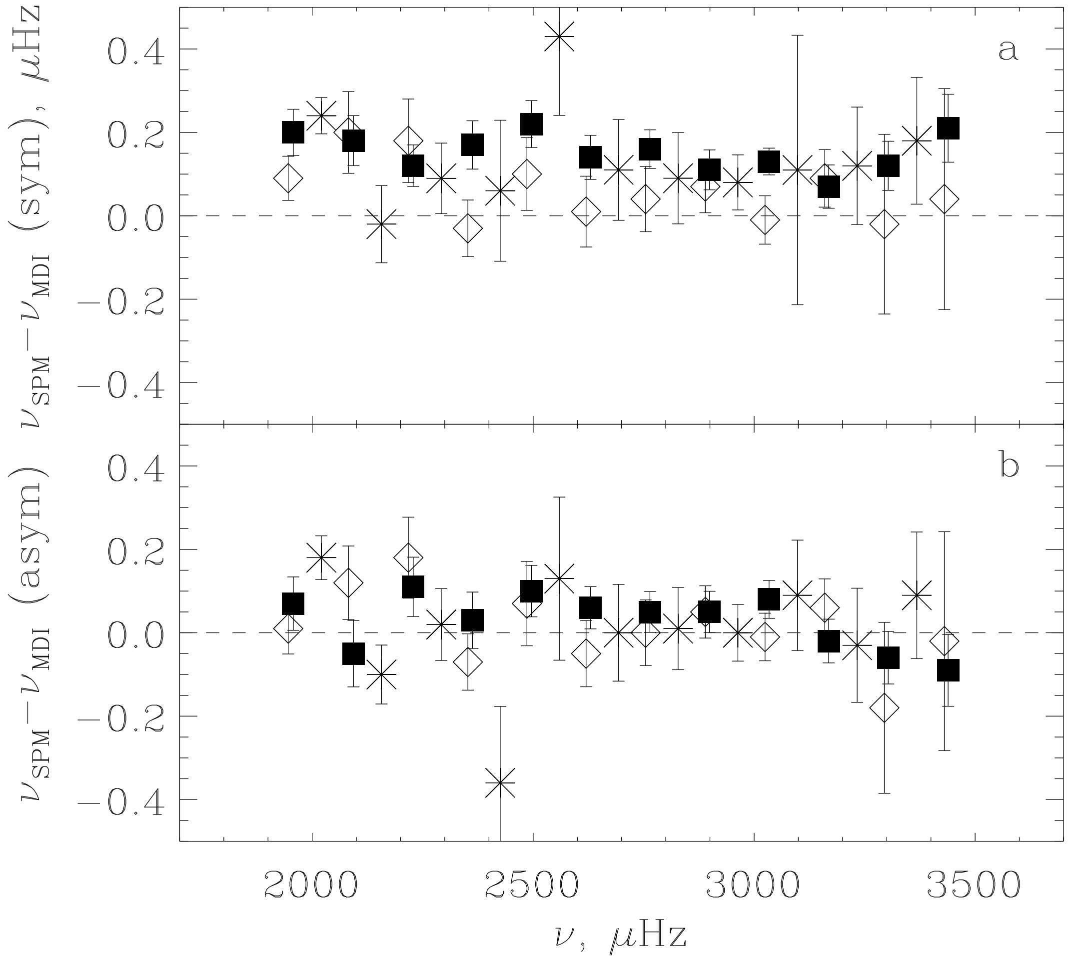

Figure 4.8: Frequency differences between SPM and MDI frequencies for $l = 0$ (squares), $l = 1$ (crosses) and $l = 2$ (diamonds) modes estimated using a) a symmetrical Lorentzian profile, and b) the asymmetrical line profile (Eq. 4.4). The errorbars are the 1-$\sigma$ errors.

### 4.4.4 Frequency differences

The frequency differences from our symmetrical (Lorentzian) fits to the MDI and SPM red channel data are plotted in Figure 4.8a. There is a systematic shift both for $l$=0-2 and $l$=1 frequencies. The frequencies inferred from the SPM intensity spectrum are systematically higher than the frequencies from the MDI velocity spectrum, as one would expect due to the reversal of line asymmetry. These differences are of the order of 0.1 $\mu$Hz.

Using the asymmetrical formula given in equation (4.4) we have recomputed the mode frequencies. The results are plotted in Figure 4.8b. Obviously, the differences are significantly reduced when an asymmetrical profile is used. We have tested the statistical significance of the asymmetry using the likelihood ratio-test (Appourchaux et al., 1995a) and find that it is highly significant in most cases. Table 1 in Toutain et al. (1998) shows mean frequency differences between intensity and velocity data obtained with both symmetrical and asymmetrical fits. The close agreement between frequencies from the asymmetrical fits means that these frequencies provide more accurate approximation to the solar mode eigenfrequencies than the frequencies previously measured with a symmetrical Lorentzian profile. In Table 2 of Toutain et al. (1998), a list of the frequencies obtained from the asymmetrical fits to the MDI velocity spectra in the range from 1000 to 4000 $\mu$Hz are provided.

### 4.4.5 Implications for solar core structure

To determine the hydrostatic structure of the Sun we combined the frequencies of the low-degree modes with the frequencies of $l = 3 - 300$ obtained by Rhodes et al. (1997) from the MDI medium-$l$ data. The medium-$l$ frequencies which constrain the structure outside the solar core have not been corrected for the asymmetry effect. The spherically symmetric structure of the Sun was determined by using a version of the optimally localized averaging inversion method of Gough and Kosovichev (1988). Figure 4.9 shows the relative difference between the square of the sound speed in the Sun and the standard solar model (Christensen-Dalsgaard et al., 1996) In the central core, the sound speed determined using the frequencies from the asymmetrical fits

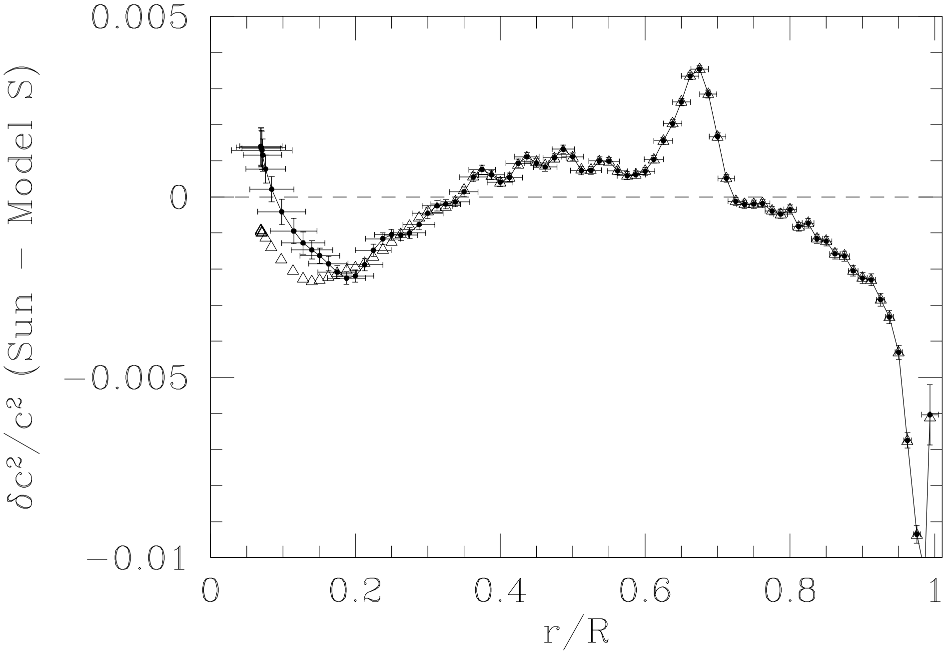

Figure 4.9: The differences in the squared sound speed between the Sun and the solar model S inferred from the frequencies of $l = 0-2$ modes and the medium-$l$ frequencies of Rhodes et al. (1997). The solid curve with the crosses shows the results obtained with the asymmetrically fitted low-degree modes; the triangles represent the result of the symmetrical (Lorentzian) fits to the mode lines of the oscillation power spectrum. The vertical error bars show the formal error estimates, and the horizontal bars show the characteristic width of the localized averages.

(solid curve with errorbars) is approximately 0.1-0.2% higher than that inferred from the symmetrical frequency fits. This shift does not result in any dramatic changes in our knowledge of the solar core structure. However, it may be important for understanding the difference between the Sun and the standard model.

It has been noted that the sound-speed perturbation profile in the central core is consistent with partial mixing (Gough and Kosovichev, 1988). The change of slope at 0.2 R may indicate the boundary of mixing. Of course, at this stage, other possible explanations, e.g. variations of opacity and nuclear reaction rates, are not ruled out. Also, we note that our inversion results are not fully consistent with the recent results from GOLF (Turck-Chièze et al., 1997), in which, however, the asymmetry effect was not taken into account.

## 4.5 Summary

We have investigated the shape of spectral lines of solar oscillation modes using both theoretical models and observational data from SOHO/MDI. A new fitting formula for the power spectra of solar velocity and intensity oscillations has been derived. It has been shown that the formula provides an accurate estimate of the eigenfrequencies when applied to simulated and MDI velocity and intensity power spectra.

We have studied p mode frequency differences between velocity and intensity data using 610 days of MDI integrated velocity and VIRGO/SPM intensity. Fitting $l$=0-2 p mode lines with commonly used Lorentzian profiles leads to systematic frequency differences of the order of 0.1 $\mu$Hz between intensity and velocity and also to a smaller extent between different wavelengths in intensity. Using instead a model of an asymmetrical line profile based on excitation of solar oscillations by a localized source and its correlation with the solar noise in the observed velocity and intensity signals gives frequency differences which are significantly smaller than the differences resulting from Lorentzian fits. The asymmetrical line profile provides more accurate estimates of the eigenfrequencies of solar oscillations. The asymmetry effect results in small (0.1-0.2%) but significant changes in the inferred sound-speed inversion in the energy-generating core, which may be important for understanding the physical processes in the core.

# Chapter 5

# Source of Solar Acoustic Modes

`(Part of this chapter is published in ApJ 1999, 514, L53)`

Solar oscillations are thought to be excited stochastically by turbulent convection. It was Lighthill (1952) who for the first time laid down a mathematical theory of excitation of sound waves by sources of different multipoles. Since then, several authors (Goldreich and Kumar, 1990); (Balmforth, 1992) have applied his theory to the excitation of solar p modes. Recently, Goldreich et al. (1994) and Stein and Nordlund (1998) argue that entropy fluctuations, which correspond to a monopole source, drive the solar p modes.

Only recently has it been realized that the observed difference in asymmetry between velocity and intensity power spectra of the solar acoustic modes is a consequence of the excitation mechanism of the solar oscillations. The relation of the observed asymmetry and the excitation mechanism (Roxburgh and Vorontsov, 1997); (Nigam et al., 1998); (Nigam and Kosovichev, 1999b); (Rast, 1999) and (Kumar and Basu, 1999) throws light on the nature of the correlated noise that is responsible for the opposite asymmetry between velocity and intensity. The correlation is expected because the main source of noise is the turbulent convection which also drives the oscillations. The same correlated noise also explains the unusual phase difference between velocity and intensity oscillations (Nigam and Kosovichev, 1999a) and the high-frequency shift above the acoustic cutoff frequency between velocity and intensity (Nigam et al., 1998).

In this chapter we investigate the power spectra of velocity and pressure perturbations obtained for different source depths and types. In order to explain the reversal of asymmetry between velocity and intensity, correlated noise is added to the amplitude spectrum of the pressure perturbation following Nigam et al. (1998). Previously Kumar and Lu (1991) proposed that the source depth can be determined solely by matching the high frequency spectra (above the acoustic cutoff frequency) with the observed spectra. Clearly this is not the case and has been pointed out in Abrams and Kumar (1996), Nigam et al. (1998) and Kumar and Basu (1999). In this paper the source depth and type are determined by studying both the low and high frequency part of the spectra. The interaction of the correlated noise and the p modes support the observations of Goode et al. (1998), that the solar oscillations are excited in the intergranular dark lanes.

In §2 we compute the power spectra for different source depths and for different multipoles using a standard solar model (Christensen-Dalsgaard et al., 1996). In §3 we discuss the origin and role of the correlated noise and propose a mechanism for the excitation of solar oscillations that is consistent with the MDI observations.

## 5.1 Theoretical Model

We assume that solar acoustic waves are generated by turbulence in the convection zone, and apply Lighthill's (1952) method to calculate the velocity and pressure perturbations. We also assume that the intensity variations recorded by the MDI instrument correspond to the pressure perturbations together with the correlated noise.

From equation (2.1)

$$\frac{d^2\Psi}{dr^2} + \left[\frac{\omega^2 - \omega_{\mathrm{c}}^2}{c^2} - \frac{L^2}{r^2}\left(1 - \frac{N^2}{\omega^2}\right)\right]\Psi = S[\boldsymbol{f}, q], \tag{5.1}$$

where $\Psi$ is proportional to the Lagrangian pressure perturbation $\delta p$, $r$ is radius, $\omega$ is frequency, $\omega_{\mathrm{c}}$ is the acoustic cutoff frequency, $c$ is the equilibrium sound speed, $N$ is the buoyancy frequency, $L = \sqrt{l(l+1)}$, $S$ is a combination of the source terms given by equation (2.2), that include the turbulent fluctuating Reynolds stress force, $\boldsymbol{f} = \partial(\rho \boldsymbol{u}' u_j')/\partial x_j$ and the mass source, $q = \nabla \cdot (\rho' \boldsymbol{u}')$ where $\rho$ is the equilibrium density, and $p'$, $\rho'$ and $\boldsymbol{u}'$ are fluctuating parts of pressure, density and velocity respectively.

In order to understand the properties of the solution it is important to note that the source is proportional to $\boldsymbol{f}$ and $\nabla \cdot \boldsymbol{f} \equiv \partial^2(\rho u_i' u_j')/\partial x_i \partial x_j$. This means that a localized force gives rise to acoustic radiation of dipole type, Reynolds stresses $\rho u_i' u_j'$ generate quadrupole type of radiation, and mass sources $q$ are of monopole type. The exact contributions of the sources to different multipoles depends on the model of turbulence.

The Green's function, $G_\Psi(r, r_\mathrm{s})$ for equation (5.1) is calculated numerically as was done in section 2.2.1. Then, integrating by parts, we express the pressure and velocity perturbations of the acoustic waves in terms of the Green's function for the localized sources of different types (see Appendix D). For instance, for a point source force $\boldsymbol{f}$, the pressure perturbation, $\delta p(r_\mathrm{obs})$, at an observing location, $r = r_\mathrm{obs}$, is proportional to $G_\Psi(r, r_\mathrm{s})$ and the derivative of $G_\Psi(r, r_\mathrm{s})$ with respect to the source location $r_\mathrm{s}$ since $S$ is proportional to $\boldsymbol{f}$ and $\nabla \boldsymbol{f}$. On the other hand, the pressure perturbation is proportional to $G_\Psi(r, r_\mathrm{s})$ for both the composite source $S$ and the monopole source. Where as for a quadrupole source, it is proportional to the first and second derivatives of the Green's function with respect to the source location. The pressure and velocity perturbations for sources extended over a range of depth can then be calculated from the respective Green's function by linear superposition.

The pressure perturbations for monopole, dipole and quadrupole sources are given below (see Appendix D):

$$\delta p_\mathrm{mon}(r_\mathrm{obs}) \propto c_5(r_\mathrm{s}) G_\Psi(r_\mathrm{obs}, r_\mathrm{s}), \tag{5.2}$$

$$\delta p_\mathrm{dip}(r_\mathrm{obs}) \propto c_6(r_\mathrm{s}) G_\Psi - \frac{d}{dr_\mathrm{s}} \left( \frac{G_\Psi}{c_7(r_\mathrm{s})} \right), \tag{5.3}$$

$$\delta p_\mathrm{qud}(r_\mathrm{obs}) \propto \frac{d^2}{dr_\mathrm{s}^2} \left( \frac{G_\Psi}{c_7(r_\mathrm{s})} \right) - \frac{d}{dr_\mathrm{s}} \left( \frac{G_\Psi}{c_8(r_\mathrm{s})} \right) \tag{5.4}$$

where $c_5, c_6, c_7$ and $c_8$ are calculated from the solar model. The velocity perturbations can be calculated similarly (see Appendix D, equation (D.25)).

Using a standard solar model (Christensen-Dalsgaard et al., 1996), we have calculated the theoretical Green's functions of angular degree $l = 200$ for both the velocity and pressure perturbations for different types of acoustic sources located at various depths, $d$, beneath the photospheric level of the model. Figures 5.1 and 5.2 show the results at $r_{\rm obs} = 300$ km above the photosphere, where the observed spectral line is formed, for a monopole source and a dipole source due to the Reynolds stress force respectively at four depths, 50 km, 75 km, 100 km, and 200 km.

For the velocity (or pressure) power spectra (Fig. 5.1) corresponding to the monopole source, the bound state modes below the acoustic cutoff frequency ($\approx 5.2$ mHz) show marked asymmetry which decreases with increasing frequency. The peaks of the bound states are close to the eigenfrequencies if damping is small as is the case for p modes. The scattered states (those above the acoustic cutoff frequency) are almost symmetrical and their peaks are mainly determined by the source position. They convey little information about the solar cavity as compared to the bound states. For the spectra for depths, $d$=50 km, 75 km and 100 km, the sense of asymmetry of the bound states and the peaks of the scattered states are in agreement with the MDI observations. However, for larger depths, there is a clear mismatch with the MDI data of Fig. 2.1a, because the scattered states show asymmetry not found in the observation. For example, at a depth of 200 km there is a peak around 5.3 mHz that has become asymmetrical, and moreover at this depth the peaks of the scattered states do not match the observed maxima. The quadrupole source produces a power spectra similar to that in Figure 5.1 that is produced by a monopole source.

It is interesting to note that the velocity (or pressure) power spectra (Fig. 5.2) for a dipole source are more sensitive to the depth of the source. Since the asymmetry in Figure 5.2 does not match the observations, the dipole source is ruled out. Also, changing the type of the source (e.g. dipole to quadrupole) changes the sense of the asymmetry in the power spectra.

It is important to note that the narrow range of the acoustic source depth found by comparing the theoretical and observed power spectra coincides with the region

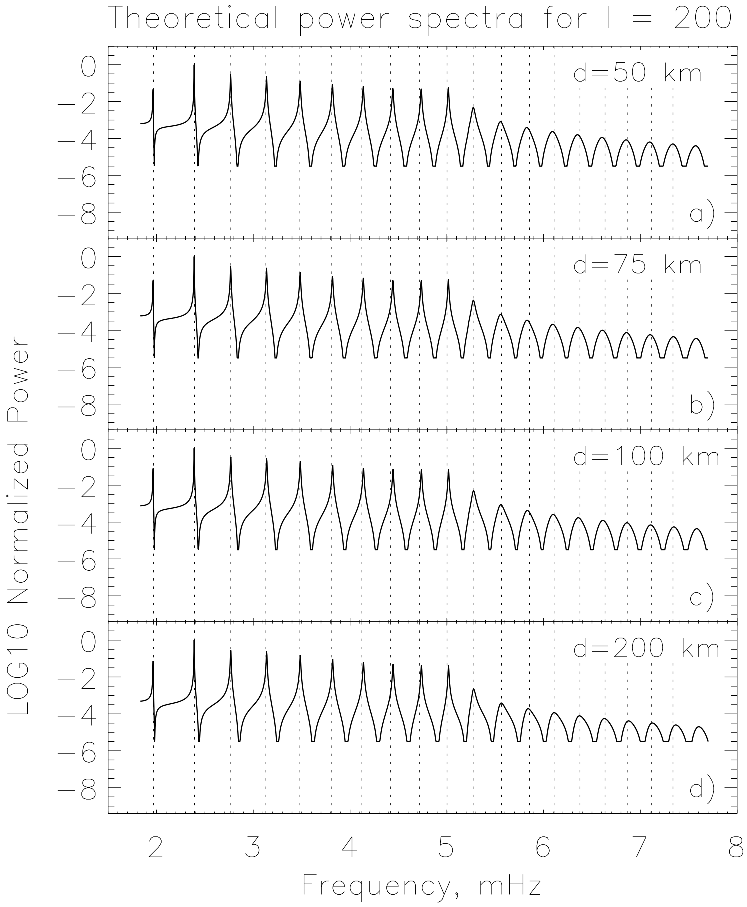

Figure 5.1: Normalized (with respect to its maximum) theoretical velocity power spectra of solar oscillations of angular degree $l = 200$ produced by a monopole source located at four depths beneath the photospheric level at $d = 50$ km, 75 km, 100 km and 200 km. Vertical dotted lines show the location of the maxima in the observed MDI velocity power spectrum (Fig. 2.1a) We have applied a threshold (at $10^{-6}$) to remove the numerical noise. The pressure spectra look similar.

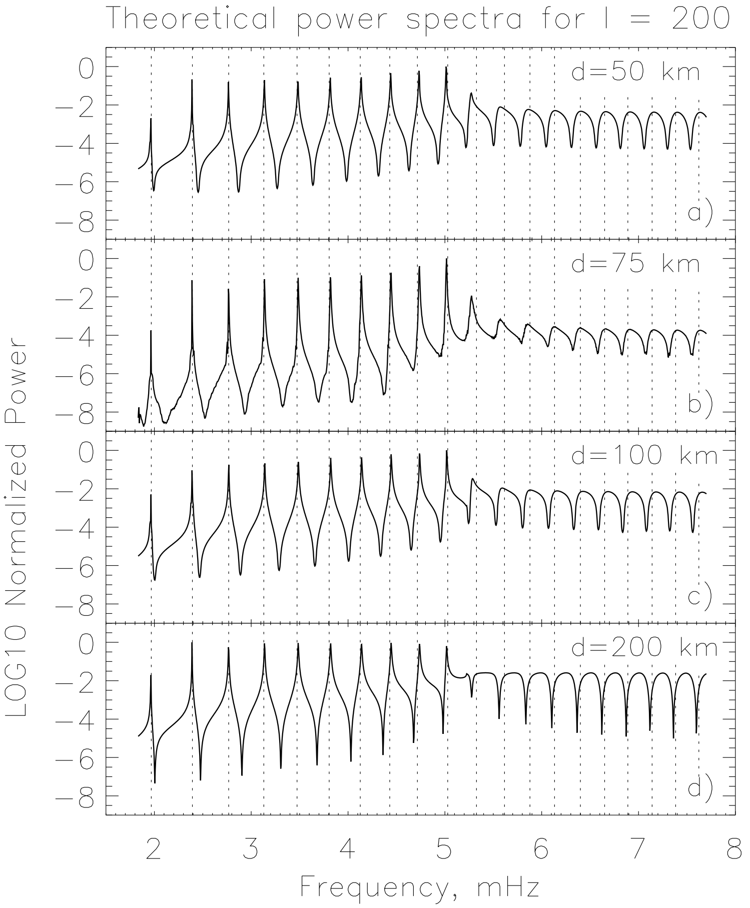

Figure 5.2: Normalized (with respect to its maximum) theoretical pressure power spectra of solar oscillations of angular degree $l = 200$ produced by a dipole source (point force) located at four depths beneath the photospheric level at $d = 50$ km, 75 km, 100 km and 200 km. Vertical dotted lines show the locations of the maxima in the observed intensity power spectrum (Fig. 2.1b). The velocity spectra look similar.

of superadiabatic convection in the solar model. This region represents the highly unstable upper boundary layer of the convection zone where convective motions are most violent. Figure 5.3 shows the properties of the upper convection zone as described in the standard solar model based on a mixing length theory of convection. In the superadiabatic layer, Reynolds stresses show a sharp gradient around 75 km below the photosphere. Also from Kumar (1994), the quadrupole source due to the Reynolds stresses peaks in the superadiabatic layer. It is therefore probable that the p modes get excited in this region.

It is remarkable that the sharp variation of the equilibrium solar model in the superadiabatic layer effects the pressure and velocity perturbations of the low-frequency modes in such a way that the asymmetry of these modes corresponds to the observations only when the acoustic source is placed within the layer, thus pinning down the location and the nature of the source. Of course, in the real Sun the superadiabatic layer is likely to be extended over a larger region, which may also vary from the pole to the equator.

In the above formulation we found that a monopole source reproduced the velocity power spectrum rather well. The quadrupole source due the turbulent fluctuating Reynolds stresses behaves more like the monopole source as seen in Figure 5.1 and it matches the velocity observations. On the other hand, the force due to the Reynolds stress is a source of dipole type and it does not match the observations as well as the monopole and quadrupole sources match the observed velocity power spectrum. Moreover, past models of mode excitation were unable to explain the reversal of asymmetry between velocity and intensity. Recently, Nigam et al. (1998) have proposed that the correlated noise, which is due to the turbulent convection (granulation), is responsible for the reversal of asymmetry between velocity and intensity. The role of the correlated noise on mode excitation is discussed in the next section.

## 5.2 The Role of Correlated Noise

The role of the correlated noise is two-fold. Firstly, by incorporating it into the model we are able to explain the observed reversal of asymmetry, high frequency

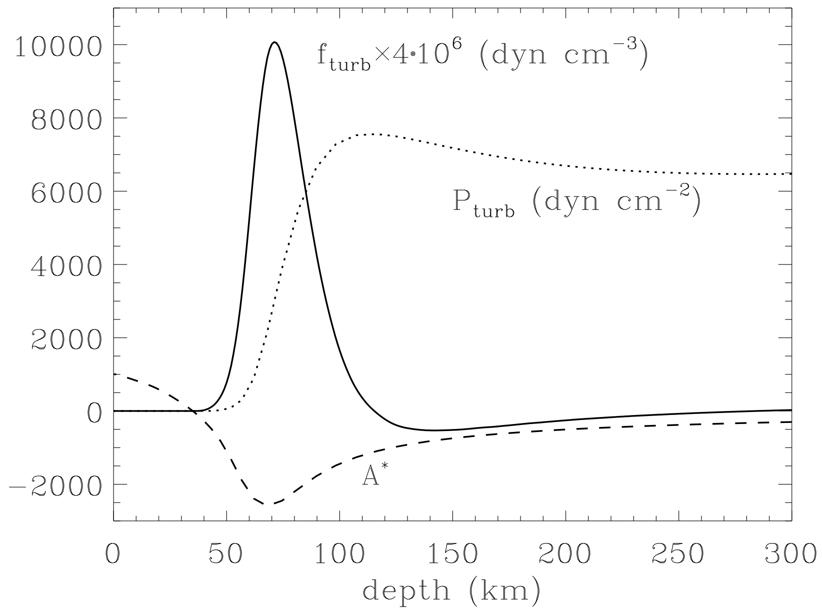

Figure 5.3: Turbulent force (solid curve) and pressure (dotted curve) due to Reynolds stresses as a function of depth in a standard solar model based on a mixing length theory. Dashed curve shows parameter of convective stability $A^* \equiv \frac{1}{\gamma}\frac{\log p}{\log r} - \frac{\log \rho}{\log r}$.

shift above the acoustic cutoff frequency and the unusual phase difference between intensity and velocity (Nigam and Kosovichev, 1999a). Secondly, it sheds some light into the excitation mechanism for p modes. It was discussed in chapter 2, section 2.2.2 that the pressure and velocity perturbations can be calculated from the Green's function after the addition of correlated noise, in order to match the observed power spectra.

From Figure 5.1 it is found that both monopole and quadrupole sources match the asymmetry and high frequency peaks of the observed velocity power spectrum, when the source is placed at a depth of 75 km. However, the dipole source does not match the velocity power spectrum, hence it can be ruled out. In order to match the observed intensity power spectrum correlated noise is added to the pressure perturbation for a source located at 75 km. Pressure perturbation with correlated noise for a source depth of 75 km is shown in Figure 5.4 for monopole, dipole and quadrupole sources.

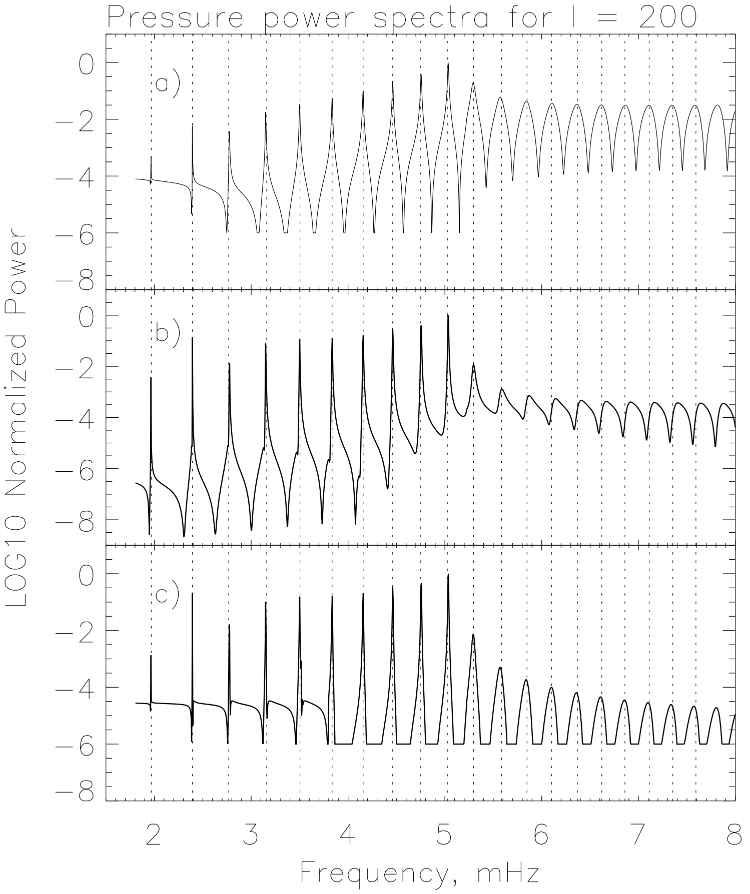

Figure 5.4: Normalized (with respect to its maximum) theoretical pressure power spectra of solar oscillations of angular degree $l = 200$ produced by a source located at a depth of 75 km beneath the photospheric level. Three different types of sources are considered, to which real correlated noise is added. a) Monopole, relative level of correlated noise $= -0.02$, (b) Dipole, relative level $= -4.0\times10^{-5}$ and (c) Quadrupole, relative level $= -0.03$. These values have been normalized by the maximum value of the real part of the pressure perturbation. There is no uncorrelated noise in the above cases. We have applied a threshold (at $10^{-6}$) to remove the numerical noise.

For different types of sources the level of the correlated noise was adjusted to get the best possible agreement with the data. The sources happen to be negatively correlated as also shown by Nigam and Kosovichev (1999a). This is consistent to the photospheric darkening in the intensity fluctuations prior to the acoustic event as observed by Goode et al. (1998) and seen in the simulations of Stein and Nordlund (1998). By adding correlated noise we are able to match the intensity data best with the help of a monopole source, as compared to the other source types. We are also able to reverse the asymmetry for the dipole and quadrupole sources too, but they do not match the asymmetry and high frequency peaks in the observed intensity power spectrum as well as the monopole source.

The source of the oscillations were located by Goode et al. (1992) close to where we find in the present paper. They used models and data about the height variation of the velocity signal in the photosphere to pin down the depth of the source. Also, Goode et al. (1998) showed a linear dependence on the local convective velocity of the magnitude of the local excitation of oscillations implying a monopole source, which is consistent with our finding.

## 5.3 Summary

Simulating the MDI observations of medium angular degree we find that a source is located at a depth of 75 ± 50 km below the photosphere, in the superadiabatic layer. The source appears to be of composite form, consisting of monopole and quadrupole types. A monopole source provides a best match with the observations in comparison to the quadrupole source; hence, it may be the dominant term exciting the p modes. Studying the interaction of the correlated noise with the p modes one finds that the noise is negatively correlated to the source, which leads to photospheric darkening prior to the acoustic emission. Therefore, it is possible that the solar p modes are excited by a combination of mass or entropy fluctuations due to radiative cooling at the solar surface, which constitute a monopole source and quadrupolar Reynolds stresses. Studying the phase relation between the correlated noise and the perturbations could provide an insight into the physics of excitation of solar p modes.

# Chapter 6

# Conclusions

In this thesis I have discussed the excitation of solar p modes. The main contributions to the field are an explanation for the reversal in asymmetry between velocity and intensity power spectra. This then led to the derivation of an asymmetrical fitting formula to determine the eigenfrequencies of oscillation by fitting both the velocity and intensity power spectra. I also gave an explanation for the observed phase difference between velocity and intensity helioseismic spectra. To explain these observed characteristics a model of excitation for solar p modes is proposed.

The cause of the reversal of asymmetry and the observed phase difference is due to the presence of correlated noise in the oscillation spectra. This noise happens to be higher in the intensity observations and can perhaps be attributed to the granulation (Nigam et al., 1998). Solar p modes are believed to be excited by turbulent convection in the superadiabatic layer, by a combination of mass or entropy fluctuations, which constitute a monopole source and quadrupolar Reynolds stresses (Nigam and Kosovichev, 1999b). The excitation of p modes could proceed in the following way: Radiative cooling at the solar surface results in monopolar emission of sound due to entropy fluctuations, followed by convective downdrafts in the dark narrow intergrannular lanes. Such mass fluctuations are linked to changes in volume, which in a gravitationally stratified medium such as the Sun produce dipolar emission via buoyant acceleration in the cool intergrannular lanes. Finally, the Reynolds stresses resulting from horizontal flow into the evacuated region left behind by the downflow are responsible for quadrupolar acoustic emission. In the observations of Goode et al. (1998) and simulations of Nordlund (1985), Stein and Nordlund (1989) the strength of the acoustic event is correlated to the photospheric darkening that is observed prior to the occurrence of the event. This supports the notion of the correlated noise that is introduced in the thesis. Several groups have verified our findings independently (Kumar and Basu, 1999); (Rast, 1999) . The phase difference between velocity and intensity that was studied in chapter 3 has been recently confirmed by Oliviero et al. (1999) and Straus et al. (1999), who attribute the unusual behavior of the phase to the correlated background. Moreover, the asymmetrical fitting formula is now being used by the helioseismology community to determine the eigenfrequencies of oscillation of the solar p and f modes (Antia and Basu, 1999); (Thiery et al., 1999); (Bertello et al., 1999).

## 6.1 Directions for Future Work

It would be interesting to verify the above results using numerical simulations of Stein and Nordlund. The reversal of asymmetry in the intensity power spectra could then be explained by solving the equations that include radiative transfer in the optically thin outer layers. Using the model proposed here and the observations from the different instruments (MDI, GOLF and VIRGO) onboard SOHO, it should be possible to estimate the correlated noise and study its physics. This would be very useful in understanding the interaction of oscillations with turbulence. Also changes in asymmetry and phase difference with solar cycle would be worth studying. This would be useful in studying the effect that the magnetic field has on the p mode frequencies. It would be challenging to fit the splittings and take rotation into account. Ridge fitting could be done using this formula. It would be interesting to see if the whole spectrum could be fit all at once. Since the correlated noise is much less in the velocity spectrum compared to the intensity, whether fitting the velocity power spectrum to determine the eigenfrequencies sufficient? These are a few important related problems to keep the helioseismologists occupied into the next century.

The effect of asymmetry on the frequencies of p modes will be important in correcting the solar models, in order to match the corrected observed frequencies. This would in turn have an impact on the celebrated solar neutrino problem (Bahcall and Davis, 1976).

High spatial and temporal resolution observations would be useful to resolve individual acoustic sources and study their distribution. This would be invaluable in studying the physics of excitation of solar p modes. A few years back Brown (1991) has proposed that these sources are likely to be localized and discrete. Therefore, a technique using wavelets (Milford and Nigam, 1995) could be applied to the data in order to study these acoustic events.

A similar study for the f mode could be undertaken. This would then shed light on its excitation.

The formalism developed in this thesis can be used to theoretically study the excitation characteristics of g modes. When, if ever, g modes are detected in the Sun, they can be used to test the predictions of the theory.

The millennium has seen several interesting discoveries. Solar p modes with a period of about five minutes (Leighton et al., 1962) were discovered only four decades ago, and the story of mode excitation has been revisited several times by many authors. There is a long way to go, but we hope to learn more about these acoustic modes and the Sun in the next century.

# Appendix A

# Mode Excitation

A derivation of the equations discussed in chapter 2 is carried out here. In §A.1 the basic equation in terms of the Lagrangian pressure perturbation is derived. In §A.2 the algorithm for the numerical computation of the Green's function is outlined. Finally, in §A.3 and §A.4 the Green's function and the eigenvalue condition for the simple potential well problem are calculated analytically.

## A.1 Linearized equations in terms of Lagrangian perturbations

The equations (1.22) and (1.23) are rewritten as

$$\frac{d\xi}{dr} + A_{11}\xi + A_{12}\delta p = S_1 \tag{A.1}$$

$$\frac{d\delta p}{dr} + A_{21}\xi + A_{22}\delta p = S_2 \tag{A.2}$$

where

$$A_{11} = \frac{2}{r} - \frac{L^2 g}{\omega^2 r^2} \tag{A.3}$$

$$A_{12} = \left(1 - \frac{L^2c^2}{\omega^2 r^2}\right)\frac{1}{\rho c^2} \tag{A.4}$$

$$A_{21} = -\frac{g\rho f}{r} \tag{A.5}$$

$$A_{22} = \frac{L^2 g}{\omega^2 r^2} \tag{A.6}$$

where $f$ is defined in equation (1.24)

The equations (A.1) and (A.2) are transformed to (see equations (1.30) and (1.31))

$$\frac{d^2\Psi}{dr^2} + K^2\Psi = S \tag{A.7}$$

where $\Psi$ is proportional to the Lagrangian pressure perturbation $\delta p$ and $K$ is is given by equations (1.32) or (1.37)

For p modes this equation is simplified as

$$K^2(r) \approx \frac{\omega_1^2 - \omega_+^2}{c^2} \tag{A.8}$$

where, $\omega_1^2 = \omega^2 + i\omega\Gamma$, and $\Gamma$ is the damping coefficient.

The composite source corresponding to the Lagrangian pressure perturbation is

$$S(r,\omega) = \left[c_1\frac{dS_2}{dr} + c_2 S_2\right] + \left[c_3\frac{dS_1}{dr} + c_4 S_1\right], \tag{A.9}$$

where $c_1, c_2, c_3$ and $c_4$ depend on the solar model and are given by:

$$c_1 = 1/u \tag{A.10}$$

where $u$ is defined by equation

$$c_2 = z/u \tag{A.11}$$

and $z$ is given by

$$z = A_{11} - \frac{A'_{21}}{A_{21}} = A_{11} - \frac{d(\ln A_{21})}{dr} \tag{A.12}$$

$$c_3 = -\frac{\rho g}{u} \tag{A.13}$$

$$c_4 = -\frac{\left[z\rho g + A_{21} + \frac{d(\rho g)}{dr}\right]}{u} \tag{A.14}$$

## A.2 Numerical solution to the Green's function

The defining equation for the Green's function is

$$\frac{d^2\Psi}{dr^2} + \frac{\omega_1^2 - \omega_+^2}{c^2}\Psi = \delta(r - r_\mathrm{s}), \tag{A.15}$$

where, $\omega_1^2 = \omega^2 + i\omega\Gamma$

The above equation is discretized using a non-uniform mesh, by finited difference approximation of the derivative. The following notation is used $\Psi_\mathrm{j} = \Psi(r_\mathrm{j})$, $c_\mathrm{j} = c(r_\mathrm{j})$ and for other variables. The radial variable $r$ has been discretized as $r_1, r_2, \ldots\, r_\mathrm{j}, \ldots\, r_\mathrm{N}$.

This is subject to the following boundary conditions: At $r = 0$

$$\Psi = 0 \tag{A.16}$$

At $r = R$, the radiation condition is applied to ensure outgoing waves. A harmonic time dependence of $e^{i\omega t}$ is used.

$$\frac{d\Psi}{dr} + ik_\mathrm{R}\Psi = 0 \tag{A.17}$$

where,

$$k^2(r) = \frac{\omega_1^2 - \omega_+^2(r)}{c^2(r)} \tag{A.18}$$

Evaluating equation (A.18) at $r = R$ leads to

$$k_{\mathrm{R}}^2 = k^2(R) = \frac{\omega_1^2 - \omega_{+\mathrm{R}}^2}{c_{\mathrm{R}}^2} \tag{A.19}$$

If on the other hand a harmonic time dependence of $e^{-i\omega t}$ is used instead, the radiation condition is modified to

$$\frac{d\Psi}{dr} - ik_{\mathrm{R}}\Psi = 0 \tag{A.20}$$

At the source location $r = r_{\mathrm{s}}$, the solution is continuous, but there is a jump in the first derivative. There are two solutions $\Psi^<$ for $0 < r < r_{\mathrm{s}}$ and $\Psi^>$ for $r_{\mathrm{s}} < r < R$. They are matched at $r = r_{\mathrm{s}}$.

The problem of computing the Green's function can be formulated as solving the following differential equations subject to the boundary and matching conditions.

$$\frac{d^2\Psi^<}{dr^2} + \frac{\omega_1^2 - \omega_+^2}{c^2}\Psi^< = 0 \tag{A.21}$$

$$\frac{d^2\Psi^>}{dr^2} + \frac{\omega_1^2 - \omega_+^2}{c^2}\Psi^> = 0 \tag{A.22}$$

$$\Psi^<(r) = 0, \qquad \text{at} \qquad r = 0 \tag{A.23}$$

$$\Psi^<(r_{\mathrm{s}}) = \Psi^>(r_{\mathrm{s}}) \tag{A.24}$$

$$\frac{d\Psi^>}{dr} - \frac{d\Psi^<}{dr} = 1, \qquad \text{at} \qquad r = r_{\mathrm{s}} \tag{A.25}$$

$$\frac{d\Psi^>}{dr} + ik_{\mathrm{R}}\Psi^> = 0, \qquad \text{at} \qquad r = R \tag{A.26}$$

The first derivatives are approximated by the following backward difference approximation

$$\frac{d\Psi}{dr} \approx \frac{\Psi_{\mathrm{j}} - \Psi_{\mathrm{j}-1}}{h_{\mathrm{j}-1}} \tag{A.27}$$

and the following forward difference approximation

$$\frac{d\Psi}{dr} \approx \frac{\Psi_{\mathrm{j}+1} - \Psi_{\mathrm{j}}}{h_{\mathrm{j}}} \tag{A.28}$$

where, $h_{\mathrm{j}-1}$ is the mesh spacing

$$h_{\mathrm{j}-1} = r_{\mathrm{j}} - r_{\mathrm{j}-1} \tag{A.29}$$

The second derivative is approximated as

$$\frac{d^2\Psi}{dr^2} \approx \frac{\Psi_{\mathrm{j}+1}}{h_{\mathrm{avg_j}} h_{\mathrm{j}}} - \frac{2\Psi_{\mathrm{j}}}{h_{\mathrm{j}-1} h_{\mathrm{j}}} + \frac{\Psi_{\mathrm{j}-1}}{h_{\mathrm{j}-1} h_{\mathrm{avg_j}}} \tag{A.30}$$

where,

$$h_{\mathrm{avg_j}} = \frac{h_{\mathrm{j}} + h_{\mathrm{j}-1}}{2} \tag{A.31}$$

The differential equations, the boundary and matching conditions can be discretized using finite differences. They are then combined and this leads to a tridiagonal system of equations.

$$a_{\mathrm{j}}\Psi_{\mathrm{j}-1} + b_{\mathrm{j}}\Psi_{\mathrm{j}} + E_{\mathrm{j}}\Psi_{\mathrm{j}+1} = 0 \tag{A.32}$$

where j = 1,2,… p-1,p+1,… ,N-1 and, the boundary condition $\Psi_0 = 0$ is used in the equation (A.32).

At the source position $r = r_{\mathrm{s}}$, j = s

$$w_{\mathrm{s}}\Psi_{\mathrm{s}-1} + v_{\mathrm{s}}\Psi_{\mathrm{s}} + u_{\mathrm{s}}\Psi_{\mathrm{s}+1} = 1 \tag{A.33}$$

At j = N, the radiation condition is applied

$$\beta_{\mathrm{N}}\Psi_{\mathrm{N}-1} + \alpha_{\mathrm{N}}\Psi_{\mathrm{N}} = 0 \tag{A.34}$$

where,

$$a_{\mathrm{j}} = \frac{1}{h_{\mathrm{j}-1} h_{\mathrm{avg}_{\mathrm{j}}}} \tag{A.35}$$

$$b_{\mathrm{j}} = k_{\mathrm{j}}^2 - F_{\mathrm{j}} \tag{A.36}$$

$$F_{\mathrm{j}} = \frac{2}{h_{\mathrm{j}-1} h_{\mathrm{j}}} \tag{A.37}$$

$$E_{\mathrm{j}} = \frac{1}{h_{\mathrm{j}} h_{\mathrm{avg}_{\mathrm{j}}}} \tag{A.38}$$

$$w_{\mathrm{s}} = \frac{1}{h_{\mathrm{s}-1}} \tag{A.39}$$

$$u_{\mathrm{s}} = \frac{1}{h_{\mathrm{s}}} \tag{A.40}$$

$$v_{\mathrm{s}} = -(u_{\mathrm{s}} + w_{\mathrm{s}}) \tag{A.41}$$

$$\beta_{\mathrm{N}} = -\frac{1}{h_{\mathrm{N}-1}} \tag{A.42}$$

$$\alpha_{\mathrm{N}} = -\beta_{\mathrm{N}} + ik_N \tag{A.43}$$

Equations (A.32), (A.33) & (A.34) can be rewritten as a matrix equation

$$A_\omega \boldsymbol{X}_{\boldsymbol{\Psi}} = \boldsymbol{b}_{\mathrm{s}} \tag{A.44}$$

Where $A_\omega$ is a N X N tridiagonal matrix. $\boldsymbol{X}_{\boldsymbol{\Psi}} = (\Psi_1, \ldots, \Psi_{\mathrm{N}})^T$ is the unknown Green's function that needs to be computed by solving equation (A.44) for each frequency $\omega$. The right hand side vector $\boldsymbol{b}_{\mathrm{s}} = (0, \ldots, 1, \ldots, 0)^T$, contains a 1 at location $j = s$ in the array corresponding to the source location $r = r_{\mathrm{s}}$.

$$A_\omega = \begin{pmatrix} b_1 & E_1 & 0 & 0 & 0 & 0 & \dots & 0 \\ a_2 & b_2 & E_2 & 0 & 0 & 0 & \dots & 0 \\ 0 & a_3 & b_3 & E_3 & 0 & 0 & \dots & 0 \\ \vdots & \vdots & \ddots & \ddots & \ddots & \vdots & & \vdots \\ \vdots & 0 & 0 & w_\mathrm{s} & v_\mathrm{s} & u_\mathrm{s} & \dots & 0 \\ \vdots & \vdots & \vdots & \vdots & \ddots & \ddots & \ddots & \vdots \\ 0 & \dots & 0 & 0 & 0 & a_{\mathrm{N}-1} & b_{\mathrm{N}-1} & E_{\mathrm{N}-1} \\ 0 & \dots & 0 & 0 & 0 & 0 & \beta_\mathrm{N} & \alpha_\mathrm{N} \end{pmatrix} \tag{A.45}$$

## A.3 Green's function for the potential well

From chapter 2, equation (2.4) we have

$$\frac{d^2\Psi}{dr^2} + \frac{\omega_1^2 - V(r)}{c^2}\Psi = \delta(r - r_\mathrm{s}) \tag{A.46}$$

where $\Psi$ is proportional to the pressure perturbation.

$$\omega_1^2 = (\omega^2 + i\omega\Gamma) \tag{A.47}$$

The source is placed inside the well, $0 < r_\mathrm{s} < a$. Without loss of generality consider frequencies $\omega < \omega_\mathrm{c}$. The solution $\Psi = 0$ at $r = 0$ and the radiation condition is applied far away from the upper turning point $r = a$. This ensures propagating waves for frequencies $\omega > \omega_\mathrm{c}$ and exponential decay for waves with $\omega < \omega_\mathrm{c}$.

The above equation with the boundary conditions needs to be solved in the three regions:

i) $0 \le r < r_\mathrm{s}$: satisfied by $\Psi_1$, with $\Psi_1 = 0$ at $r = 0$.

ii) $r_\mathrm{s} < r < a$: satisfied by $\Psi_2$.

iii) $r \ge a$: satisfied by an exponentially decaying solution $\Psi_3$.

These three solutions satisfy three different differential equations in each of the three regions.

$$\frac{d^2\Psi_1}{dr^2} + W_1^2\Psi_1 = 0 \tag{A.48}$$

$$\frac{d^2\Psi_2}{dr^2} + W_1^2\Psi_2 = 0 \tag{A.49}$$

$$\frac{d^2\Psi_3}{dr^2} - W_2^2\Psi_2 = 0 \tag{A.50}$$

where,

$$W_1 = \frac{\omega_1}{c} \tag{A.51}$$

$$W_2 = \frac{\omega_2}{c} \tag{A.52}$$

$$\omega_2^2 = (\omega_{\mathrm{c}}^2 - \omega_1^2) \tag{A.53}$$

The solutions to the differential equations with the boundary conditions are:

$$\Psi_1(r) = c_1 \sin(W_1 r) \tag{A.54}$$

$$\Psi_2(r) = c_2 \sin(W_1 r) + c_3 \cos(W_1 r) \tag{A.55}$$

$$\Psi_3(r) = c_4 e^{-W_2 r} \tag{A.56}$$

The constants $c_1, c_2, c_3$ and $c_4$ are obtained by applying matching conditions at $r = r_{\mathrm{s}}$ and $r = a$.

At $r = r_{\mathrm{s}}$ due to the delta function, the solution is continuous, but there is a jump in the first derivative.

$$\Psi_1(r_{\mathrm{s}}) = \Psi_2(r_{\mathrm{s}}) \tag{A.57}$$

$$\frac{d\Psi_2}{dr} - \frac{d\Psi_1}{dr} = 1, \qquad \text{at} \qquad r = r_{\mathrm{s}} \tag{A.58}$$

At $r = a$, both the function and its first derivative are continuous.

$$\Psi_2(a) = \Psi_3(a) \tag{A.59}$$

$$\frac{d\Psi_2}{dr} = \frac{d\Psi_3}{dr}, \qquad \text{at} \qquad r = a \tag{A.60}$$

Applying these matching conditions and carrying out the algebra, the constant $c_4$ is

$$c_4 = -\frac{\sin(W_1 r_\mathrm{s})}{W_1 \cos(W_1 a) + W_2 \sin(W_1 a)} e^{W_2 a} \tag{A.61}$$

The Green's function at $r \geq a$ is $G_\Psi(r, r_\mathrm{s}) = \Psi_3(r) = c_4 e^{-W_2 r}$

$$G_\Psi(r, r_\mathrm{s}) = \frac{-c\ \sin(\omega_1 r_\mathrm{s}/c)}{\omega_1 \mathrm{cos}(\omega_1 a/c) + \omega_2 \mathrm{sin}(\omega_1 a/c)} e^{-\omega_2 (r-a)/c} \tag{A.62}$$

For frequencies $\omega > \omega_\mathrm{c}$, $\omega_2$ becomes imaginary. Replacing $\omega_2$ by $ik$ in the above expression (A.62), we get the corresponding Green's function. Where $k$ is

$$k^2 = (\omega_1^2 - \omega_\mathrm{c}^2) \tag{A.63}$$

## A.4 Eigenfrequencies for the potential well

The governing equation for the eigenfrequency $\omega_0$ is

$$\frac{d^2\Psi}{dr^2} + \frac{\omega_0^2 - V(r)}{c^2}\Psi = 0 \tag{A.64}$$

where $\Psi$ is proportional to the pressure perturbation.

Without loss of generality consider eigenfrequencies $\omega_0 < \omega_\mathrm{c}$. The solution $\Psi = 0$ at $r = 0$ and the radiation condition is applied far away from the upper turning point $r = a$. This ensures propagating waves for eigenfrequencies $\omega_0 > \omega_\mathrm{c}$ and exponential decay for waves with $\omega_0 < \omega_\mathrm{c}$.

The above equation (A.64) with the boundary conditions needs to be solved in the two regions:

i) $0 \leq r < a$: satisfied by $\Psi_1$, with $\Psi_1 = 0$ at $r = 0$.

ii) $r \geq a$: satisfied by an exponentially decaying solution $\Psi_2$.

These two solutions satisfy two different differential equations in each of the two regions.

$$\frac{d^2\Psi_1}{dr^2} + W_0^2\Psi_1 = 0 \tag{A.65}$$

$$\frac{d^2\Psi_2}{dr^2} - W_{0\mathrm{c}}^2\Psi_2 = 0 \tag{A.66}$$

where,

$$W_0 = \frac{\omega_0}{c} \tag{A.67}$$

$$W_{0\mathrm{c}} = \frac{\omega_{0\mathrm{c}}}{c} \tag{A.68}$$

$$\omega_{0\mathrm{c}}^2 = (\omega_\mathrm{c}^2 - \omega_0^2) \tag{A.69}$$

The solutions to the differential equations with the boundary conditions are:

$$\Psi_1(r) = c_1 \sin(W_0 r) \tag{A.70}$$

$$\Psi_2(r) = c_4 e^{-W_{0\mathrm{c}} r} \tag{A.71}$$

Applying the matching condition at $r = a$:

$$\Psi_1(a) = \Psi_2(a) \tag{A.72}$$

$$\frac{d\Psi_1}{dr} = \frac{d\Psi_2}{dr}, \qquad \text{at} \qquad r = a \tag{A.73}$$

This gives the equation for the eigenfrequency $\omega_0$

$$\omega_{0\mathrm{c}} \sin(W_0 a) + W_0 \cos(W_0 a) = 0 \tag{A.74}$$

The equation (A.74) also holds for eigenfrequencies $\omega_0 > \omega_{\mathrm{c}}$, in which case $\omega_{0\mathrm{c}}$ becomes imaginary.

# Appendix B

# Phase and Amplitude differences

In this appendix the equations used in chapter 3 are derived.

The Green's function is given by (from equation (A.62))

$$G_{\Psi}(\omega_1) = \frac{-c\ \sin(\omega_1 r_{\rm s}/c)}{\omega_1 \cos(\omega_1 a/c) + \omega_2 \sin(\omega_1 a/c)} e^{-\omega_2 (r-a)/c} \tag{B.1}$$

where $\omega_1$ and $\omega_2$ are given by:

$$\omega_1^2 = (\omega^2 + i\omega\Gamma) \tag{B.2}$$

$$\omega_2^2 = (\omega_{\rm c}^2 - \omega_1^2) \tag{B.3}$$

For solar p modes the damping coefficient $\Gamma \ll \omega$, using the binomial expansion, equation (B.2) becomes

$$\omega_1 = \omega + i\Gamma/2 \tag{B.4}$$

The denominator $D$ of equation (B.1) is

$$D = \omega_1 \cos(\omega_1 a/c) + \omega_2 \sin(\omega_1 a/c) \tag{B.5}$$

The above equation (B.5) can be rewritten as

$$D = \omega_{\rm c} \sin(\omega_1 a/c + \phi_{\rm c}) \tag{B.6}$$

where

$$\sin \phi_{\mathrm{c}} = \frac{\omega_1}{\omega_{\mathrm{c}}} \approx \frac{\omega}{\omega_{\mathrm{c}}} \tag{B.7}$$

From equation (1.29) $\delta p = u\Psi$ and since the Green's function is proportional to $\Psi$, therefore $\delta p \propto G_{\Psi}$. Taking into account the time dependence $e^{i\omega t}$, for modes below the acoustic cutoff frequency $\omega_{\mathrm{c}}$

$$\delta p \propto -\frac{\alpha c}{\omega_{\mathrm{c}}} e^{i\omega t} e^{-\omega_{\mathrm{c}}(r-a)/c} \tag{B.8}$$

where $\alpha$ is a complex analytical function of $\omega$, $a$, $r_{\mathrm{s}}$, $c$ and the damping, and is given by

$$\alpha = \frac{\sin(\omega_1 r_{\mathrm{s}}/c)}{\sin(\omega_1 a/c + \phi_{\mathrm{c}})} \tag{B.9}$$

Using the equation of continuity, and the adiabatic relation,

$$\frac{d\delta\rho}{dt} + \rho\frac{d\delta v}{dr} = 0 \tag{B.10}$$

$$\delta\rho = \frac{\delta p}{c^2} \tag{B.11}$$

the velocity perturbation is given by

$$\delta v = \frac{\delta p\, \omega}{c\rho\omega_{\mathrm{c}}} e^{i\pi/2} \tag{B.12}$$

where $\rho$ is the density which has been assumed to be constant in this simple model. Without loss of generality both the pressure and velocity perturbations can be evaluated at the upper turning point $r = a$.

The cross spectrum $S_{\mathrm{xy}}$ between two complex numbers $x = r_{\mathrm{x}}e^{i\theta_{\mathrm{x}}}$ and $y = r_{\mathrm{y}}e^{i\theta_{\mathrm{y}}}$ is defined as

$$S_{\mathrm{xy}} = xy^* = r_{\mathrm{x}} r_{\mathrm{y}} e^{i(\theta_{\mathrm{x}} - \theta_{\mathrm{y}})} \tag{B.13}$$

The modulus of $S_{\mathrm{xy}}$ is $r_{\mathrm{x}} r_{\mathrm{y}}$ and its phase is $\theta_{\mathrm{x}} - \theta_{\mathrm{y}}$.

The power contrast of the power of quantity $\psi$ ($p$ or $v$), $P_{\psi}$, relative to the power of the uncorrelated background $P_{\psi,\mathrm{uncor}}$, is $C_\psi$ and is given by

$$C_\psi = \frac{(\delta\psi + N_{\psi,\mathrm{cor}})(\delta\psi + N_{\psi,\mathrm{cor}})^*}{P_{\psi,\mathrm{uncor}}} \tag{B.14}$$

where $\psi$ can be $p$ or $v$, and $C_\psi = P_\psi / P_{\psi,\mathrm{uncor}}$.

$$C_\psi = \frac{|\delta\psi|^2}{P_{\psi,\mathrm{uncor}}} + \beta_\psi \left[1 + \frac{\delta\psi N^*_{\psi,\mathrm{cor}} + \delta\psi^* N_{\psi,\mathrm{cor}}}{|N_{\psi,\mathrm{cor}}|^2}\right] \tag{B.15}$$

where $\beta_\psi = |N_{\psi,\mathrm{cor}}|^2 / P_{\psi,\mathrm{uncor}}$ is the ratio of the power of correlated, $|N_{\psi,\mathrm{cor}}|^2$, to uncorrelated noise.

The above equation (B.15) can be rewritten, using the fact $|N_{\psi,\mathrm{cor}}|^2 = N_{\psi,\mathrm{cor}} N^*_{\psi,\mathrm{cor}}$, as

$$C_\psi = \frac{|\delta\psi|^2}{P_{\psi,\mathrm{uncor}}} + \beta_\psi \left[1 + \left(\frac{\delta\psi}{N_{\psi,\mathrm{cor}}} + \frac{\delta\psi^*}{N^*_{\psi,\mathrm{cor}}}\right)\right] \tag{B.16}$$

Further, by considering that

$$\frac{\delta\psi}{N_{\psi,\mathrm{cor}}} + \frac{\delta\psi^*}{N^*_{\psi,\mathrm{cor}}} = 2\mathrm{Re}\left(\frac{\delta\psi}{N_{\psi,\mathrm{cor}}}\right) \tag{B.17}$$

The expression of the power contrast in equation (B.16) is then (see also Eq. (3.9))

$$C_\psi = \frac{|\delta\psi|^2}{P_{\psi,\mathrm{uncor}}} + \beta_\psi \left[1 + 2\mathrm{Re}\left(\frac{\delta\psi}{N_{\psi,\mathrm{cor}}}\right)\right] \tag{B.18}$$

# Appendix C

# Fitting formula

Derivations of the various equations in chapter 4 of the thesis are carried out here. In §C.1 the asymmetrical fitting formula is derived. In §C.2 the basic idea of fitting is explained. Finally, in §C.3 the eigenfrequencies of the solar model are computed numerically, for both reflecting and radiation boundary conditions.

## C.1 Derivation of the fitting formula

The Green's function is

$$G_{\Psi}(\omega_1) = \frac{-c\ \sin(\omega_1 r_{\rm s}/c)}{\omega_1 \cos(\omega_1 a/c) + \omega_2 \sin(\omega_1 a/c)} e^{-\omega_2 (r-a)/c} \tag{C.1}$$

where $\omega_1$ and $\omega_2$ are given by:

$$\omega_1^2 = (\omega^2 + i\omega\Gamma) \tag{C.2}$$

$$\omega_2^2 = (\omega_{\rm c}^2 - \omega_1^2) \tag{C.3}$$

For solar p modes the damping coefficient $\Gamma \ll \omega$, using the binomial expansion equation (C.2) becomes

$$\omega_1 = \omega + i\Gamma/2 \tag{C.4}$$

Without loss of generality the Green's function can be evaluated at the observing location $r = a$. The denominator $D$ of equation (C.1) is

$$D = \omega_1 \cos(\omega_1 a/c) + \omega_2 \sin(\omega_1 a/c) \tag{C.5}$$

The above equation (C.5) can be rewritten as

$$D = \omega_{\rm c} \sin(\omega_1 a/c + \phi_{\rm c}) \tag{C.6}$$

where

$$\sin \phi_{\rm c} = \frac{\omega_1}{\omega_{\rm c}} \approx \frac{\omega}{\omega_{\rm c}} \tag{C.7}$$

Substituting the expression for $\omega_1$ from equation (C.4) in equation (C.6) for $D$ one gets

$$D = \omega_{\rm c} \left[ \sin\left(\frac{\omega a}{c} + \phi_{\rm c}\right) \cos\left(\frac{i\Gamma a}{2c}\right) + \cos\left(\frac{\omega a}{c} + \phi_{\rm c}\right) \sin\left(\frac{i\Gamma a}{2c}\right) \right] \tag{C.8}$$

Define a dimensionless parameter $\beta = \Gamma a/c$ and expanding the above equation for small $\beta$ one gets

$$D \approx \omega_{\rm c} \left[ \sin\left(\frac{\omega a}{c} + \phi_{\rm c}\right) + \frac{i\beta}{2} \cos\left(\frac{\omega a}{c} + \phi_{\rm c}\right) \right] \tag{C.9}$$

Next, we define a dimensionless line profile parameter $X = \frac{\omega - \omega_0}{\Gamma}$ and substitute for $\omega$ in terms of $X$ and $\omega_0$, the sin and cos terms become

$$\sin\left(\frac{\omega a}{c} + \phi_{\rm c}\right) = \sin\left(\frac{\omega_0 a}{c} + \phi_{\rm c}\right) \cos(\beta X) + \cos\left(\frac{\omega_0 a}{c} + \phi_{\rm c}\right) \sin(\beta X) \tag{C.10}$$

$$\cos\left(\frac{\omega a}{c} + \phi_{\rm c}\right) = \cos\left(\frac{\omega_0 a}{c} + \phi_{\rm c}\right) \cos(\beta X) - \sin\left(\frac{\omega_0 a}{c} + \phi_{\rm c}\right) \sin(\beta X) \tag{C.11}$$

The above follow from the fact that

$$\frac{\omega a}{c} + \phi_{\mathrm{c}} = \left(\frac{\omega_0 a}{c} + \phi_{\mathrm{c}}\right) + \beta X \tag{C.12}$$

At the eigenfrequency $\omega = \omega_0$ (see Appendix A.4):

$$\sin\left(\frac{\omega_0 a}{c} + \phi_{\mathrm{c}}\right) = 0 \tag{C.13}$$

$$\cos\left(\frac{\omega_0 a}{c} + \phi_{\mathrm{c}}\right) = 1 \tag{C.14}$$

Using the above equations (C.9) through (C.14) the expression for $D$ becomes

$$D = \omega_{\mathrm{c}}\left[\sin(\beta X) + \frac{i\beta}{2}\cos(\beta X)\right] \tag{C.15}$$

This can then be expanded for small $\beta X$ to yield

$$D = \omega_{\mathrm{c}}\beta\left(X + \frac{i}{2}\right) \tag{C.16}$$

Now returning to the numerator $N$ of the Green's function

$$N = -c\ \sin(\omega_1 r_{\mathrm{s}}/c) \tag{C.17}$$

We define the depth of the source from the upper turning point $r = a$ as $d_{\mathrm{s}} = a - r_{\mathrm{s}}$. Substituting the expression for $r_{\mathrm{s}}$ in terms of $d_{\mathrm{s}}$ into the argument of the sin in equation (C.17)

$$\sin(\omega_1 r_{\mathrm{s}}/c) = \sin\left(\frac{\omega_1 a}{c} - \frac{\omega_1 d_{\mathrm{s}}}{c}\right) \tag{C.18}$$

The right hand side can be expanded using the standard trigonometric identity

$$\sin(\omega_1 r_{\mathrm{s}}/c) = \sin\left(\frac{\omega_1 a}{c}\right)\cos\left(\frac{\omega_1 d_{\mathrm{s}}}{c}\right) - \cos\left(\frac{\omega_1 a}{c}\right)\sin\left(\frac{\omega_1 d_{\mathrm{s}}}{c}\right) \tag{C.19}$$

Using the expression for $\omega_1$ the above equation (C.19) becomes

$$\sin(\omega_1 r_{\mathrm{s}}/c) = \sin\left(\frac{\omega a}{c} + \frac{i\beta}{2}\right)\cos\left(\frac{\omega d_{\mathrm{s}}}{c} + \frac{i\Gamma d_{\mathrm{s}}}{2c}\right) - \cos\left(\frac{\omega a}{c} + \frac{i\beta}{2}\right)\sin\left(\frac{\omega d_{\mathrm{s}}}{c} + \frac{i\Gamma d_{\mathrm{s}}}{2c}\right) \tag{C.20}$$

The above equation (C.20) can be simplified for small $\beta$ and $\frac{\Gamma d_{\mathrm{s}}}{c}$

$$S \approx \left[\sin\left(\frac{\omega a}{c}\right) + \frac{i\beta}{2}\cos\left(\frac{\omega a}{c}\right)\right]\cos\left(\frac{\omega d_{\mathrm{s}}}{c}\right) - \left[\cos\left(\frac{\omega a}{c}\right) - \frac{i\beta}{2}\sin\left(\frac{\omega a}{c}\right)\right]\sin\left(\frac{\omega d_{\mathrm{s}}}{c}\right) \tag{C.21}$$

Where we have used the fact that $\cos(y) \approx 1$ and $\sin(y) \approx y$ for small $y$ and $S = \sin(\omega_1 r_{\mathrm{s}}/c)$. Substituting $\omega = \omega_0 + X\Gamma$ into the above equation (C.21) and using the eigenvalue condition $\frac{\omega_0 a}{c} = n\pi - \phi_{\mathrm{c}}$, where $n = 0, 1, ...$ Without loss of generality consider $n = 0$. With this substitution and approximating for small $\frac{\Gamma d_{\mathrm{s}}}{c}$ the equation (C.21) becomes

$$S \approx \left[\sin(\beta X - \phi_{\mathrm{c}}) + \frac{i\beta}{2}\cos(\beta X - \phi_{\mathrm{c}})\right]\cos p_0 - \left[\cos(\beta X - \phi_{\mathrm{c}}) - \frac{i\beta}{2}\sin(\beta X - \phi_{\mathrm{c}})\right]\sin p_0 \tag{C.22}$$

where $p_0 = \frac{\omega_0 d_{\mathrm{s}}}{c}$. The above equation (C.22) can be simplified to

$$S = \sin(\beta X - p_{\mathrm{w}}) + \frac{i\beta}{2}\cos(\beta X - p_{\mathrm{w}}) \tag{C.23}$$

where $p_{\mathrm{w}} = p_0 + \phi_{\mathrm{c}}$.

The Green's function then becomes

$$G_\Psi \approx \frac{-c\ \left[\sin(\beta X - p_{\mathrm{w}}) + \frac{i\beta}{2}\cos(\beta X - p_{\mathrm{w}})\right]}{\omega_{\mathrm{c}}\left[\sin(\beta X) + \frac{i\beta}{2}\cos(\beta X)\right]} \tag{C.24}$$

We get the complex amplitude of the pressure perturbation $A_\Psi$ from the Green's function

$$A_\Psi(X) = -A_{\mathrm{w}}\frac{\sin(\beta X - p_{\mathrm{w}}) + \frac{i}{2}\beta\cos(\beta X - p_{\mathrm{w}})}{\sin(\beta X) + \frac{i}{2}\beta\cos(\beta X)} \tag{C.25}$$

Here $A_{\mathrm{w}} = A_0 c/\omega_{\mathrm{c}}$, $A_0$ is the mode amplitude that has been multiplied by the Green's function. Correlated noise $N_{\mathrm{cor}}$ is added to the amplitude. The power is then given by $P = |N_{\mathrm{cor}} + A_{\Psi}|^2$. This gives a trigonometric expression for the power and is,

$$P(X) = F^2 + \frac{(G\beta)^2\left[\cos^2(\beta X) + \frac{\beta^2}{4}\sin^2(\beta X)\right]}{\sin^2(\beta X) + \frac{\beta^2}{4}\cos^2(\beta X)} + \frac{FG\beta\sin(2\beta X)(1-\frac{\beta^2}{4})}{\sin^2(\beta X) + \frac{\beta^2}{4}\cos^2(\beta X)} \tag{C.26}$$

where $F = N_{\mathrm{cor}} - A_{\mathrm{w}} q_{\mathrm{w}}$ and $G = \frac{A_{\mathrm{w}}(1-q_{\mathrm{w}}^2)^{1/2}}{\beta}$ and $q_{\mathrm{w}} = \cos p_{\mathrm{w}}$.

Neglecting the small terms $\frac{\beta^2}{4}\sin^2(\beta X)$ incomparison with $\cos^2(\beta X)$ and $\frac{\beta^2}{4}$ compared to 1, and making use of the transformation $x = 2X$ the above expression (C.26) can be written as

$$P(x) \approx AB^2 + AU^2\frac{\left[\cos^2(Ux) + U^2\sin^2(Ux)\right]}{\sin^2(Ux) + U^2\cos^2(Ux)} + \frac{ABU\sin(2Ux)}{\sin^2(Ux) + U^2\cos^2(Ux)} \tag{C.27}$$

where $x = 2(\nu - \nu_0)/\gamma$, cyclic frequency $\nu = \omega/2\pi$, $\gamma = \Gamma/2\pi$ $A = 4A_{\mathrm{w}}^2(1-q_{\mathrm{w}}^2)\beta^{-2}$, $B = 0.5\beta(N_{\mathrm{cor}} - A_{\mathrm{w}}q_{\mathrm{w}})A_{\mathrm{w}}^{-1}(1-q_{\mathrm{w}}^2)^{-1/2}$, $U = \beta/2$, $p_{\mathrm{w}} = p_0 + \phi_{\mathrm{c}}$, $p_0 = \omega_0 d_{\mathrm{s}}/c$, $\sin\phi_{\mathrm{c}} \approx \omega/\omega_{\mathrm{c}}$ and $d_{\mathrm{s}} = a - r_{\mathrm{s}}$

This trigonometric expression (C.27) can be written in compact form after neglecting $U^2\sin^2(Ux)$ in comparison to $\cos^2(Ux)$

$$P(x) \approx A\frac{\left[U\cos(Ux) + B\sin(Ux)\right]^2 + B^2U^2\cos^2(Ux)}{U^2\cos^2(Ux) + \sin^2(Ux)} \tag{C.28}$$

This expression can be used to fit multiple peaks. The ratio $a/c$ is the travel time of the p modes between the upper and lower turning points, and is $a/c = 1/2\Delta\nu$, where $\Delta\nu$ is the mode spacing. Using this fact the dimensionless parameter $U = \pi\gamma/2\Delta\nu$.

The equation (C.28) is then simplified to a more practical polynomial expression which is obtained by expanding equation for small $Ux$, with the $U$ canceling out:

$$P(x) \approx A\frac{(1+Bx)^2 + B^2}{1+x^2} + B_{\mathrm{l}} \tag{C.29}$$

To this one can add the linear uncorrelated background $B_{\mathrm{l}} = c_1 + c_2\nu$, where $c_1$ and $c_2$ are fitting parameters, which results in equation (4.4) in chapter 4 of the main text.

## C.2 Fitting power spectra by the formula

Given a target power spectrum $P_t(\nu)$, fitting is carried out by minimizing the square of the difference between the power estimated by the above formula $P(\nu)$ and $P_t(\nu)$, summed over a suitable range so as to isolate the mode.

$$\Delta = \sum_{j=1}^{\mathrm{N}} \left[P_t(\nu_j) - P(\nu_j)\right]^2 \tag{C.30}$$

where, $\nu_1, \nu_2, \ldots, \nu_{\mathrm{N}}$ are the N frequency mesh points.

The nonlinear minimization of $\Delta$ is done with respect to a set of six parameters $S = \{A, B, \gamma, \nu_0, c_1, c_2\}$ using Powell's algorithm from the IDL library.

$$\min_S \Delta \tag{C.31}$$

## C.3 Numerical solution of the eigenvalue problem

### C.3.1 Reflecting boundary conditions

The eigenfrequencies $\omega_0$ of the solar model are computed from the following equation

$$\frac{d^2\Psi}{dr^2} + \frac{\omega_0^2 - \omega_+^2}{c^2}\Psi = 0, \tag{C.32}$$

For computing just the bound states, reflecting boundary conditions $\Psi = 0$ at $r = 0$ and $r = R$ is applied. The above equation (C.32) is discretized using a non-uniform mesh, by using finite difference approximation to the derivative. The following notation is used $\Psi_{\mathrm{j}} = \Psi(r_{\mathrm{j}})$, $c_{\mathrm{j}} = c(r_{\mathrm{j}})$ and similarly for the other variables.

The second derivative is approximated as

$$\frac{d^2\Psi}{dr^2} \approx \frac{\Psi_{\mathrm{j+1}}}{h_{\mathrm{avg_j}} h_{\mathrm{j}}} - \frac{2\Psi_{\mathrm{j}}}{h_{\mathrm{j-1}} h_{\mathrm{j}}} + \frac{\Psi_{\mathrm{j-1}}}{h_{\mathrm{j-1}} h_{\mathrm{avg_j}}} \tag{C.33}$$

This leads to a tridiagonal system of equations for j $= 1, \ldots$ ,N-1 with boundary conditions $\Psi_0 = \Psi_{\mathrm{N}} = 0$.

$$a_{\mathrm{j}} \Psi_{\mathrm{j-1}} + (b_{\mathrm{j}} - \omega_0^2)\Psi_{\mathrm{j}} + E_{\mathrm{j}} \Psi_{\mathrm{j+1}} = 0 \tag{C.34}$$

where

$$a_{\mathrm{j}} = -\frac{c_{\mathrm{j}}^2}{h_{\mathrm{j-1}} h_{\mathrm{avg_j}}} \tag{C.35}$$

$$b_{\mathrm{j}} = F_{\mathrm{j}} + \omega_{+\mathrm{j}}^2 \tag{C.36}$$

$$E_{\mathrm{j}} = -\frac{c_{\mathrm{j}}^2}{h_{\mathrm{j}} h_{\mathrm{avg_j}}} \tag{C.37}$$

$$F_{\mathrm{j}} = \frac{2c_{\mathrm{j}}^2}{h_{\mathrm{j-1}} h_{\mathrm{j}}} \tag{C.38}$$

$$h_{\mathrm{avg_j}} = \frac{h_{\mathrm{j}} + h_{\mathrm{j-1}}}{2} \tag{C.39}$$

$$h_{\mathrm{j-1}} = r_{\mathrm{j}} - r_{\mathrm{j-1}} \tag{C.40}$$

Equation (C.34) can be rewritten as a matrix eigenvalue problem

$$A_\omega \boldsymbol{X_\Psi} = \mathbf{0} \tag{C.41}$$

Where $A_\omega = A_0 - \omega_0^2 I$. The eigenvalues of the (N-1)X(N-1) tridiagonal matrix $A_0$ are nothing but $\omega_0^2$, $I$ is the (N-1)X(N-1) identity matrix, $\boldsymbol{X_\Psi} = (\Psi_1, \ldots, \Psi_{\mathrm{N-1}})^T$ is the eigenvector corresponding to the eigenvalue and $\mathbf{0} = (0, \ldots, 0)^T$.

$$A_0 = \begin{pmatrix} b_1 & E_1 & 0 & 0 & 0\dots & 0 \\ a_2 & b_2 & E_2 & 0 & 0\dots & 0 \\ 0 & a_3 & b_3 & E_3 & 0\dots & 0 \\ \vdots & \vdots & \ddots & \ddots & \ddots & \vdots \\ 0 & & \dots & a_{\mathrm{N}-2} & b_{\mathrm{N}-2} & E_{\mathrm{N}-2} \\ 0 & \dots & 0 & 0 & a_{\mathrm{N}-1} & b_{\mathrm{N}-1} \end{pmatrix} \tag{C.42}$$

### C.3.2 Radiation condition

The eigenfrequencies for the solar model can also be computed when the Sommerfeld radiation condition is applied far away from the upper turning point. The problem is formulated as follows:

Equation (C.32) can be rewritten as,

$$c^2 \frac{d^2\Psi}{dr^2} + \omega_0^2 \Psi - \omega_+^2 \Psi = 0, \tag{C.43}$$

This is subject to the following boundary conditions: At $r = 0$

$$\Psi = 0 \tag{C.44}$$

At $r = R$, the radiation condition is applied to ensure outgoing waves. A harmonic time dependence of $e^{i\omega t}$ is used.

$$\frac{d\Psi}{dr} + ik_{\mathrm{R}} \Psi = 0 \tag{C.45}$$

where,

$$k^2(r) = \frac{\omega_0^2 - \omega_+^2(r)}{c^2(r)} \tag{C.46}$$

Evaluating equation (C.46) at $r = R$ leads to

$$k_{\mathrm{R}}^2 = k^2(R) = \frac{\omega_0^2 - \omega_{+\mathrm{R}}^2}{c_{\mathrm{R}}^2} \tag{C.47}$$

From equations (C.43) and (C.47) one obtains

$$\frac{c^2}{c_{\mathrm{R}}^2}\frac{d^2\Psi}{dr^2}+\frac{\omega_{+\mathrm{R}}^2-\omega_{+}^2}{c_{\mathrm{R}}^2}\Psi+k_{\mathrm{R}}^2\Psi=0 \tag{C.48}$$

Defining a new variable $\Phi = k_{\mathrm{R}}\Psi$, one obtains the following set of equations

$$\frac{c^2}{c_{\mathrm{R}}^2}\frac{d^2\Psi}{dr^2}+\frac{\omega_{+\mathrm{R}}^2-\omega_{+}^2}{c_{\mathrm{R}}^2}\Psi+k_{\mathrm{R}}\Phi=0 \tag{C.49}$$

$$k_{\mathrm{R}}\Psi-\Phi=0 \tag{C.50}$$

These equations (C.49) and (C.50) are to be solved subject to the following boundary conditions $\Psi = \Phi = 0$ at $r = 0$.

At $r = R$ the radiation condition is applied on $\Psi$ and $\Phi$

$$\frac{d\Psi}{dr}+ik_{\mathrm{R}}\Psi=0 \tag{C.51}$$

$$\frac{d\Phi}{dr}+ik_{\mathrm{R}}\Phi=0 \tag{C.52}$$

The first derivatives are approximated by the following backward difference approximation

$$\frac{d\Psi}{dr}\approx\frac{\Psi_{\mathrm{j}}-\Psi_{\mathrm{j}-1}}{h_{\mathrm{j}-1}} \tag{C.53}$$

The boundary conditions and the equations can be discretized by using finite differences and are

$$\Psi_0=0 \tag{C.54}$$

$$\Phi_0=0 \tag{C.55}$$

The following equations are written at the interior mesh points j = 1, . . . ,N-1

$$-k_{\mathrm{N}}\Psi_{\mathrm{j}}+\Phi_{\mathrm{j}}=0 \tag{C.56}$$

$$-E_{\mathrm{j-1}}\Psi_{\mathrm{j-1}}-B_{\mathrm{j}}\Psi_{\mathrm{j}}-k_{\mathrm{N}}\Phi_{\mathrm{j}}-A_{\mathrm{j}}\Psi_{\mathrm{j+1}}=0 \tag{C.57}$$

The radiation condition is applied at j = N.

$$-d_{\mathrm{N-1}}\Psi_{\mathrm{N-1}}+(d_{\mathrm{N-1}}-k_{\mathrm{N}})\Psi_{\mathrm{N}}=0 \tag{C.58}$$

$$-d_{\mathrm{N-1}}\Phi_{\mathrm{N-1}}+(d_{\mathrm{N-1}}-k_{\mathrm{N}})\Phi_{\mathrm{N}}=0 \tag{C.59}$$

where

$$E_{\mathrm{j-1}}=\frac{c_{\mathrm{j}}^2}{c_{\mathrm{N}}^2 h_{\mathrm{j-1}} h_{\mathrm{avg_j}}} \tag{C.60}$$

$$A_{\mathrm{j}}=\frac{c_{\mathrm{j}}^2}{c_{\mathrm{N}}^2 h_{\mathrm{j}} h_{\mathrm{avg_j}}} \tag{C.61}$$

$$B_{\mathrm{j}}=\frac{\omega_{+\mathrm{N}}^2-\omega_{+\mathrm{j}}^2}{c_{\mathrm{N}}^2}-\frac{2c_{\mathrm{j}}^2}{c_{\mathrm{N}}^2 h_{\mathrm{j-1}} h_{\mathrm{j}}} \tag{C.62}$$

$$d_{\mathrm{N-1}}=\frac{i}{h_{\mathrm{N-1}}} \tag{C.63}$$

The equations (C.56) through (C.59) can be written compactly in matrix form.

$$A_{\mathrm{k}}\boldsymbol{Y}=\mathbf{0} \tag{C.64}$$

The matrix $A_{\mathrm{k}}$ is a pentadiagonal matrix. Where $A_{\mathrm{k}}=F-k_{\mathrm{N}}I$. The eigenvalues of the 2N X 2N pentadiagonal matrix $F$ are $k_{\mathrm{N}}$, which contain the eigenfrequencies $\omega_0^2$, $I$ is the 2N X 2N identity matrix, $\boldsymbol{Y}=(\Psi_1,\Phi_1,\ldots,\Psi_{\mathrm{N}},\Phi_{\mathrm{N}})^T$ is the eigenvector corresponding to the eigenvalue and $\mathbf{0}=(0,\ldots,0)^T$. From this computation the eigenvalues corresponding to the variables $\Psi_{\mathrm{j}}$ are sorted out before the eigenfrequencies are computed.

$$F = \begin{pmatrix} 0 & 1 & 0 & 0 & 0 & 0 & 0 & 0 & \dots & 0 \\ -B_1 & 0 & -A_1 & 0 & 0 & 0 & 0 & 0 & \dots & 0 \\ 0 & 0 & 0 & 1 & 0 & 0 & 0 & 0 & \dots & 0 \\ -E_1 & 0 & -B_2 & 0 & -A_2 & 0 & 0 & 0 & \dots & 0 \\ 0 & 0 & 0 & 0 & 0 & 1 & 0 & 0 & \dots & 0 \\ \vdots & \vdots & \ddots & \ddots & \ddots & \ddots & \ddots & \vdots & \vdots & \vdots \\ 0 & 0 & 0 & 0 & 0 & 0 & 0 & 1 & \dots & 0 \\ 0 & 0 & 0 & 0 & -E_{\mathrm{N}-2} & 0 & -B_{\mathrm{N}-1} & 0 & -A_{\mathrm{N}-1} & 0 \\ 0 & 0 & 0 & 0 & 0 & 0 & -d_{\mathrm{N}-1} & 0 & d_{\mathrm{N}-1} & 0 \\ 0 & 0 & 0 & 0 & 0 & 0 & 0 & -d_{\mathrm{N}-1} & 0 & d_{\mathrm{N}-1} \end{pmatrix}$$

# Appendix D

# The Source of p modes

The equations relating the excitation of p modes by different source types in Chapter 5 are derived here.

The composite source corresponding to the Lagrangian pressure perturbation is

$$S(r,\omega) = \left[c_1 \frac{dS_2}{dr} + c_2 S_2\right] + \left[c_3 \frac{dS_1}{dr} + c_4 S_1\right], \tag{D.1}$$

where $c_1, c_2, c_3$ and $c_4$ depend on the solar model and are given by:

$$c_1 = 1/u \tag{D.2}$$

where $u$ is defined by equation (1.29)

$$c_2 = z/u \tag{D.3}$$

and $z$ is given by

$$z = A_{11} - \frac{A'_{21}}{A_{21}} = A_{11} - \frac{d(\ln A_{21})}{dr} \tag{D.4}$$

$$c_3 = -\frac{\rho g}{u} \tag{D.5}$$

$$c_4 = -\frac{\left[z\rho g + A_{21} + \frac{d(\rho g)}{dr}\right]}{u} \tag{D.6}$$

$A_{11}$ and $A_{21}$ are given by

$$A_{11} = \frac{2}{r} - \frac{L^2 g}{\omega^2 r^2} \tag{D.7}$$

$$A_{21} = -\frac{g\rho f}{r} \tag{D.8}$$

where $L^2 = l(l+1)$ and $f$ has been defined by equation (1.24).

The above source can be broken up into monopole $S_{\rm mon}$, dipole $S_{\rm dip}$ and quadrupole $S_{\rm qud}$ sources respectively, which are given by

$$S_{\rm mon} = c_4 S_1 \tag{D.9}$$

$$S_{\rm dip-mon} = c_3 \frac{dS_1}{dr} \tag{D.10}$$

where $S_{\rm dip-mon}$ is the dipole source due to monopole

$$S_{\rm dip} = c_1 \frac{dS_2}{dr} + c_2 S_2 \tag{D.11}$$

The pressure perturbation $\delta p$ for these source types can be computed by linear superposition from the Green's function.

$$\Psi(R) = \int_0^R G_\Psi(r, r_{\rm s}) S(r_{\rm s}) dr_{\rm s} \tag{D.12}$$

where $\delta p(r) = u(r)\Psi(r)$.

For a monopole source

$$\Psi_{\rm mon}(R) = \int_0^R G_\Psi(r, r_{\rm s}) c_4(r_{\rm s}) S_1(r_{\rm s}) dr_{\rm s} \tag{D.13}$$

Considering a single source location $r_{\rm s}$ one gets for a monopole source,

$$\delta p_{\mathrm{mon}}(r_{\mathrm{obs}}) \propto c_5(r_{\mathrm{s}}) G_{\Psi}(r_{\mathrm{obs}}, r_{\mathrm{s}}), \tag{D.14}$$

where $c_5(r_{\mathrm{s}})$ is

$$c_5(r_{\mathrm{s}}) = c_4(r_{\mathrm{s}}) u(r_{\mathrm{obs}}) \tag{D.15}$$

For, the dipole source produced by the monopole source $S_{\mathrm{dip-mon}}$, the pressure perturbation is proportional to the Green's function as in equation (D.14) above.

For a dipole source,

$$\Psi_{\mathrm{dip}}(R) = \int_0^R G_{\Psi}(r, r_{\mathrm{s}}) \left[ c_1 \frac{dS_2}{dr_{\mathrm{s}}} + c_2 S_2(r_{\mathrm{s}}) \right] dr_{\mathrm{s}} \tag{D.16}$$

The derivative in the $S_2$ term can be transferred to the Green's function by an integration by parts

$$\int_0^R G_{\Psi}(r, r_{\mathrm{s}}) \frac{dS_2}{dr_{\mathrm{s}}} dr_{\mathrm{s}} = - \int_0^R \frac{dG_{\Psi}(r, r_{\mathrm{s}})}{dr_{\mathrm{s}}} S_2 dr_{\mathrm{s}} \tag{D.17}$$

The other term in the integration by parts $G_{\Psi} S_2$ vanishes at the two limits because the source $S_2$ is localized and is zero at those limits.

$$\Psi_{\mathrm{dip}}(R) = \int_0^R \left[ c_2(r_{\mathrm{s}}) G_{\Psi} - \frac{d\left(c_1(r_{\mathrm{s}}) G_{\Psi}\right)}{dr_{\mathrm{s}}} \right] S_2(r_{\mathrm{s}}) dr_{\mathrm{s}} \tag{D.18}$$

Now, considering a single source location $r_{\mathrm{s}}$ one gets for a dipole source,

$$\delta p_{\mathrm{dip}}(r_{\mathrm{obs}}) \propto c_6(r_{\mathrm{s}}) G_{\Psi} - \frac{d}{dr_{\mathrm{s}}} \left( \frac{G_{\Psi}}{c_7(r_{\mathrm{s}})} \right), \tag{D.19}$$

where $c_6$ and $c_7$ are

$$c_6(r_{\mathrm{s}}) = c_2(r_{\mathrm{s}}) u(r_{\mathrm{obs}}) \tag{D.20}$$

$$c_7(r_{\mathrm{s}}) = \frac{1}{c_1(r_{\mathrm{s}}) u(r_{\mathrm{obs}})} \tag{D.21}$$

Finally, consider the quadrupole source $S_{\mathrm{qud}}$

$$S_2 \approx \frac{dS_{\mathrm{qud}}}{dr} \tag{D.22}$$

where $S_{\mathrm{qud}}$ is equal to the Reynolds stress $\rho\boldsymbol{vv}$. Substituting $S_2$ in equation

$$\Psi_{\mathrm{qud}}(R) = \int_0^R \left( \left[ c_2(r_{\mathrm{s}})G_\Psi - \frac{d\,(c_1(r_{\mathrm{s}})G_\Psi)}{dr_{\mathrm{s}}} \right] \frac{dS_{\mathrm{qud}}}{dr_{\mathrm{s}}} \right) dr_{\mathrm{s}} \tag{D.23}$$

and carrying out a similar integration by parts as was done for the dipole source one gets

$$\delta p_{\mathrm{qud}}(r_{\mathrm{obs}}) \propto \frac{d^2}{dr_{\mathrm{s}}^2} \left( \frac{G_\Psi}{c_7(r_{\mathrm{s}})} \right) - \frac{d}{dr_{\mathrm{s}}} \left( \frac{G_\Psi}{c_8(r_{\mathrm{s}})} \right) \tag{D.24}$$

where $c_8 = 1/c_6$

The radial component of the displacement $\xi$ is computed from $\delta p$ using the equation below

$$\frac{d\delta p}{dr} + \frac{L^2 g}{\omega^2 r^2}\delta p - \frac{g\rho f}{r}\xi = 0 \tag{D.25}$$

The velocity perturbation $\delta v = i\omega\xi$ is then computed for the different source types.

# Bibliography

Abrams, D. and Kumar, P.: 1996, *The Astrophysical Journal* **472**, 882.

Anderson, E. R., Duvall, T. L., and Jefferies, S. M.: 1990, *The Astrophysical Journal* **364**, 699.

Antia, H. M. and Basu, S.: 1999, *The Astrophysical Journal* **519**, 400.

Appourchaux, T., Telljohann, U., Martin, D., Fleur, J., and Leveque, S.: 1995a, in J. T. Hoeksema, V. Domingo, B. Fleck, and B. Battrick (eds.), *Fourth SOHO Workshop Helioseismology. Proceedings. ESA SP-376*, (Paris: ESA) vol.2, 359.

Appourchaux, T., Toutain, T., Gough, D. ., and Kosovichev, A. G.: 1995b, in R. K. Ulrich, E. J. Rhodes, and W. Dappen (eds.), *Helio- And Astero-Seismology from the Earth and Space*, GONG 1994: Astr. Soc. Pac., San Francisco, 76, p. 314-317.

Bahcall, J. N. and Davis, R.: 1976, *Science* **191**, 264.

Balmforth, N. J.: 1992, *Monthly Notices Of The Royal Astronomical Society* **255**, 639.

Bertello, L., Henney, C. J., Ulrich, R. K., Varadi, F., Kosovichev, A. G., Scherrer, P. H., Roca Cortés, T., Thiery, S., Boumier, P., and Turck-Chièze, S.: 1999, *The Astrophysical Journal, submitted.*

Bracewell, R. N.: 1986, *The Fourier Transform and its Applications, 2nd ed., Rev., McGraw-Hill, New York.*

Brown, T. M.: 1991, *The Astrophysical Journal* **371**, 396.

Christensen-Dalsgaard, J.: 1994, *Lecture Notes on Stellar Oscillations: Institut for Fysik og Astronomi, Aarhus Universitet, 3rd ed.*

Christensen-Dalsgaard, J., Dappen, W., Ajukov, S. V., Anderson, E. R., Antia, H. M., Basu, S., Baturin, V. A., Berthomieu, G., Chaboyer, B., Chitre, S. M., Cox, A. N., Demarque, P., Donatowicz, J., Dziembowski, W. A., Gabriel, M., Gough, D. O., Guenther, D. B., Guzik, J. A., Harvey, J. W., Hill, F., Houdek, G., Iglesias, C. A., Kosovichev, A. G., Leibacher, J. W., Morel, P., Proffitt, C. R., Provost, J., Reiter, J., Rhodes, E. J., Rogers, F. J., Roxburgh, I. W., Thompson, M. J., and Ulrich, R. K.: 1996, *Science* **272**, 1286.

Crighton, D. G.: 1975, *Progress In Aerospace Science* **16**, 31.

Deubner, F.-L.: 1975, *Astronomy and Astrophysics* **44**, 371.

Deubner, F.-L. and Fleck, B.: 1989, *Astronomy and Astrophysics* **213**, 423.

Deubner, F.-L., Fleck, B., Schmitz, F., and Straus, T.: 1992, *Astronomy and Astrophysics* **266**, 560.

Duvall, T. L., Jefferies, S. M., Harvey, J. W., Osaki, Y., and Pomerantzi, M. A.: 1993, *The Astrophysical Journal* **410**, 829.

Fossat, E.: 1991, *Solar Physics* **133**, 1.

Frohlich, C., Romero, J., Roth, H., Wehrli, C., Anderson, B. N., Appourchaux, T., Domingo, V., Telljohann, U., Berthomieu, G., Delache, P., Provost, J., Toutain, T., Crommelynck, D. A., Chevalier, A., Fichot, A., Dappen, W., Gough, D. O., Hoeksema, T., Jiménez, A., Gómez, M. F., Herreros, J. M., Roca Cortés, T., Jones, A. R., Pap, J. M., and Willson, R. C.: 1995, *Solar Physics* **162**, 101.

Frohlich, C., Toutain, T., Bonnet, R. M., Bruns, A. V., Delaboudinière, J. P., Domingo, V., Kotov, V. A., Kollath, Z., Rashkovsky, D. N., Vial, J. C., and Wehrli, C.: 1990, in G. Berthomieu and M. Cribier (eds.), *Inside the Sun*, (Dordrecht: Kluwer), 279.

Gabriel, M.: 1992, *Astronomy and Astrophysics* **265**, 771.

Gabriel, M.: 1993, *Astronomy and Astrophysics* **274**, 935.

Gabriel, M.: 1995, *Astronomy and Astrophysics* **299**, 245.

Gabriel, M.: 1998, *Astronomy and Astrophysics* **330**, 359.

Goldreich, P. and Keeley, D. A.: 1977, *The Astrophysical Journal* **212**, 243.

Goldreich, P. and Kumar, P.: 1988, *The Astrophysical Journal* **326**, 462.

Goldreich, P. and Kumar, P.: 1990, *The Astrophysical Journal* **363**, 694.

Goldreich, P., Murray, N., and Kumar, P.: 1994, *The Astrophysical Journal* **424**, 466.

Goode, P. R., Gough, D. O., and Kosovichev, A. G.: 1992, *The Astrophysical Journal*

**387**, 707.

Goode, P. R., Strous, L. H., Rimmele, T. R., and Stebbins, R. T.: 1998, *The Astrophysical Journal* **495**, L27.

Gough, D. O.: 1993, in J. P. Zahn and J. Zinn-Justin (eds.), *Astrophysical Fluid Dynamics*, Elsevier, Amsterdam, 399-560.

Gough, D. O. and Kosovichev, A. G.: 1988, in E. J. Rolfe (ed.), *Seismology of the Sun and Sun-like Stars*, (Paris: ESA), 195.

Houdek, G., Balmforth, N. J., and Christensen-Dalsgaard, J.: 1995, in J. T. Hoeksema, V. Domingo, B. Fleck, and B. Battrick (eds.), *Fourth SOHO Workshop: Helioseismology*, (ESA SP-376; Noordwijk: ESA), 447.

Kumar, P.: 1994, *The Astrophysical Journal* **428**, 827.

Kumar, P. and Basu, S.: 1999, *The Astrophysical Journal* **519**, 389.

Kumar, P. and Lu, E.: 1991, *The Astrophysical Journal* **375**, L35.

Leibacher, J. W. and Stein, R. F.: 1971, *The Astrophysical Journal* **7**, L191.

Leighton, R. B.: 1960, *Proc. IAU Symp.* **12**, 321.

Leighton, R. B., Noyes, R. W., and Simon, G. W.: 1962, *The Astrophysical Journal* **135**, 474.

Lighthill, M. J.: 1952, *Proceedings Of The Royal Society Of London* **A211**, 564.

Lighthill, M. J.: 1953, *Proceedings Of The Royal Society Of London* **A222**, 1.

Marmolino, C. and Severino, G.: 1991, *Astronomy and Astrophysics* **242**, 271.

Milford, P. N. and Nigam, R.: 1995, in R. K. Ulrich, E. J. Rhodes, and W. Dappen (eds.), *Helio- And Astero-Seismology from the Earth and Space*, GONG 1994: Astr. Soc. Pac., San Francisco, 76, p. 504.

Moore, D. W. and Spiegel, E. A.: 1964, *The Astrophysical Journal* **139**, 48.

Nigam, R. and Kosovichev, A. G.: 1996, *Bulletin Of Astronomical Society Of India* **24**, 195.

Nigam, R. and Kosovichev, A. G.: 1998, *The Astrophysical Journal* **505**, L51.

Nigam, R. and Kosovichev, A. G.: 1999a, *The Astrophysical Journal* **510**, L149.

Nigam, R. and Kosovichev, A. G.: 1999b, *The Astrophysical Journal* **514**, L53.

Nigam, R., Kosovichev, A. G., and Scherrer, P. H.: 1997, in J. Provost and F. Schmider (eds.), *Sounding Solar and Stellar Interiors*, Proc. IAU Symp. 181.

Nigam, R., Kosovichev, A. G., Scherrer, P. H., and Schou, J.: 1998, *The Astrophysical Journal* **495**, L115.

Nordlund, A.: 1985, *Solar Physics* **100**, 209.

Oliviero, M., Severino, G., Straus, T., Jefferies, S. M., and Appourchaux, T.: 1999, *The Astrophysical Journal* **516**, L45.

Rast, M. P.: 1999, *The Astrophysical Journal, submitted.*

Rast, M. P. and Bogdan, T. J.: 1998, *The Astrophysical Journal* **496**, 527.

Rhodes, E. J., Kosovichev, A. G., Schou, J., Scherrer, P. H., and Reiter, J.: 1997, *Solar Physics* **175**, 287.

Rimmele, T. R., Goode, P. R., Harold, E., and Stebbins, R. T.: 1995, *The Astrophysical Journal* **444**, L119.

Rosenthal, C. S.: 1998, *The Astrophysical Journal* **508**, 864.

Roxburgh, I. W. and Vorontsov, S. V.: 1995, *Monthly Notices Of The Royal Astronomical Society* **272**, 850.

Roxburgh, I. W. and Vorontsov, S. V.: 1997, *Monthly Notices Of The Royal Astronomical Society* **292**, L33.

Scherrer, P. H., Bogart, R. S., Bush, R. I., Hoeksema, J. T., G., K. A., Schou, J., Rosenberg, W., Springer, L., Tarbell, T. D., Title, A., Wolfson, C. J., and Zayer, I.: 1995, *Solar Physics* **162**, 129.

Stein, R. F.: 1966, *Generation and Propagation of Acoustic and Internal Gravity Waves in the Solar Atmosphere, PhD. thesis, (Columbia University).*

Stein, R. F.: 1967, *Solar Physics* **2**, 385.

Stein, R. F. and Nordlund, A.: 1989, *The Astrophysical Journal* **342**, L95.

Stein, R. F. and Nordlund, A.: 1998, *The Astrophysical Journal* **499**, 914.

Straus, T., Fleck, B., Severino, G., Deubner, F.-L., Marmolino, C., and Tarbell, T.: 1998, in E. R. Priest (ed.), *A Crossroads for European Solar and Heliospheric Physics: Recent Achievements and Future Mission Possibilities*, Tenerife, ESA SP-417, 293.

Straus, T., Severino, G., Deubner, F.-L., Fleck, B., Jefferies, S. M., and Tarbell, T.: 1999, *The Astrophysical Journal* **516**, 939.

Thiery, S., Boumier, P., Gabriel, A. H., and et al.: 1999, *Astronomy and Astrophysics,* *submitted.*

Toutain, T.: 1993, in D. O. Gough and I. W. Roxburgh (eds.), *IRIS VI: Proceedings Of The Sixth IRIS Workshop*, (University of Cambridge), 28.

Toutain, T., Approurchaux, T., Baudin, F., Frohlich, C. Gabriel, A., Scherrer, P. H., Andersen, B. N., Bogart, R., Bush, R., Finsterle, W., García, R. A., Grec, G., Henney, C. J., Hoeksema, J. T., Jiménez, A., Kosovichev, A. G., Roca Cortés, T., Turck-Chièze, S., Ulrich, R., and Wehrli, C.: 1997, *Solar Physics* **175**, 311.

Toutain, T., Approurchaux, T., Frohlich, C., Kosovichev, A. G., Nigam, R., and Scherrer, P. H.: 1998, *The Astrophysical Journal* **506**, L147.

Turck-Chièze, S., Basu, S., Brun, A. S., and et al.: 1997, *Solar Physics* **175**, 247.

Ulrich, R.: 1970, *The Astrophysical Journal* **162**, 993.

Unno, W.: 1964, *Transactions I.A.U.* **XIIB**, 555.

Wang, Z., Ulrich, R. K., and Coroniti, V.: 1995, *The Astrophysical Journal* **444**, 879.

Woodard, M.: 1984, *Short-Period Oscillations in the Total Solar Irradiance, Ph.D. Thesis, (San Diego: University of California).*